SPATIAL ANALYSIS OF CELLULAR NETWORKS: META DISTRIBUTIONS, COOPERATION, AND JOINT GEOMETRIC MODELING

A Dissertation

Submitted to the Graduate School
of the University of Notre Dame
in Partial Fulfillment of the Requirements
for the Degree of

Doctor of Philosophy

by

Ke Feng

Martin Haenggi, Director

Graduate Program in Electrical Engineering
Notre Dame, Indiana
December 2021

SPATIAL ANALYSIS OF CELLULAR NETWORKS: META DISTRIBUTIONS, COOPERATION, AND JOINT GEOMETRIC MODELING

Abstract

by

Ke Feng

This dissertation takes a probabilistic approach to analyze cellular networks, with an emphasis on the spatial aspect. This approach is substantiated by the increasingly dense and irregular deployment of base stations as well as the need for tractability for advanced network analysis. For instance, in recent developments, the ultra-reliable and low-latency communications (URLLC) is introduced as a keystone to support mission-critical applications; there is also a shift of emphasis from the average/peak performance to a seamless user experience. These developments require guaranteed performance at the link level under varied propagation conditions, interference, and so on. To model these variations, the framework of stochastic geometry is developed, with the primary goal of refining the network analysis to the link level. Previously, network metrics are often analyzed in ways that obscure the effects of multiple sources of spatial and temporal randomness. An important example is the success probability, defined through the distribution of the signal-to-interference-plus-noise ratio (SINR). The SINR is subject to randomness both temporally and spatially, including the small-scale fading and the large-scale propagation loss. Distinguishing their effects is a crucial step towards the analysis of next-generation networks.

The dissertation consists of three parts. In the first part, we study the SINR meta distribution, which defines the individual link reliability by first conditioning

on the spatial locations of base stations. Exploiting the independence between the small-scale fading and large-scale path loss, we derive the separability of the meta distributions for arbitrary fading. In the second part, we quantify the performance gap between the typical user and the cell edge users; then we investigate cooperative transmissions to improve the performance of the latter. The last part focuses on the correlation between the irregular base station deployment and the large-scale propagation conditions. We show that properly accounting for this correlation reveals a critical deployment gain over models that ignore the dependence.

CONTENTS

FIGURES

TABLES

SYMBOLS

Φ	point process
λ	intensity
$\mathbb{P}$	probability measure
$\mathbb{E}$	expectation
$\mathbb{V}$	variance
$\mathbb{R}^d$	d-dimensional Euclidean space
$\|x\|$	Euclidean metric of $x \in \mathbb{R}^d$
$\|\cdot\|$	Lebesgue measure (in $\mathbb{R}^d$)
α	path loss exponent
$\mathbb{1}(\cdot)$	indicator function
$\#$	cardinality

ACKNOWLEDGMENTS

I would like to thank Dr. Martin Haenggi, my Ph.D. advisor, who has created a liberal and supporting research environment during my time in graduate school. He is the best person to work with and a role model in many ways. The thing that I appreciate most is his pursuit of being precise about what is and what is not—an essential quality in general and particularly in scientific research and communications.

I benefited from many interactions with Dr. Panos Antsaklis, Dr. Bertrand Hochwald, Dr. Yih-Fang Huang, Dr. J Nicholas Laneman, Dr. Hai Lin, Dr. Ken Sauer, and Dr. Wenyi Zhang. I especially thank Dr. Hochwald, Dr. Sauer, and Dr. Zhang for many helpful conversations. I also thank Dr. Hochwald, Dr. Huang, and Dr. Laneman for serving on my defense committee. Their feedback leads me to think deeply about the impacts and contributions of my work. I thank Dr. Gerard Misiolek for introducing me to more mathematics. I thank my wonderful colleagues for the technical and casual discussions we had on a daily basis, especially Abbas, Arash, Jeya, Kang, Kewei, Nora, Sanket, Tan, Wenhao, and Yinhao. I thank my roommate Yujia for her generosity and friendship. I thank Christine for her help throughout the graduate school. I am also indebted to the Hesburgh Library, the book club, gradSWE, and the women's boxing team. The financial support from the National Science Foundation is gratefully acknowledged.

Finally, my utmost appreciation goes to my family and friends, with a special thank to my grandfather. Their love and support make it possible for me to go on adventures.

CHAPTER 1

INTRODUCTION

1.1 Spatial Analysis of Wireless Networks

Wireless signals propagating in space are subject to fading at the large and small scales, and they interfere with each other when using the same channel. These basic characteristics inevitably lead to performance variation of wireless links across space and time. While a probabilistic approach has long been used to characterize small-scale fading and its effect on link reliability, only in the recent decades has it become prevalent to characterize large-scale propagation and interference through spatial modeling. The reason is that, with the evolution of network infrastructure, any specific spatial configuration risks losing the generality of the conclusions from which they are obtained; it also usually lacks tractability and prevents advanced analysis. In contrast, a probabilistic approach to the spatial analysis of wireless networks has the advantages of (1) considering all possible spatial realizations (dictated by the distribution of the spatial model), and (2) establishing a clear connection between the performance and assumptions through a few key system parameters. This probabilistic approach falls into the framework of stochastic geometry, the study of random spatial patterns.

1.1.1 A Brief History

One of the earliest works on spatial modeling of wireless networks is the work by Gilbert [1]. Assuming communication devices are distributed in the two-dimensional

space according to a Poisson point process (PPP) with a given density and each communicates within a range of radius R, this work studies *what is the probability that a device belongs to a connected component of size* N. This models multi-hop wireless networks where the characterization of wireless connectivity is simplified using a single parameter R. It is further shown that there exists a critical threshold R_c above which $N \to \infty$ is possible. Later this work is followed by research efforts both on the theoretical side, *e.g.*, stochastic geometry, random graphs, and percolation [2–5], and their applications on communication/network engineering, *e.g.*, connectivity, coverage, and delay in wireless networks such as cellular, ad hoc, and vehicular networks [6–10]. In the past few decades, crisp analyses are obtained for emerging wireless networks within the framework of stochastic geometry. One of the most successful cases is cellular networks.

In cellular networks, each base station (BS) serves a set of users based on the signal strengths, which largely depend on the large-scale path loss and shadowing. The coverage region of a BS is referred to as its cell. Such a structure is naturally characterized by the Voronoi tessellations (Definition 1.2). Traditionally, the hexagonal cellular structure is used despite its mathematical intractability. In [11], it is proposed to model BSs and users as PPPs. In contrast to the hexagonal model, the PPP captures the dense and irregular BS deployment of evolving cellular networks while producing tractable results. Since then, key quantities such as the signal-to-interference-plus-noise ratio (SINR), interference, rate, delay, area spectral efficiency are studied via functionals of the Poisson point processes [12, 13]. The special case of the worst-case users, usually users close to cell edges, is also investigated [14, 15]. It is shown both in experiments and analysis that there is a huge performance gap between generally placed users and the cell-edge users. The framework also generalize to multi-tier networks [14, 16] and general BS point processes [17–20]. We refer to [10, 21, 22] for reviews of stochastic geometry modeling of cellular networks.

1.1.2 Meta Distributions

An increasingly important characterization of wireless systems is the achievable performance by almost all links at almost all times, not just a subset of links or peak performance. This requires the evaluation of spatial and temporal randomness in (at least) two separate steps, which is formalized by the notion of *meta distributions* in [23–25]. For instance, a fundamental quantity that determines the link capacity is the SINR, which is subject to the small-scale fading and the large-scale fading. The reliability of a given link (i.e., fixed transceiver locations) refers to the probability of the SINR exceeding a threshold under only the small-scale fading, which varies significantly over short distances/time (depending on the wavelength of the signal), whereas the large-scale fading is considered static at fixed locations. The SINR meta distribution is the distribution of the link reliability, which gives the fraction of links in the network that achieve a target reliability $x \in [0, 1]$ (for a given target SINR threshold). However, the exact characterization of the SINR meta distribution is difficult to obtain even in the case of Rayleigh fading. In Chapter 2, we obtain the separability of the meta distributions by exploiting the independence between the small and large-scale fading [26, 27]. The separability allows characterization of tail performance for arbitrary fading statistics and is accurate in the high-reliability scenarios.

1.1.3 Cooperation

The performance disparity between cell-center users and cell-edge users in cellular networks is long known yet rarely quantified in spatial models. In Chapter 3, we quantify this disparity in Poisson cellular networks [28]. Further, a base station cooperation scheme is investigated where multiple base stations jointly serve the same user. Joint transmission schemes are known as the coordinated multipoint (CoMP) techniques in the long-term evolution (LTE) and further developed in the fifth gen-

eration (5G) specifications, to provide macro diversity to improve link reliability, throughput, and mobility. In contrast to existing schemes, the proposed scheme activates cooperative transmission only if a user's received signal strengths from nearby base stations are relatively close. This policy translates to a geometric policy, where geometric regions of cell centers, cell edges, and cell corners are defined. The cooperating BSs are Delaunay neighbors. We show that this scheme jointly improves the cell edge performance and the uniformity of the user experience [29, 30].

1.1.4 Joint Spatial-Propagation Modeling

In cellular networks, base station deployment often correlates with the large-scale propagation conditions for coverage. In particular, cellular operators deploy more base stations in regions with severe signal decay, and vice versa, such that cell-edge users can achieve sufficient signal strength. However, this correlation is ignored in almost all prior theoretical works. In Chapter 4, we bridge this gap by studying a joint spatial-propagation model. This model ascribes the irregular deployment of base stations to an intelligent design by the operators, rather than to pure randomness. We show that, even though the Poisson deployment is often considered pessimistic, it achieves near-optimal coverage when the spatial-propagation correlation is accounted for [31].

1.2 Preliminaries

Definition 1.1 (Spatial random point process)**.** *A spatial random point process is a countable random set* $\Phi = \{x_1, x_2, ...\} \subset \mathbb{R}^d$.

By using the random set formalism, we have implicitly assumed that the point process is *simple*, *i.e.*, no points are collocated. This assumption holds for the modeling of BS locations in most cases. Alternatively, the random measure formalism is useful for general point processes [7, Chapter 2].

Definition 1.2 (Voronoi Tessellations)**.** *The Voronoi cell $V(x)$ of a point x of a general point process $\Phi \subset \mathbb{R}^d$ consists of those locations of $\mathbb{R}^d$ whose distance to x is not greater than their distance to any other point in Φ, i.e.,*

$$V(x) \triangleq \{u \in \mathbb{R}^d \colon \|x-u\| \leq \|z-u\|,\ \forall z \in \Phi\}. \tag{1.1}$$

Further, we require Φ to be locally finite, *i.e.*, $\#\{\Phi \cap B\} < \infty$ almost surely if $|B| < \infty$, stationary, *i.e.*, its distribution is translation-invariant, and ergodic, *i.e.*, spatial averages correspond to ensemble averages. We consider two points to be neighbors if they share a boundary, *i.e.*, if their Voronoi cells overlap in $d-1$ dimension. The dual graph for the Voronoi tessellation corresponds to the Delaunay triangulation, where two points are connected if they are neighbors. In $\mathbb{R}^2$, a Voronoi edge contains locations equidistant to two points, and a Voronoi vertex is a location equidistant to three points.

Definition 1.3 (Intensity measure)**.** *The intensity measure Λ of a point process $\Phi \subset \mathbb{R}^d$ is defined as*

$$\Lambda(B) \triangleq \mathbb{E}\#\{\Phi \cap B\}, \tag{1.2}$$

where B is any Borel set in $\mathbb{R}^d$.

For a stationary process, $\Lambda(B) = \lambda|B|$, where λ is the intensity of the point process, and $|\cdot|$ is the Lebesgue measure in $\mathbb{R}^d$.

Two classes of random point processes are of particular interest for BS modeling: the homogeneous PPP and the stationary lattices. In general, the actual BS deployment falls somewhere between the PPP (completely random) and triangular lattices (completely repulsive) [20]. As a result, these two are often used as references for pessimistic deployment and optimistic deployment. The other difference is that the PPP is tractable while metrics such as the SINR statistics for lattice networks are obtained by simulations or analytical approximations.

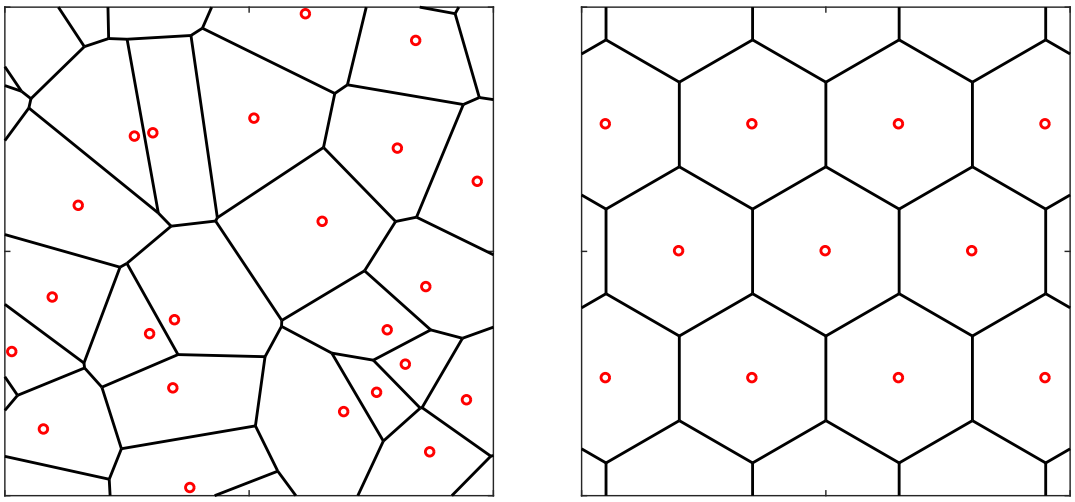

(a) Poisson-Voronoi cells. (b) Hexagonal cells.

Figure 1.1. Illustration of the Poisson-Voronoi tessellation and the hexagonal cellular structure.

Definition 1.4 (Homogeneous PPP)**.** *The homogeneous PPP with intensity λ is a point process in $\mathbb{R}^d$ such that*

- *for every compact set B, the number of points falling into B has a Poisson distribution with mean $\lambda|B|$, where $|B|$ is the Lebesgue measure of B.*
- *the numbers of points in disjoint bounded sets are independent random variables.*

The intensity λ is the expected number of points of the process per unit area or volume.

Fig. 1.1 shows a realization of the Poisson-Voronoi tessellation and the hexagonal cellular structure.

Theorem 1.5 (Campbell's Theorem for sums)**.** *Let $\Phi \subset \mathbb{R}^d$ be a point process with mean measure Λ, and let $f\colon \mathbb{R}^d \to \mathbb{R}$ be measurable. Then the sum*

$$S = \sum_{x \in \Phi} f(x) \tag{1.3}$$

is a random variable with mean

$$\mathbb{E}S = \int_{\mathbb{R}^d} f(x)\Lambda(\mathrm{d}x) \tag{1.4}$$

provided the right hand side is finite.

Proof. See [7, Theorem 4.1]. □

For a stationary point process, $\mathbb{E}S = \lambda \int_{\mathbb{R}^d} f(x)\mathrm{d}x$.

Theorem 1.6 (Campbell's Theorem for Poisson point process)**.** *Let $\Phi \subset \mathbb{R}^d$ be a homogeneous Poisson point process with intensity λ, and let $f\colon \mathbb{R}^d \to \mathbb{R}$ be measurable. Then the sum $S = \sum_{x\in\Phi} f(x)$ is absolutely convergent almost surely if and only if*

$$\int_{\mathbb{R}^d} \min(|f(x)|, 1)\mathrm{d}x < \infty. \tag{1.5}$$

If it is, we have

$$\mathbb{E}\left(e^{tS}\right) = \exp\left(\lambda \int_{\mathbb{R}^d} \left(e^{tf(x)} - 1\right) \mathrm{d}x\right). \tag{1.6}$$

Proof. See [7, Theorem 4.6]. □

CHAPTER 2

META DISTRIBUTIONS

2.1 Introduction

Consider a cellular network where BS locations are modeled using a stationary and ergodic point process $\Phi \subset \mathbb{R}^2$. We focus on the SINR at *the typical user*, which usually involves two different notions.

- Any arbitrary location can be considered as the typical location; a user placed at that location becomes the typical user upon averaging over Φ.
- For an arbitrary stationary point process of users that is independent of Φ, the performance of the typical user corresponds to the average performance of all users.

Here, we adopt the former notion as it is sufficient for downlink analysis. Without loss of generality, we assume that the typical user is located at the origin. Let $x \in \Phi$ be the serving BS and $\Phi \setminus \{x\}$ be the set of interfering BSs. The SINR at the typical user is

$$\mathrm{SINR} \triangleq \frac{h_x \|x\|^{-\alpha}}{\sum_{y \in \Phi \setminus \{x\}} h_y \|y\|^{-\alpha} + \sigma^2}, \tag{2.1}$$

where h_x denotes the fading associated with BS x, $\|\cdot\|^{-\alpha}$ denotes the path loss with exponent α, and σ^2 is the variance of the additive white Gaussian noise. Given the BS locations, the SINR received at the typical user is subject to the randomness of small-scale fading only. In this case, the reliability of the link for a target SINR of θ is defined as

$$P_{\mathrm{s}}(\theta) \triangleq \mathbb{P}(\mathrm{SINR} > \theta \mid \Phi), \quad \theta > 0, \tag{2.2}$$

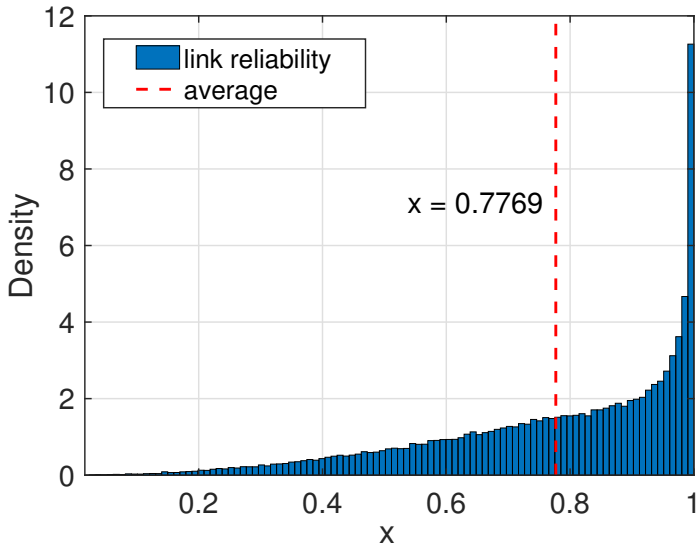

Figure 2.1. Histogram of $P_{\mathrm{s}}(\theta)$ for $\theta = -5$ dB in a Poisson cellular network with iid Rayleigh fading, power-law path loss with $\alpha = 4$, and $\sigma^2 = 0$. The mean reliability is 0.7769, indicated by the red dashed line. Approximately 58.2% of the links achieve $\theta = -5$ dB with reliability above $x = 0.7769$.

which is referred to as the conditional success probability (CSP) interchangeably [23] since it evaluates the probability of success conditioned on the BS point process. The distribution of $P_{\mathrm{s}}(\theta)$ depends on the distribution of Φ. The SINR meta distribution (MD) is defined as [23, 24]

$$\bar{F}_{P_{\mathrm{s}}}(\theta, x) \triangleq \mathbb{P}(P_{\mathrm{s}}(\theta) > x), \quad x \in [0, 1], \tag{2.3}$$

which is the CCDF of the conditional success probability. For any ergodic BS point process, the SINR MD can be interpreted as the fraction of links (or the plane) that achieves θ with reliability higher than x in any realization of the network. Generally, $\bar{F}_{P_{\mathrm{s}}}(\theta, x)$ monotonically decreases with θ and x, and $\bar{F}_{P_{\mathrm{s}}}(\theta, 1) = 0$.

Fig. 2.1 shows the histogram of the conditional success probability for $\theta = -5$ dB in a Poisson network with iid Rayleigh fading, power-law path loss with exponent $\alpha = 4$, and $\sigma^2 = 0$. In this example, approximately 58.2% of the links achieve $\theta = -5$

dB with a reliability above $x = 0.7769$, which is the mean success probability defined as

$$p_{\mathrm{s}}(\theta) \triangleq \mathbb{P}(\mathrm{SINR} > \theta), \quad \theta > 0. \tag{2.4}$$

The mean success probability is extensively studied in the literature of wireless networks modeling using stochastic geometry. With the definitions in (2.2) and (2.4),

$$p_{\mathrm{s}}(\theta) \equiv \mathbb{E}[P_{\mathrm{s}}(\theta)]. \tag{2.5}$$

2.2 Previous Work

For interference-limited networks, the signal-to-interference ratio (SIR) MD for cellular networks with BS cooperation is analyzed in [32], with non-orthogonal multiple access (NOMA) in [33], with offloading in [34, 35], and with power control in [36]. [37] studies the MD in the Poisson typical cell while [38, 39] provide approximations of the MD for non-Poisson cellular networks. The MD for Poisson bipolar networks is studied in [40] as a basis for the spatial outage capacity, defined as the maximum density of concurrently active links that satisfy a certain outage constraint. Most of the work mentioned above evaluate the MD based on simulations or approximations due to the lack of efficient analytical methods. Numerical methods are proposed in [41, 42] to calculate the MD based on the moments of the conditional success probability, which are more tractable. We refer to [43, 44] for comprehensive reviews.

The moments of the conditional success probability in Poisson networks and an exact integral expression for the MD are given in [23]. The authors in [38] study the asymptotics of the moments as $\theta \to 0$ for general networks. They propose to approximate the SIR MD for non-Poisson networks using the shifted version of the MD for Poisson networks. However, only Rayleigh fading is studied in [23, 38].

The SINR MD can also be interpreted as the distribution of the link rate, given

that the transmission rate of each link is adjusted to achieve a target reliability x [45]. Given the quest for ultra-reliable transmission in 5G and beyond communication systems [46], the link-level reliability is expected to be higher than $1-10^{-5}$. It is thus critical to explore the asymptotic behavior of the SINR MD in cellular networks as $x \to 1$. Asymptotic analyses of the (mean) success probability show that, for general 2D stationary point processes under general independent and identically distributed (iid) fading and power-law path loss, $p_{\mathrm{s}}(\theta) = \Theta(\theta^{-\delta})$ as $\theta \to \infty$ with $\delta \triangleq 2/\alpha$ [18, 47–49]. In comparison, here we focus on the asymptotics of the MD as $\theta \to \infty$ and as $x \to 1$. Further, we exploit the connection between the link reliability, rate, and local delay in the context of the MD.

2.3 System Model

Assume that the typical user is associated with its nearest BS, which provides the strongest average signal. Let $x_i(o)$ denote the i-th nearest BS to the typical user and h_i the associated fading power, $i \in \mathbb{N}$. Define $r_i \triangleq \|x_i(o)\|$, the distance to $x_i(o)$. The CSP is

$$P_{\mathrm{s}}(\theta) = \mathbb{P}\bigg(\frac{h_1 r_1^{-\alpha}}{\sum_{i=2}^{\infty} h_i r_i^{-\alpha} + \sigma^2} > \theta \;\bigg|\; \Phi\bigg). \tag{2.6}$$

We first observe that for power-law path loss and arbitrary fading, the noise power σ^2 and the BS density λ jointly impact the MD only through the *network signal-to-noise ratio* (NSNR), defined as follows.

Definition 2.1 (Network Signal-to-Noise Ratio)**.** *The network signal-to-noise ratio for a stationary BS point process with density λ is*

$$\eta \triangleq \lambda^{\alpha/2}/\sigma^2. \tag{2.7}$$

2.4 General Networks

Let Φ_0 be an arbitrary stationary point process of density 1. We assume that the BS locations are modeled by $\Phi = \Phi_0/\sqrt{\lambda}$, where $\lambda > 0$ is the density of Φ.[1]

Lemma 2.2. *For the baseline model, the* SINR *MD depends on λ and σ^2 only through the* NSNR*. Equivalently, if the bandwidth (and thus the noise power) is doubled, the BS density needs to be increased by a factor $2^{2/\alpha}$ to maintain the same performance.*

Proof. Let us write

$$P_{\mathrm{s}}(\theta) = \mathbb{P}\bigg(h_1 > \theta\bigg(r_1^{\alpha}\sum_{i=2}^{\infty} h_i r_i^{-\alpha} + r_1^{\alpha}\sigma^2\bigg) \;\bigg|\; \Phi\bigg). \tag{2.8}$$

For any fading distribution, $r_1^{\alpha}\sum_{i=2}^{\infty} h_i r_i^{-\alpha}$ does not depend on either λ or σ, since $\{r_i\}_{i=1}^{\infty}$ is scaled by the same factor $1/\sqrt{\lambda}$. The distribution of the random variable $r_1^{\alpha}\sigma^2$ depends on $\eta = \lambda^{\alpha/2}/\sigma^2$. □

We observe that densifying the network has the same effect as reducing the noise power. In the ultradense case, as $\eta \to \infty$, the network becomes noise-free—as if $\sigma^2 \to 0$. Conversely, when $\eta \to 0$, the network is interference-free, but the SINR decays to 0. Lemma 1 shows that two networks that differ only in the BS density and noise power are equivalent in their SINR MD performance if $\lambda_1^{\alpha/2}/\sigma_1^2 = \lambda_2^{\alpha/2}/\sigma_2^2$. One may define a crossover point of η and classify the network as interference-limited if $\eta > 1$ (assuming unit transmission power) and noise-limited otherwise. For $\alpha = 4$, $\eta = \lambda^2/\sigma^2$. So if there is twice as much noise, the BS density needs to be increased by a factor of $\sqrt{2}$ to maintain the same performance.

In a practical setting, relevant network parameters include the BS transmission power P (normalized to 1 in this work), the BS density (estimated by the

[1] This way, if Φ_0 is a hard-core process with hard-core distance u, Φ has a hard-core distance $u/\sqrt{\lambda}$.

average inter-site distance), and the noise power (estimated by noise density and channel bandwidth). We can generalize the definition of NSNR to include P, *i.e.*, $\eta = P\lambda^{\alpha/2}/\sigma^2$. For instance, a dense urban scenario may have $\lambda \approx 25/\text{km}^2$ ($\lambda \approx 1/d^2$ for inter-site distance $d = 200$ m in a square lattice) and noise power -94 dBm (for noise density -174 dBm/Hz and 100 MHz channel bandwidth) [50, 51].

A similar observation to Lemma 1 is made in [52, Lemma 4] for the standard success probability, *i.e.*, $\mathbb{E}P_{\text{s}}(\theta)$, and only for the PPP. Note that the equivalence in the standard success probability does not imply the equivalence in the SINR MD, while the opposite holds trivially since $\mathbb{E}P_{\text{s}}(\theta)$ is obtained by integrating the MD over the parameter x. For instance, it is known that for Poisson networks with instantaneously-strongest base station association (ISBA), $\mathbb{E}P_{\text{s}}(\theta)$ does not depend on the fading distribution. Thus it is equivalent to the success probability for no fading [53]. Such an equivalence does not hold for the SINR MD: $P_{\text{s}}(\theta) \in \{0, 1\}$ for no fading while $0 < P_{\text{s}}(\theta) < 1$ for general fading (with continuous distribution).

2.5 Poisson Networks

We now study the separability of the SINR MD in Poisson networks. We first present some useful properties of the PPP. To simplify the notation, we define the distance ratios $t_i \triangleq r_i/r_{i+1}$ for $i \in \mathbb{N}$.

2.5.1 Basic Properties of the Poisson Point Process

Lemma 2.3. *For a homogeneous Poisson point process in* $\mathbb{R}^m$*,*

$$\mathbb{P}(t_i \leq x) = x^{mi}, \quad x \in [0, 1]. \tag{2.9}$$

Proof.

$$\begin{aligned}\mathbb{P}(t_i \le x) &= \mathbb{E}[\mathbb{P}(t_i \le x \mid r_{i+1})] \\ &= \mathbb{E}[\mathbb{P}(r_i \le x r_{i+1} \mid r_{i+1})] \\ &\overset{\text{(a)}}{=} x^{mi}.\end{aligned}$$

Step (a) follows from the fact that conditioning on r_{i+1}, the i points $x_1(o), ..., x_i(o)$ are independently and uniform randomly distributed in the m-dimensional ball with radius r_{i+1}. r_i is the maximum distance of the i points and the distance ratio t_i does not depend on the value of r_{i+1} for $i \in \mathbb{N}$. □

Lemma 2.3 shows that $1/t_i$ is Pareto distributed in Poisson networks. t_i is likely to have a value close to 1 when i is large, which is intuitive since the void probability depends on the volume $c_m(r_i^m/x^m - r_i^m)$, which depends on r_i. Alternatively, we can prove Lemma 2.3 by conditioning on r_i and using the void probability of the PPP and the distribution of r_i [54].

Following Lemma 2.3, it is easy to show that t_1 is independent of any subset of $\{t_i\}_{i\ge 2}$.

2.5.2 Separability

Define $\mathbb{R}^+ \triangleq [0, \infty)$ and $\delta \triangleq 2/\alpha$. The following theorem characterizes the separability of the SINR MD in Poisson cellular networks.

Theorem 2.4. *For Poisson networks, there exists a function $g : [0, 1] \to \mathbb{R}^+$ such that the SINR MD is*

$$\bar{F}_{P_\mathrm{s}}(\theta, x) = g(x)\theta^{-\delta}, \quad (\theta, x) \in \mathcal{D},$$

where

$$\mathcal{D} \triangleq \{(\theta, x) : \mathbb{P}\left(h_1/h_2 > \theta\right) \leq x\}, \tag{2.10}$$

and g depends on the distributions of the fading random variables $\{h_i\}_{i\in\mathbb{N}}$ and η. Further, g is monotonically decreasing with $g(1) = 0$.

Proof. Let us rewrite (2.8) as

$$P_{\mathrm{s}}(\theta) = \mathbb{P}\bigg(h_1 > \theta\Big(\frac{r_1}{r_2}\Big)^{\alpha}\bigg(h_2 + \sum_{i=3}^{\infty} h_i\Big(\frac{r_2}{r_i}\Big)^{\alpha} + r_2^{\alpha}\sigma^2\bigg) \;\Big|\; \Phi\bigg). \tag{2.11}$$

$P_{\mathrm{s}}(\theta)$ is continuous and monotonically decreases with $\theta r_1^{\alpha}/r_2^{\alpha}$. Denote the inverse of $P_{\mathrm{s}}(\theta)$ w.r.t. $\theta r_1^{\alpha}/r_2^{\alpha}$ as f. f is a function of the random variables $\{r_i\}_{i\geq 2}$ and depends on σ^2. Then

$$\begin{aligned}
\bar{F}_{P_{\mathrm{s}}}(\theta, x) &= \mathbb{P}\left(P_{\mathrm{s}}(\theta) > x\right) \\
&= \mathbb{P}\left(\theta r_1^{\alpha}/r_2^{\alpha} < f\left(x, r_2, \ldots\right)\right) \\
&= \mathbb{E}\left[\mathbb{P}\left(\theta r_1^{\alpha}/r_2^{\alpha} < f\left(x, r_2, \ldots\right) \mid r_2, \ldots\right)\right] \\
&= \mathbb{E}\left[\min\left\{1, \theta^{-\delta} f\left(x, r_2, \ldots\right)^{\delta}\right\}\right].
\end{aligned}$$

The last step follows from the fact that for a PPP, $\mathbb{P}(r_1/r_2 < t) = t^2$ and r_1/r_2 is independent from $\{r_i\}_{i\geq 2}$.

For $(\theta, x) \in \mathcal{D}$,

$$P_{\mathrm{s}}(\theta) > x \quad \Rightarrow \quad P_{\mathrm{s}}(\theta) > \mathbb{P}\left(h_1 > \theta h_2\right) \tag{2.12}$$

Writing $P_{\mathrm{s}}(\theta)$ as (2.11), we conclude $f(x, r_2, \ldots) < \theta$ for $\forall\{r_i\}_{i\geq 2}$, $(\theta, x) \in \mathcal{D}$. Note

that $\sum_{i=3}^{\infty} h_i (r_2/r_i)^{\alpha} + r_2^{\alpha}\sigma^2 > 0$. Hence

$$\begin{aligned} \bar{F}_{P_{\mathrm{s}}}(\theta, x) &= \theta^{-\delta}\mathbb{E}\left[f\left(x, r_2, \ldots\right)^{\delta}\right] \\ &= \theta^{-\delta} g(x), \quad (\theta, x) \in \mathcal{D}. \end{aligned} \tag{2.13}$$

The dependence of g on the fading distributions is obvious, and the dependence on η follows from Lemma 1. The monotonicity of g is inherited from the monotonicity of the SINR MD with $\bar{F}_{P_{\mathrm{s}}}(\theta, 1) = 0$ for any $\theta > 0$. □

When $(\theta, x) \notin \mathcal{D}$, (2.13) becomes an upper bound. Adding noise does not change the separable region in [26]. This is because the noise power, which appears in an extra term $r_2^{\alpha}\sigma^2$ in (2.11), does not change the regime in which $f < \theta$.

Remark 2.1. *From (2.10), the separable region is $x \geq 0$ as $\theta \to \infty$. So $\lim_{\theta\to\infty} \theta^{\delta}\mathbb{E}P_{\mathrm{s}}(\theta) = \lim_{\theta\to\infty} \theta^{\delta} \int_0^1 \bar{F}_{P_{\mathrm{s}}}(\theta, x)\mathrm{d}x = \lim_{\theta\to\infty} \theta^{\delta} \int_{\mathcal{D}} g(x)\theta^{-\delta}\mathrm{d}x = \int_0^1 g(x)\mathrm{d}x$. For $\sigma = 0$, $\int_0^1 g(x)\mathrm{d}x = \mathrm{sinc}\,(\delta)$ where $\mathrm{sinc}\,(x) \triangleq \sin(\pi x)/(\pi x)$. This follows from [55, Theorem 4] which shows that for the PPP with arbitrary iid fading, $\mathbb{E}P_{\mathrm{s}}(\theta) \sim \mathrm{sinc}(\delta)\theta^{-\delta}$, $\theta \to \infty$. Theorem 1 shows that $\mathbb{E}P_{\mathrm{s}}(\theta) = \Theta(\theta^{-\delta})$ also holds for Poisson networks with noise, and the pre-constant depends on the noise. To obtain the pre-constant $\int_0^1 g(x)\mathrm{d}x$ for $\sigma > 0$, we can directly modify the statement and proof in [55, Theorem 4] to include noise. For the PPP with iid fading h,*

$$\mathbb{E}P_{\mathrm{s}}(\theta) \sim \mathrm{sinc}(\delta)\theta^{-\delta} \int_0^{\infty} \exp(-x - Kx^{1/\delta})\mathrm{d}x, \ \theta \to \infty, \tag{2.14}$$

where $K \triangleq (\pi\mathbb{E}[h^{\delta}]\Gamma(1-\delta))^{-1/\delta}/\eta$. Hence for $\sigma > 0$, $\int_0^1 g(x)\mathrm{d}x$ depends on $\mathbb{E}[h^{\delta}]$. Specifically, for $\delta = 1/2$,

$$\int_0^1 g(x)\mathrm{d}x = \frac{1}{\sqrt{\pi K}} \,\mathrm{erfc}\left(\frac{1}{2\sqrt{K}}\right) \exp\left(\frac{1}{4K}\right). \tag{2.15}$$

For no fading, $K = 1/(\eta\pi^3)$, and for Rayleigh fading, $K = 4/(\eta\pi^4)$. Further, [55, Theorem 4] proves that $\mathbb{E}P_{\mathrm{s}}(\theta) = \Theta(\theta^{-\delta})$ holds for all simple stationary BS point processes in the noise-free scenario. A natural conjecture is that the MD satisfies $\Theta(\theta^{-\delta})$ for all simple stationary BS point processes with noise.

Corollary 2.5. *Let $\mathcal{D}$ be expressed in terms of $(1/(1+\theta), x) \subset [0,1]^2$. For any iid fading, $\mathcal{D}$ always contains the point $(1/2, 1/2)$, and the area of $\mathcal{D}$ is 1/2.*

Proof. The separable region $\mathcal{D}$ in terms of (θ, x) is

$$x \geq \mathbb{P}\left(h_1/h_2 > \theta\right) \tag{2.16}$$

$$= \mathbb{P}\left(\frac{h_1 + h_2}{h_2} > \theta + 1\right) \tag{2.17}$$

$$= \mathbb{P}\left(\frac{h_2}{h_1 + h_2} < \frac{1}{1+\theta}\right). \tag{2.18}$$

Letting $t = 1/(1+\theta)$, we have $\mathcal{D} = \{(t, x) \colon x \geq \mathbb{P}(h_2/(h_1+h_2) < t)\}$, which is a subset of $[0,1]^2$. For any iid fading, $\mathbb{P}(h_2/(h_1+h_2) < 1/2) = 1/2$. Thus $(1/2, 1/2) \in \mathcal{D}$.

The area of $\mathcal{D}$ is

$$\int_{\mathcal{D}} \mathrm{d}x\mathrm{d}t = \int_0^1 1 - \mathbb{P}\left(\frac{h_2}{h_1+h_2} < t\right) \mathrm{d}t \tag{2.19}$$

$$= 1 - \mathbb{E}\left[\frac{h_2}{h_1+h_2}\right] \tag{2.20}$$

$$\overset{\text{(a)}}{=} \frac{1}{2}. \tag{2.21}$$

Step (a) holds since $\mathbb{E}h_2/(h_1+h_2) = \mathbb{E}h_1/(h_1+h_2) = 1/2$ for any iid h_1, h_2. □

Remark 2.2. *Corollary 1 shows that for any iid fading, $\mathcal{D}$ always covers half of the parameter space. Further, the boundary of $\mathcal{D}$, $x = \mathbb{P}(h_2/(h_1+h_2) < t)$, is an odd function w.r.t. the center point $(1/2, 1/2)$. This is proved by showing that for iid*

fading,

$$\mathbb{P}(h_2/(h_1+h_2)<t)+\mathbb{P}(h_2/(h_1+h_2)<1-t)=1.$$

2.5.3 Impact of Fading

We first study the separable region for iid Nakagami-m fading[2], $m>0$. The rate of Nakagami-m fading is set to $1/m$ to have unit mean power for any m. We then focus on two special cases, namely no fading ($m\to\infty$) and Rayleigh fading ($m=1$). Throughout the rest of the paper, we denote by h the fading random variable.

The PDF of Nakagami-m fading is

$$f_h(x)=\frac{m^m}{\Gamma(m)}x^{m-1}e^{-mx},\quad x\geq 0, \tag{2.22}$$

and the CCDF is

$$\begin{aligned}\bar{F}_h(x)&=\frac{m^m}{\Gamma(m)}\int_x^\infty t^{m-1}e^{-mt}\mathrm{d}t\\&=\frac{\Gamma(m,mx)}{\Gamma(m)}.\end{aligned}$$

Theorem 2.6. *For Poisson networks with Nakagami-m fading, $m>0$,*

$$\mathcal{D}=\left\{(\theta,x)\colon I_{\frac{1}{1+\theta}}(m,m)\leq x\right\}, \tag{2.23}$$

where $\theta>0, x\in[0,1]$, and $I_p(a,b)$ is the regularized incomplete beta function.

[2]While Nakagami-m fading has been defined only for $m\geq 1/2$ [56], our results hold for any positive m.

Proof.

$$\begin{aligned}
\mathbb{P}(h_1/h_2 > \theta) &= \mathbb{E}\big[\mathbb{P}(h_1 > \theta h_2 \mid h_2)\big] \\
&\overset{\text{(a)}}{=} \frac{1}{\Gamma(m)}\mathbb{E}\int_{m\theta h}^{\infty} t^{m-1}e^{-t}\mathrm{d}t \\
&\overset{\text{(b)}}{=} \frac{m^m}{\Gamma(m)}\int_{\theta}^{\infty} \mathbb{E}\big[h^m e^{-mhu}\big]u^{m-1}\mathrm{d}u \\
&\overset{\text{(c)}}{=} \frac{\Gamma(2m)}{(\Gamma(m))^2}\int_{\theta}^{\infty} \frac{1}{(1+u)^{m+1}}\frac{u^{m-1}}{(1+u)^{m-1}}\mathrm{d}u \\
&\overset{\text{(d)}}{=} \frac{\int_0^{\frac{1}{1+\theta}} v^{m-1}(1-v)^{m-1}\mathrm{d}v}{B(m,m)} \\
&= I_{\frac{1}{1+\theta}}(m,m).
\end{aligned}$$

Step (a) follows from the PDF of h. Step (b) follows from change of variable $u = t/mh$. Step (c) follows from $\mathbb{E}[h^m e^{-mhu}] = m^{-m}\Gamma(2m)/\Gamma(m)(1+u)^{2m}$ and (d) follows from the change of variable $v = 1/(1+u)$. The last step follows from the definition of the regularized incomplete beta function. Letting $\mathbb{P}(h_1/h_2 > \theta) \leq x$, we obtain $\mathcal{D}$. □

Fig. 2.2 shows the boundary of the separable region. We plot $I_{\frac{1}{1+\theta}}(m,m)$ versus $1/(1+\theta)$ for $m = 1/2,\ 1,\ 2,\ 3$, and $m \to \infty$. The x-axis is chosen such that it is in $[0,1)$. Note that the boundary $I_{\frac{1}{1+\theta}}(m,m)$ contains the point $(1/(1+\theta), x) = (1/2, 1/2)$ for any finite m, which is stated in Corollary 1. And the area of $\mathcal{D}$ is $1/2$. For $m \to \infty$, $I_{\frac{1}{1+\theta}}(m,m)$ is a step function: $x = 1$ for $\theta < 1$, and $x = 0$ for $\theta \geq 1$. For $m \to 0$, $I_{\frac{1}{1+\theta}}(m,m) \to 1/2$ for any $\theta > 0$.

Without fading, *i.e.*, $h \equiv 1$, $P_{\mathrm{s}}(\theta) \in \{0,1\}$. $\bar{F}_{P_{\mathrm{s}}}(\theta, x) = \mathbb{E}P_{\mathrm{s}}(\theta) = \mathbb{P}(\mathrm{SINR} > \theta)$, $\forall x \in (0,1)$. The separable region is $\mathcal{D} = \{\theta \geq 1, 0 < x < 1\}$, and $\mathbb{P}(\mathrm{SINR} > \theta) = g(x)\theta^{-\delta},\ \theta \geq 1$. For $x \in (0,1)$, $g(x) \equiv g$ is a constant.

$$g = \mathrm{sinc}(\delta)\int_0^{\infty} \exp(-x - Kx^{1/\delta})\mathrm{d}x, \tag{2.24}$$

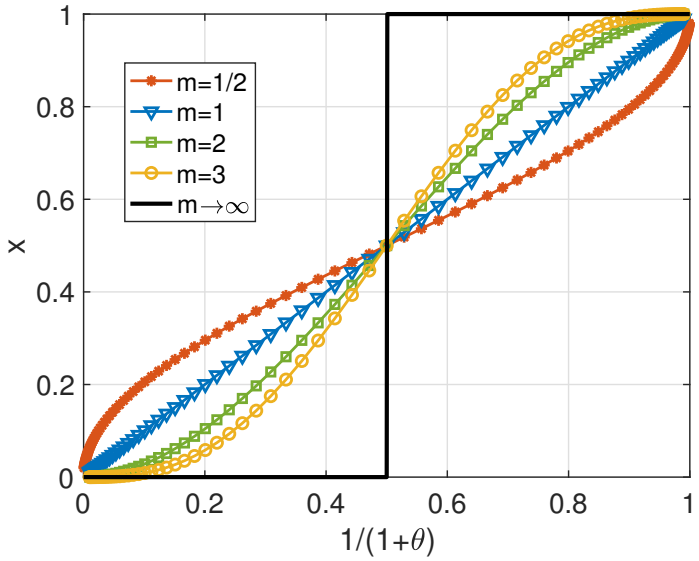

Figure 2.2. The curve $x = I_{\frac{1}{1+\theta}}(m, m)$ (boundary of $\mathcal{D}$) versus $1/(1+\theta)$ for $m = 1/2, 1, 2, 3$, and $m \to \infty$.

where $K = (\pi\Gamma(1-\delta))^{-1/\delta}/\eta$. For $\delta = 1/2$, $K = 1/(\eta\pi^3)$, and g can be written in a closed-form as (2.15). Eq (2.24) simplifies the expression derived in [52, Corollary 5] and generalizes [53, Corollary 2] which considers the noise-free scenario.

With iid Rayleigh fading, the conditional success probability is [57]

$$P_{\mathrm{s}}(\theta) = \exp(-\sigma^2\theta r_1^{\alpha}) \prod_{i=2}^{\infty} \frac{1}{1+\theta\,(r_1/r_i)^{\alpha}}. \tag{2.25}$$

Using the probability generating functional (PGFL) of the PPP, its b-th moment is derived in [57]. Applying Theorem 1, we know that $\bar{F}_{P_{\mathrm{s}}}(\theta, x) = g(x)\theta^{-\delta}$ for $\mathcal{D} = \{(\theta, x) : 1+\theta \geq x^{-1}\}$. $g(x)$ can be obtained through a quick simulation and/or approximated by analytical expressions [26]. We obtain $g(x)$ by simulating $\bar{F}_{P_{\mathrm{s}}}(100, x)100^{\delta}$. Fig. 2.3 shows the impact of η on the MD for SINR thresholds $\theta = 1$ and $\theta = 3$. Fig. 2.4 shows the impact of η on g.

To show the impact of the fading statistics on g, we compare the following four fading scenarios: *i)* no fading, *ii)* iid Rayleigh fading, *iii)* h_1, h_2 iid Rayleigh fading,

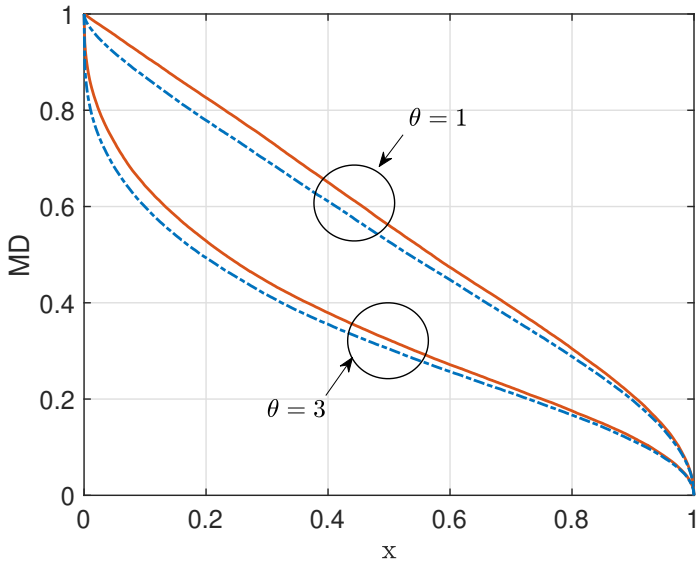

Figure 2.3. MD vs. x for $\theta = 1$ and $\theta = 3$, iid Rayleigh fading, $\delta = 1/2$. The solid curves are for $\eta = \infty$ and the dashed curves are for $\eta = 1$.

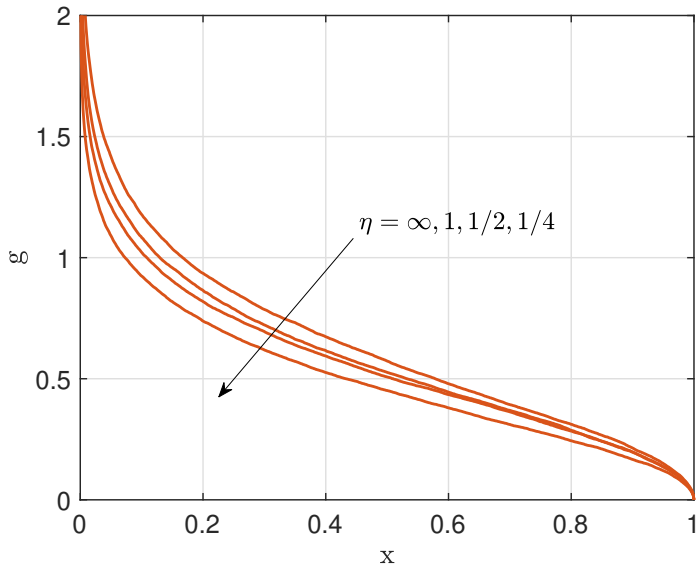

Figure 2.4. Simulation results of $g(x)$ for $\eta = \infty, 1, 1/2, 1/4$, iid Rayleigh fading, $\delta = 1/2$.

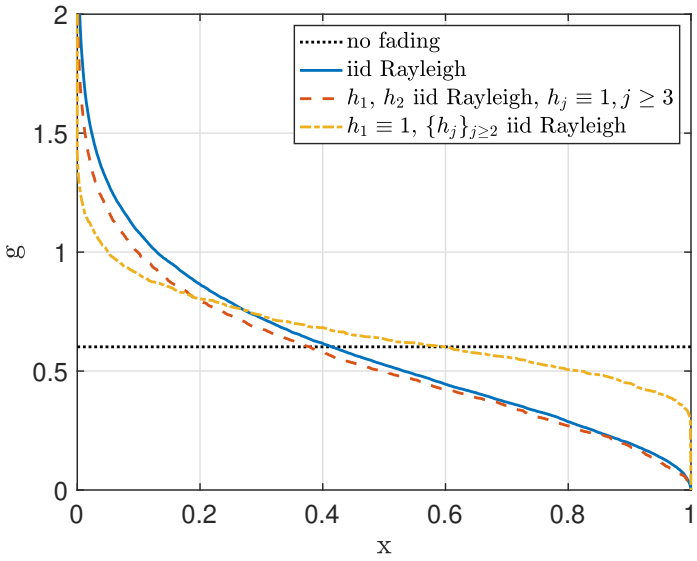

Figure 2.5. $g(x)$ for four fading scenarios. $\eta = 1$, $\delta = 1/2$.

$h_j \equiv 1,\ j \geq 3$, and *iv)* $h_1 \equiv 1$, $\{h_j\}_{j\geq 2}$ iid Rayleigh fading. For *i)*, $\mathcal{D} = \{\theta \geq 1\}$, and $g(x)$ is a constant for $x \in (0, 1)$ as expressed in (2.24), which is approximately 0.6017 for $\delta = 1/2$, $\eta = 1$. For the remaining scenarios, $g(x)$ is obtained through simulation. For scenarios *ii)* and *iii)*, $\mathcal{D} = \{(\theta, x) : 1 + \theta \geq x^{-1}\}$. For *iv)*, $\mathcal{D} = \{(\theta, x) \colon \theta \geq -1/\log(1 - x)\}$, as noted in Remark 2. The results are plotted in Fig. 2.5. $g(x)$ for *iii)* is lower than that for *ii)* since the conditional success probability for *iii)* is smaller than that for *ii)* given the same BS locations. However, the difference is minor, which shows that the fading statistics of faraway interferers do not significantly impact g. In contrast, $g(x)$ for *iv)* is significantly larger than *ii)* at the high-reliability end, and lower at the low-reliability end. Hence combating multi-path fading from the serving BS is crucial for the high reliability scenario and less so for the low reliability scenario.

2.6 Repulsive Network Models

We focus on two specific networks that model the repulsion between BS locations: Ginibre networks [17, 19, 58] and triangular lattice networks. We assume iid Rayleigh fading and that the network is interference-limited ($\sigma^2 = 0$). We are interested in showing that $g(x)\theta^{-\delta}$ serves as a good approximation for these networks. To that end, we simulate the SIR MD for $x = 0.9$ and $x = 0.99$. We show that when θ is chosen large enough, $g(x)\theta^{-\delta}$ is indeed a good approximation. The choice of the "large enough" θ depends on the reliability x.

As is mentioned earlier, only the distances need to be simulated to obtain the MD with Rayleigh fading. The simulation of the distances in a triangular lattice network is straightforward. For Ginibre networks, we use [59, Proposition 4.3].

Proposition 2.7. *The distances $\{r_i\}_{i\in\mathbb{N}}$, for a Ginibre point process have the same distribution as $\{\sqrt{Y_i}\}_{i\in\mathbb{N}}$, where $Y_i,\ i \in \mathbb{N}$, are mutually independent and Y_i follows the i-th Erlang distribution with unit-rate parameter[3], denoted by $Y_i \sim \Gamma(i, 1),\ i \in \mathbb{N}$.*

Fig. 2.6a and 2.6b shows the SIR MD in Ginibre networks and triangular lattice networks for $x = 0.9$ and $x = 0.99$. We consider $g(x)\theta^{-\delta}$ to be a good approximation when its relative error from the simulated result is less than 5%. For Ginibre networks, $0.29\theta^{-\delta}$ provides a good approximation for $\theta \geq 0$ dB when $x = 0.9$; the same accurateness holds with $0.092\theta^{-\delta}$ for $\theta \geq -6$ dB when $x = 0.99$. For triangular lattices, $0.42\theta^{-\delta}$ provides a good approximation for $\theta \geq 6$ dB when $x = 0.9$; the same accurateness holds with $0.134\theta^{-\delta}$ for $\theta \geq -1$ dB when $x = 0.99$. In comparison, for Poisson networks with Rayleigh fading, the "separable region" for $x = 0.9$ and $x = 0.99$ are $\theta \geq -9.54$ dB and $\theta \geq -20$ dB, respectively. Thus, $g(x)\theta^{-\delta}$ provides a good approximation for $\theta \geq -1$ dB when $x = 0.99$ in all cases studied.

[3]The intensity of this Ginibre point process is π^{-1}. Distances in a Ginibre point process with a different intensity can be obtained by scaling the rate parameter of the Erlang distribution.

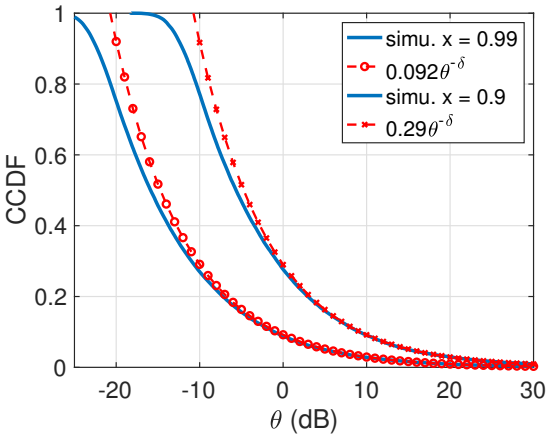

(a) Ginibre networks.

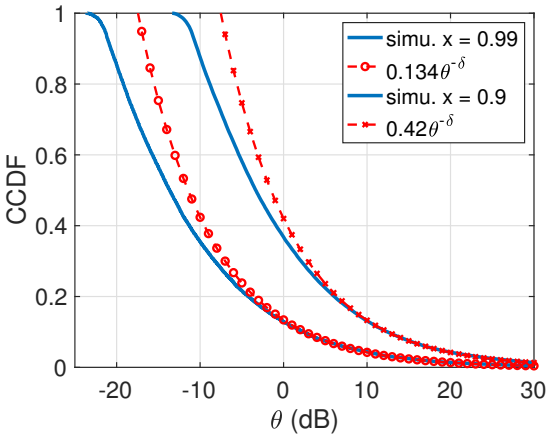

(b) Triangular lattice networks.

Figure 2.6. Simulation and the $g(x)\theta^{-\delta}$ approximation of the SIR MD for $x = 0.9,\ 0.99$ in Ginibre networks and triangular lattice networks, Rayleigh fading, $\alpha = 4$.

2.7 Generalized System Models

2.7.1 General Path Loss Models

Consider a general path loss model $\ell(r)$, with the only requirement that it decreases with the distance r and has an inverse ℓ^{-1}. In general, the tail distribution of the SINR MD in terms of θ depends critically on the path loss from the serving BS, and we can modify the proof for Theorem 2.4 for ℓ. Consider the special case where $h \equiv 1$ (no fading). For the PPP and $\theta \geq 1$,

$$\begin{aligned}\mathbb{P}(\text{SINR} > \theta) &= \mathbb{P}\left(\ell(r_1) < \theta\left(\sum_{i=2}^{\infty} \ell(r_i) + \sigma^2\right)\right) \\ &\overset{\text{(a)}}{=} \mathbb{P}\left[\frac{r_1}{r_2} < \frac{\ell^{-1}\left(\theta\left(\sum_{i=2}^{\infty} \ell(r_i) + \sigma^2\right)\right)}{r_2}\right].\end{aligned}$$

Step (a) follows from first inverting ℓ and then dividing r_2. $\theta \geq 1$ guarantees $\ell^{-1}\left(\theta\left(\sum_{i=2}^{\infty} l(r_i) + \sigma^2\right)\right) < r_2$. If $\ell^{-1}\left(\theta\left(\sum_{i=2}^{\infty} l(r_i) + \sigma^2\right)\right) > 0$, we can apply $\mathbb{P}(r_1/r_2 < x) = x^2$ and the conditional independence of r_1/r_2 given $\{r_i\}_{i\geq 2}$. The power-law path

loss satisfies $\ell^{-1}(xy) = \ell^{-1}(x)\ell^{-1}(y)$, so $(\ell^{-1}(\theta))^2$ will be extracted from the right hand side of (a).

2.7.2 General Path Loss With Selection Combining

Let $n \in \mathbb{N}$ be the number of resource blocks used. We assume the fading coefficients from each BS across different resource blocks are iid. The resource block with the maximum SINR is chosen to decode the message. We have

$$P_{\mathrm{s}}^{(n)}(\theta) = 1 - (1 - P_{\mathrm{s}}(\theta))^n \,, \tag{2.26}$$

and

$$\bar{F}_{P_{\mathrm{s}}}^{(n)}(\theta, x) = \bar{F}_{P_{\mathrm{s}}}\left(\theta, 1 - (1-x)^{\frac{1}{n}}\right). \tag{2.27}$$

By the monotonicity of $\bar{F}_{P_{\mathrm{s}}}(\theta, x)$ w.r.t. x, $\bar{F}_{P_{\mathrm{s}}}^{(n)}(\theta, x) \geq \bar{F}_{P_{\mathrm{s}}}^{(m)}(\theta, x)$ if $n \geq m$. For all links to achieve the same target reliability of x, the number of resource blocks n assigned to each link must adapt to the link SINR. Allowing $n \in \mathbb{R}$ to be a link-dependent random variable for fixed target θ and x, we obtain $n = \log(1-x)/\log(1-P_{\mathrm{s}}(\theta))$.

2.7.3 Power-Law Path Loss With ALOHA

Let $\chi_i \sim \text{Bernoulli}(p)$, $i \in \mathbb{N}$, be iid denoting the transmission status of a BS, *i.e.*, x_i is active if $\chi_i = 1$ and inactive otherwise. The conditional success probability is

$$P_{\mathrm{s}}(\theta) = \mathbb{P}\left(\frac{h_1 r_1^{-\alpha}}{\sum_{i=2}^{\infty} h_i \chi_i r_i^{-\alpha} + \sigma^2} > \theta \mid \Phi\right).$$

It is easy to show that Lemma 1 applies to this setting. For the PPP, $\bar{F}_{P_{\mathrm{s}}}(\theta, x) = g(x)\theta^{-\delta}$, $(\theta, x) \in \mathcal{D}$, where $\mathcal{D} = \left\{(\theta, x) : pI_{\frac{1}{1+\theta}}(m, m) \leq x + p - 1\right\}$. This is calcu-

lated by

$$\mathbb{P}\left(h_1/h_2 > \chi\theta\right) = \mathbb{E}\left[I_{\frac{1}{1+\theta\chi}}(m,m)\right] = pI_{\frac{1}{1+\theta}}(m,m) + 1 - p. \tag{2.28}$$

If $1 - x \geq p$, $\mathcal{D} = \emptyset$. The separable region is different from the baseline model with BS density λp, since the separable region in the baseline model does not depend on BS density. For $\sigma = 0$, the moments of the conditional success probability are derived in [23].

2.7.4 Power-Law Path Loss With BS Silencing

Let $n \in \mathbb{N}$ be the number of silenced BSs. The conditional success probability is

$$P_{\mathrm{s}}(\theta) = \mathbb{P}\left(\frac{h_1 r_1^{-\alpha}}{\sum_{i=n+2}^{\infty} h_i r_i^{-\alpha} + \sigma^2} > \theta \mid \Phi\right). \tag{2.29}$$

Lemma 1 applies to this scenario also. For the PPP, one can derive the separable region via the definition in Theorem 1. $\mathbb{P}(r_1/r_{n+2} \leq x) = 1 - (1-x^2)^{n+1},\ x \in [0,1]$ [60]. Thus the MD is $1 - \mathbb{E}\left[\left(1 - f(x, r_{n+2}, r_{n+3}, ...)\theta^{-\delta}\right)^{n+1}\right]$ in the separable region. For instance, when $n = 1$, *i.e.*, the nearest interferer is silenced, the MD can be written as $a(x)\theta^{-\delta} - b(x)\theta^{-2\delta}$ in the separable region. It satisfies $\bar{F}_{P_{\mathrm{s}}}(\theta, x) = \Theta(\theta^{-\delta}),\ \theta \to \infty$, and is upper bounded by $1 - \left(1 - \mathbb{E}f(x, r_{n+2}, r_{n+3}, ...)\theta^{-\delta}\right)^{n+1}$ due to the convexity of power functions on $\mathbb{R}^+$.

2.8 Asymptotics, Rate, and Local Delay

The link reliability, rate, and latency in wireless networks are fundamentally intertwined. Given the quest for ultra-reliable transmission, we study the asymptotics of the SIR MD as $x \to 1$ for general cellular networks with Rayleigh fading. Then we apply the results of the SIR MD to study the distribution of the link rate and the

local delay. Many of the results can be generalized to the case of SINR.

2.8.1 Asymptotics

2.8.1.1 General Networks

Lemma 2.8. *[47, Theorem 4] For all simple stationary BS point processes Φ and iid fading[4] $\{h_x\}_{x\in\Phi}$, where the typical user is served by the nearest BS,*

$$p_s(\theta) \sim C(\alpha)\theta^{-\delta}, \tag{2.30}$$

where

$$C(\alpha) = \lambda\pi\mathbb{E}_o^!\left[\left(\frac{h}{\sum_{x\in\Phi} h_x\|x\|^{-\alpha}}\right)^{\delta}\right]^{1/\delta}, \tag{2.31}$$

and $\mathbb{E}_o^!$ is the expectation with respect to the reduced Palm measure[5] of Φ.

Theorem 2.9. *For all simple stationary point processes with Rayleigh fading, for any $x > 0$,*

$$\bar{F}_{P_{\mathrm{s}}}(\theta, x) = \Theta(\theta^{-\delta}), \quad \theta \to \infty, \tag{2.32}$$

and for any $\theta > 0$,

$$\bar{F}_{P_{\mathrm{s}}}(\theta, x) \sim C(\alpha)(x^{-1} - 1)^{\delta}\theta^{-\delta}, \quad x \to 1, \tag{2.33}$$

where $C(\alpha)$ is defined in Lemma 2.8 with $h \equiv 1$.

Proof. For Rayleigh fading, the SIR MD is

$$\bar{F}_{P_{\mathrm{s}}}(\theta, x) = \mathbb{P}\bigg(\prod_{i=2}^{\infty}\left(1 + \theta(r_1/r_i)^{\alpha}\right) < x^{-1}\bigg). \tag{2.34}$$

---

[4] [48] derives a sufficient condition of Lemma 2.8 on the fading and the point process.

[5] The reduced Palm distribution is the conditional point process distribution given that the typical point exists at a given location (the origin) but is excluded in the distribution [7, Chapter 8].

For $a_i > 0$, the inequalities

$$1 + \sum_i a_i \leq \prod_i (1 + a_i) \leq \exp\left(\sum_i a_i \right) \tag{2.35}$$

hold, and thus we can bound the SIR MD as

$$\mathbb{P}\left(\exp\left(\sum_{i=2}^{\infty} \theta (r_1/r_i)^{\alpha} \right) < x^{-1} \right) \leq \bar{F}_{P_{\mathrm{s}}}(\theta, x) \leq \mathbb{P}\left(1 + \sum_{i=2}^{\infty} \theta (r_1/r_i)^{\alpha} < x^{-1} \right). \tag{2.36}$$

For the lower bound,

$$\mathbb{P}\left(\exp\left(\sum_{i=2}^{\infty} \theta (r_1/r_i)^{\alpha} \right) < x^{-1} \right) = \mathbb{P}\left(\sum_{i=2}^{\infty} \theta (r_1/r_i)^{\alpha} < -\log x \right) \tag{2.37}$$

$$\sim C(\alpha)(-\log x)^{\delta} \theta^{-\delta}, \quad x \to 1, \tag{2.38}$$

$$\sim C(\alpha)(x^{-1} - 1)^{\delta} \theta^{-\delta}, \quad x \to 1. \tag{2.39}$$

(2.38) also holds for any x and $\theta \to \infty$.

For the upper bound,

$$\mathbb{P}\left(1 + \sum_{i=2}^{\infty} \theta (r_1/r_i)^{\alpha} < \frac{1}{x} \right) = \mathbb{P}\left(\sum_{i=2}^{\infty} \theta (r_1/r_i)^{\alpha} < x^{-1} - 1 \right) \tag{2.40}$$

$$\sim C(\alpha)(x^{-1} - 1)^{\delta} \theta^{-\delta}, \quad x \to 1. \tag{2.41}$$

(2.41) also holds for any x and $\theta \to \infty$.

From (2.38) and (2.41), for any $x > 0$, $\bar{F}_{P_{\mathrm{s}}}(\theta, x) = \Theta(\theta^{-\delta})$, $\theta \to \infty$. For any $\theta > 0$ and $x \to 1$, the asymptotic expressions (2.39) and (2.41) are the same, hence the proof is complete. □

Remark 2.3. *Theorem 2.9 shows that the calculation of the MD in the limiting case boils down to the calculation of the SIR MD without fading. The effect of Rayleigh fading is captured by* $(x^{-1} - 1)^{\delta}$*, and the effect of the network geometry is captured*

by $C(\alpha)$ (under no fading).

Remark 2.4. *Taking the derivative of $g(x)$ at $x \to 1$ yields*

$$\lim_{x\to 1} \frac{\partial \bar{F}_{P_s}(\theta, x)}{\partial x} = -\infty. \tag{2.42}$$

Given $\bar{F}_{P_s}(\theta, 1) = 0$, (2.42) implies that in the ultra-reliable regime, reducing the reliability requirement by a small amount leads to a significant increase of the user percentage satisfying the reliability requirement. This behavior is a result of the unboundedness of the power-law path loss and the distribution of t_1 as $t_1 \to 0$. We contrast this result with that in Poisson bipolar networks [40] where

$$\lim_{x\to 1} \frac{\partial \bar{F}_{P_s}(\theta, x)}{\partial x} = 0. \tag{2.43}$$

This follows from the derivative of $\bar{F}_{P_s}(\theta, x) \sim \exp(-C(1-x)^{-\delta/(1-\delta)})$, $x \to 1$, where $C = (\theta p \delta)^{\delta/(1-\delta)}(1-\delta)(\lambda \pi \Gamma(1-\delta))^{1/(1-\delta)}$ [40, Theorem 4]. Thus, the asymptotic behaviors of the MD for any θ as $x \to 1$ in cellular networks and Poisson bipolar networks are quite different. This is because in Poisson bipolar networks, the distance from the user to the desired transmitter is fixed, while in cellular networks, the user can be arbitrarily closer to the serving BS than to the interfering ones.

2.8.1.2 Poisson Networks

Corollary 2.10. *For Poisson networks with Rayleigh fading, for any $\theta > 0$ and $x \to 1$,*

$$\bar{F}_{P_s}(\theta, x) \sim \mathrm{sinc}(\delta)\theta^{-\delta}(x^{-1} - 1)^{\delta}. \tag{2.44}$$

Proof. It follows from (2.15) that for the PPP,

$$C(\alpha) = \mathrm{sinc}(\delta). \tag{2.45}$$

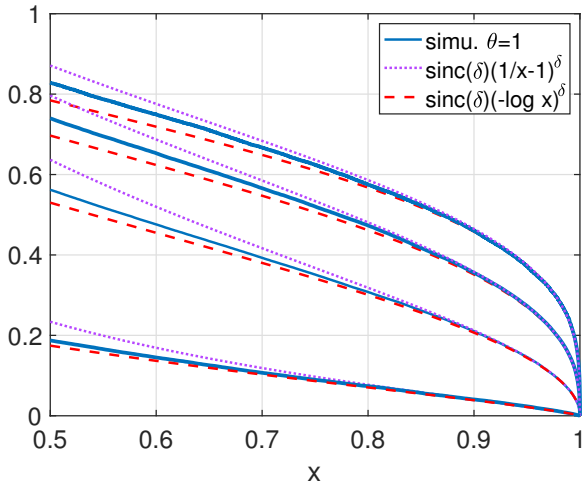

Figure 2.7. $g(x)$ and its asymptotic form using (2.33) in Poisson networks with Rayleigh fading, $\alpha = 2.5, 4, 5.5, 7$ from lower left to upper right.

□

In Poisson networks, by the definition of the separable region, for any θ, $(\theta, x) \in \mathcal{D}$ when $x \to 1$. Thus, (2.44) is equivalent to $g(x) \sim \text{sinc}(\delta)(x^{-1} - 1)^{\delta}$. Fig. 2.7 shows $g(x)$ from simulation and its asymptotic (2.44) for $\alpha = 2.5, 4, 5.5, 7$.

2.8.1.3 Ginibre Networks

Lemma 2.11 ([48])**.** *The distances $\{r_i\}_{i\in\mathbb{N}}$, for a Ginibre point process under the reduced Palm distribution, have the same distribution as $\{Y_{i+1}\}_{i\in\mathbb{N}}$, where Y_i, $i \in \mathbb{N} \setminus \{1\}$ are defined in Proposition 2.7.*

Lemma 2.12. *For Ginibre networks with no fading,*

$$p_{\text{s}}(\theta) \sim C(\alpha)\theta^{-\delta}, \quad \theta \to \infty, \tag{2.46}$$

where

$$C(\alpha) = \mathbb{E}\left[\left(\sum_{i=2}^{\infty} Y_i^{-\frac{\alpha}{2}}\right)^{-\delta}\right] \tag{2.47}$$

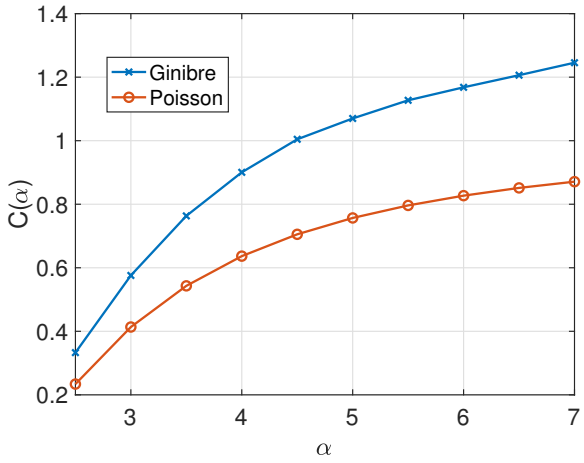

Figure 2.8. $C(\alpha)$ for Poisson and Ginibre networks per (2.45) and (2.47).

and Y_i for $i \in \mathbb{N} \setminus \{1\}$, is defined in Proposition 2.7.

Proof. There are two ways to prove this lemma. The first is by directly applying Lemma 2.8, $h \equiv 1$, and the reduced Palm measure of Ginibre point processes given in Proposition 2.11. Alternatively, we can follow the proof for [18, Theorem 2] and replace Rayleigh fading with no fading. □

Corollary 2.13. *For Ginibre networks with Rayleigh fading,*

$$\bar{F}_{P_s}(\theta, x) \sim C(\alpha)(x^{-1} - 1)^{\delta}\theta^{-\delta}, \quad x \to 1, \tag{2.48}$$

where $C(\alpha)$ is given in Lemma 2.12.

Proof. Follows directly from Theorem 2.9 and Lemma 2.12. □

Fig. 2.8 shows $C(\alpha)$ in Poisson and Ginibre networks for $\alpha \in [2.5, 7]$. The former has an explicit form $C(\alpha) = \text{sinc}(\delta)$ and the latter is simulated using (2.47). For Ginibre networks and $C(4) \approx 0.91$. Fig. 2.9 shows the result in Lemma 2.12 and the two bounds (2.38) and (2.41). Note that from Fig. 2.9b, the lower bound (2.38) is quite tight over the entire range of x.

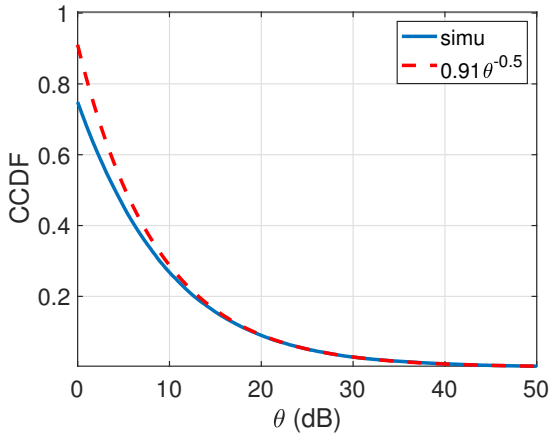

(a) The success probability with no fading.

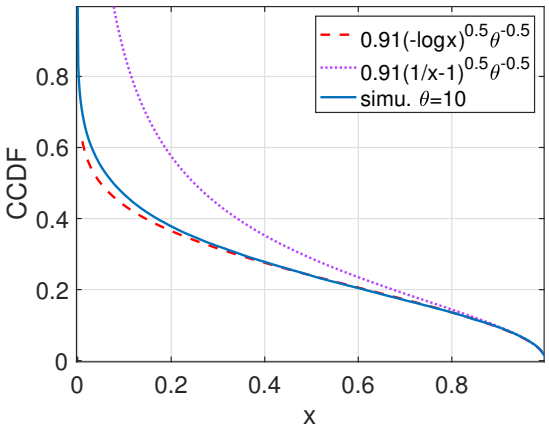

(b) The SIR MD with Rayleigh fading.

Figure 2.9. Asymptotic of the success probability for no fading as $\theta \to \infty$ and two bounds for the SIR MD in Ginibre networks with Rayleigh fading, $\alpha = 4$.

2.8.2 Rate

It is shown in [45, Theorem 1] that the MD can be interpreted as the distribution of the SIR threshold for a fixed link reliability x, denoted by $T(x)$. In adaptive transmission techniques, based on the channel quality of each link, the transmission rate (modulation and coding scheme) is chosen such that a certain reliability can be achieved. For instance, in a network where the target reliability $x = 0.99$, the SIR threshold at each individual link is adjusted such that $\mathbb{P}(\text{SIR} > T(0.99) \mid \Phi) = 0.99$. The local delay is defined as the number of transmissions needed for a message to be received successfully. Retransmissions are less likely to occur for links with a high reliability. The distribution of the delay and, especially, its tail, is a critical metric in 5G cellular networks and beyond. We focus on Poisson networks with Rayleigh fading.

The distribution of the SIR threshold determines the distribution of the transmission rate by the Shannon formula. The normalized rate in nats/Hz/s for a given

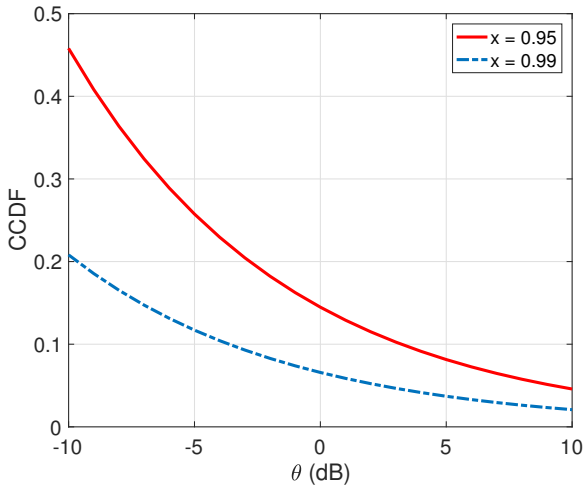

Figure 2.10. $\mathbb{P}(T(x) > \theta)$ for reliability $x = 0.95$ and $x = 0.99$, Poisson networks, $\alpha = 4$.

reliability is defined as

$$\mathcal{R} \triangleq x \log(1 + T(x)), \tag{2.49}$$

where $T(x)$ is the SIR threshold that satisfies the reliability x. It is a random variable whose distribution is a function of x. Let $\bar{\mathcal{R}} \triangleq \mathbb{E}[\mathcal{R}]$ be the ergodic rate for a given reliability x. There is a trade-off between the reliability and the ergodic rate. Setting $x \to 0$ or $x \to 1$ will result in arbitrarily small rate, either due to an ultra-low reliability or due to an ultra-high SIR threshold. Hence, there is an optimal reliability $0 < x < 1$ that maximizes the ergodic rate.

Fig. 2.10 shows the distribution of the SIR threshold when the reliability in the network is fixed. From Theorem 1, when $(\theta, x) \in \mathcal{D}$, the two curves only differ in the constant ratio $0.99g(0.99)/0.95g(0.95) \approx 0.47$, where $g(0.95) = 0.1448$ and $g(0.99) = 0.0658$ are obtained through simulation.

Corollary 2.14. *In Poisson networks, the rate distribution satisfies*

$$\bar{F}_{\mathcal{R}}(r) = g(x)(e^{r/x} - 1)^{-\delta}, \quad (e^{r/x} - 1, x) \in \mathcal{D}, \tag{2.50}$$

and the ergodic rate satisfies

$$\bar{\mathcal{R}} \sim \frac{\pi}{\sin(\pi\delta)} x g(x), \quad x \to 1. \tag{2.51}$$

Proof. For a given reliability x, the rate distribution can be written in the form of the SIR MD as $\bar{F}_{\mathcal{R}}(r) = \bar{F}_{P_{\mathrm{s}}}(e^{r/x} - 1, x)$ [45]. Hence,

$$\bar{F}_{\mathcal{R}}(r) = g(x)(e^{r/x} - 1)^{-\delta}, \quad (e^{r/x} - 1, x) \in \mathcal{D}, \tag{2.52}$$

which follows from Theorem 1. Solving $e^{r/x} - 1 \geq \frac{1}{x} - 1$ for r for a given x using the definition of $\mathcal{D}$ yields $r \geq -x \log x$. The ergodic rate for a given reliability x is

$$\begin{aligned} \bar{\mathcal{R}} &= \int_0^{-x\log x} \bar{F}_{\mathcal{R}}(r)\mathrm{d}r + g(x) \int_{-x\log x}^{\infty} (e^{r/x} - 1)^{-\delta}\mathrm{d}r \\ &= \int_0^{-x\log x} \bar{F}_{\mathcal{R}}(r)\mathrm{d}r + xg(x) \int_{-\log x}^{\infty} (e^{t} - 1)^{-\delta}\mathrm{d}t. \end{aligned} \tag{2.53}$$

The first integral approaches 0 as $x \to 1$ faster than the second integral since $g(x) \sim (x^{-1} - 1)^{\delta}$, and so

$$\bar{\mathcal{R}} \sim xg(x) \int_0^{\infty} (e^{t} - 1)^{-\delta}\mathrm{d}t, \quad x \to 1, \tag{2.54}$$

which evaluates to (2.51). □

With rate adaptation, the ergodic rate is a function of the target reliability. Fig. 2.11 plots the trade-off of the ergodic rate versus the reliability x per Corollary 2.14. (2.51) is asymptotically exact as $x \to 1$. It provides an upper bound for $\bar{\mathcal{R}}$ in general and an accurate approximation when $x \geq 0.8$. It is worth noting that in the simulated per-link rate-reliability trade-off, the optimum rate $\bar{\mathcal{R}} \approx 0.8$ [nats/s/Hz] is achieved at some point for $x \in [0.65, 0.75]$.

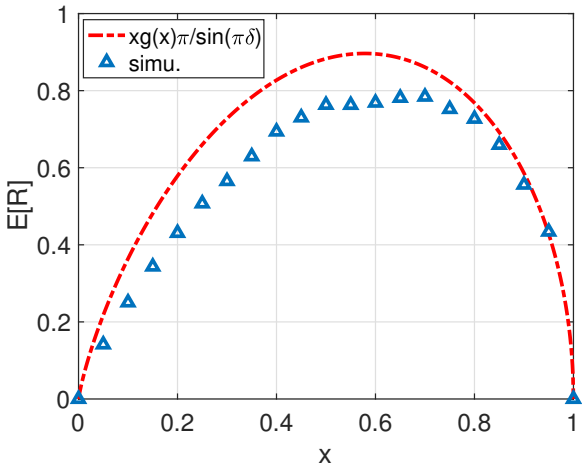

Figure 2.11. The average rate $\bar{\mathcal{R}}$ versus the reliability x and its approximation per (2.54).

2.8.3 Local Delay

The local delay is defined as the number of transmissions, averaged over the fading, needed for a message to be received successfully. Denote by $D(\theta)$ the local delay as a function of θ. We have $D(\theta) \equiv 1/P_{\mathrm{s}}(\theta)$ (the mean of a geometric distribution with success probability $P_{\mathrm{s}}(\theta)$). In other words, the local delay for any individual link is the reciprocal of the link reliability $P_{\mathrm{s}}(\theta)$. It is known that the mean local delay $\mathbb{E}[D(\theta)] = (1-\delta)/(1-\delta(1+\theta))$ for $\theta < 1/\delta - 1$ in Poisson networks with Rayleigh fading [23, Theorem 2]. Here, we provide the asymptotic form of the CDF of the local delay.

Lemma 2.15. *The CDF of the local delay in the network can be expressed using the SIR meta distribution as*

$$\mathbb{P}(D(\theta) \leq t) = \bar{F}_{P_{\mathrm{s}}}(\theta, t^{-1}), \quad t \geq 1. \tag{2.55}$$

Proof. Rewriting the CDF of the local delay as $\mathbb{P}(D(\theta) \leq t) = \mathbb{P}(P_{\mathrm{s}}(\theta) \geq t^{-1})$ we obtain (2.55). □

Corollary 2.16. *For Poisson networks with Rayleigh fading,*

$$\mathbb{P}(D(\theta) \leq 1+\epsilon) = g((1+\epsilon)^{-1})\theta^{-\delta}, \quad \theta \geq \epsilon. \tag{2.56}$$

And for any $\theta > 0$*,*

$$\mathbb{P}(D(\theta) \leq 1+\epsilon) \sim \operatorname{sinc} \delta \epsilon^{\delta} \theta^{-\delta}, \quad \epsilon \to 0. \tag{2.57}$$

Proof. omitted. □

Eq. (2.57) shows the trade-off between the SIR threshold and the target local delay. Note that by Theorem 2.9, the distribution across different types of network models (satisfying the condition in Theorem 2.9) only differs in a constant ratio. Essentially, the fraction of links satisfying a mean local delay constraint w.r.t. θ only depends on the ratio ϵ/θ. For more general networks, the constant $\operatorname{sinc}(\delta)$ is replaced by $C(\alpha)$, which is defined as in Lemma 2.8.

2.9 Summary

1. For stationary base station point processes, arbitrary fading, and power-law path loss with exponent α, the base station density λ and the noise power σ^2 impact the SINR MD only through the network signal-to-noise ratio (NSNR), $\eta \triangleq \lambda^{\alpha/2}/\sigma^2$.
2. In Poisson networks with power-law path loss, the SINR MD for any independent fading, either identically or non-identically distributed, can be expressed as $g(x)\theta^{-\delta}$ for $(\theta, x) \in \mathcal{D}$, where g depends on the NSNR and $\mathcal{D}$ depends on fading statistics. This is referred to as the *separability of the SINR MD in Poisson networks*.
3. For Ginibre and triangular lattice networks, the SIR MD is well approximated by $g(x)\theta^{-\delta}$ in the high reliability regime when θ is chosen large enough. We further characterize the asymptotics of the SINR MD.
4. We show that there is an optimal reliability that maximizes the ergodic rate normalized by the reliability.

CHAPTER 3

COOPERATION

3.1 Introduction

The previous analysis shows that the link reliability is primarily dependent on the distance ratio to the serving BS and nearest interfering BS. In the literature, "the cell edge users" typically refers to users who are almost equally close to the serving and nearest interfering BS and "the cell center users" refers to those who are much closer to the serving BS than to interfering ones. The former type is known to be the bottleneck of the network.

In this chapter, we distinguish these two types of users and quantify their performance gain/loss relative to the typical user. Further, to improve the reliability of users at the cell edge, we exploit cooperative transmission schemes in the context of coordinated multipoint (CoMP). We focus on CoMP joint transmission schemes, which turn a set of interfering BSs into cooperating BSs that jointly serve users. Intuitively, turning distant interfering BSs into cooperating BSs would result in inefficient utilization of BS resources (by adding to the cell load), higher computational effort, and extensive backhaul data exchange, since distant BSs have little impact on either the desired signals or the interference. Hence the cooperating set of BSs is an important design aspect. Here, we propose a geometric policy where the cooperating set is decided by the geometric region of the considered user.

3.2 Quantifying the Performance Gap

In this section, we study the performance gap between two types of users: the cell-center user and the cell-edge users. For any stationary and ergodic base station process, we partition its associated Voronoi cells into the cell centers and the cell edges. We define the region of a location u by how much closer u is to its serving BS than to its nearest interfering BS following [29, 61]. Let $\Phi \subset \mathbb{R}^2$ be an ergodic and stationary BS point process and $x_i(u) \in \Phi$ be the i-th nearest BS to u. For $\gamma \in [0, 1]$ and $\rho \triangleq 1 - \gamma$ we define

$$\begin{aligned} \mathcal{C}_1 &\triangleq \{u \in \mathbb{R}^2 \colon \|u - x_1(u)\| \leq \rho \|u - x_2(u)\|\} \\ \mathcal{C}_2 &\triangleq \{u \in \mathbb{R}^2 \colon \rho \|u - x_2(u)\| < \|u - x_1(u)\|\}. \end{aligned} \tag{3.1}$$

γ controls the area fraction of each region (for any realization of Φ).

In the case when Φ is a homogeneous PPP with intensity λ, the area fraction of each region equals the probability that the origin falls into each region [61]:

$$\mathbb{P}(o \in \mathcal{C}_1) = \rho^2, \quad \mathbb{P}(o \in \mathcal{C}_2) = 1 - \rho^2. \tag{3.2}$$

Theorem 3.1. *The success probability conditioned on the typical user lying in $\mathcal{C}_1$ is*

$$\begin{aligned} \mathbb{P}(\mathrm{SIR} > \theta \mid o \in \mathcal{C}_1) &= \bar{F}_{\mathrm{PPP}}(\theta \rho^{\alpha}) \\ &= \frac{1}{{}_2F_1(1, -\delta; 1 - \delta; -\rho^{\alpha}\theta)}. \end{aligned} \tag{3.3}$$

In particular, for $\alpha = 4$, we have

$$\mathbb{P}(\mathrm{SIR} > \theta \mid o \in \mathcal{C}_1) = \frac{1}{1 + \rho^2 \sqrt{\theta} \arctan\left(\rho^2 \sqrt{\theta}\right)}. \tag{3.4}$$

Proof.

$$\begin{aligned}
\mathbb{P}(\mathrm{SIR} > \theta \mid o \in \mathcal{C}_1) &= \mathbb{P}(S > \theta I \mid o \in \mathcal{C}_1) \\
&= \mathbb{E}\Bigg[\prod_{i=2}^{\infty} \frac{1}{1+\theta(\frac{r_1}{r_i})^{\alpha}} \mid o \in \mathcal{C}_1\Bigg] \\
&= \mathbb{E}\Bigg[\prod_{i=2}^{\infty} \frac{1}{1+\theta\rho^{\alpha}(\frac{r_1/\rho}{r_i})^{\alpha}} \mid o \in \mathcal{C}_1\Bigg] \\
&\overset{\text{(a)}}{=} \mathbb{E}\Bigg[\prod_{i=2}^{\infty} \frac{1}{1+\theta\rho^{\alpha}(\frac{r_1}{r_i})^{\alpha}}\Bigg] \\
&= \bar{F}_{\mathrm{PPP}}(\theta\rho^{\alpha}),
\end{aligned}$$

where (a) is due to the fact that the region $\mathcal{C}_1$ is equivalent to $\{r_1/r_2 \leq \rho\} = \{r_1/\rho \leq r_2\}$. Put differently, the probability law of $r_1/\rho, r_2, ...$ conditioned on $r_1/r_2 \leq \rho$ is the same as the law of $r_1, r_2, ...$ without conditioning. This can be shown by establishing that $f_{\frac{r_1}{\rho}}(x \mid \frac{r_1}{r_2} \leq \rho) = f_{r_1}(x)$ in the following derivation and using the independence property of the PPP:

$$\begin{aligned}
\mathbb{P}\left(r_1 \leq x \mid \frac{r_1}{r_2} \leq \rho\right) &= \frac{\mathbb{P}(r_1 \leq x, r_1/r_2 \leq \rho)}{\mathbb{P}\big(r_1/r_2 \leq \rho\big)} \\
&= \frac{\int_0^x \int_{\frac{u}{\rho}}^{\infty} (2\lambda\pi)^2 uv \exp\left(-\lambda\pi v^2\right) \mathrm{d}v \mathrm{d}u}{\rho^2} \\
&= 1 - \exp\left(-\lambda\pi\frac{x^2}{\rho^2}\right),
\end{aligned} \tag{3.5}$$

and the pdf

$$f_{r_1}\left(x \mid \frac{r_1}{r_2} \leq \rho\right) = \frac{2\lambda\pi x}{\rho^2} \exp\left(-\lambda\pi\frac{x^2}{\rho^2}\right). \tag{3.6}$$

Now

$$f_{\frac{r_1}{\rho}}\left(x \mid r_1/r_2 \leq \rho\right) = 2\pi\lambda x \exp(-\lambda\pi x^2) = f_{r_1}(x).$$

□

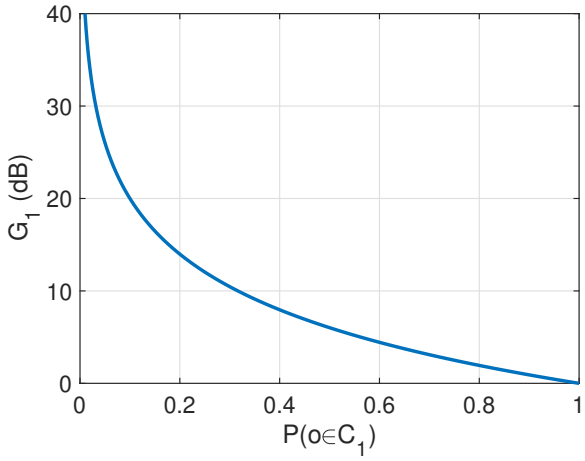

Figure 3.1. The SIR gain (in dB) as a function of the area fraction of $\mathcal{C}_1$, $\alpha = 4$.

Remark 3.1. *Theorem 1 shows the SIR gain (in dB) conditioned on the typical user being in* $\mathcal{C}_1$ *is*

$$G_1 = -10 \log_{10} \rho^{\alpha}. \tag{3.7}$$

Eq (3.7) is remarkably simple and directly shows that the top fraction $x = \rho^2$ of users enjoy an SIR gain of $-5\alpha \log_{10} x$ dB relative to the typical user. Here, the "top" users are those with the highest distance ratio of the nearest interferer and the serving BS. Fig. 3.1 shows the SIR gain G_1 as a function of the area fraction of users in $\mathcal{C}_1$. For instance, there are 31.5% of the users that enjoy an average gain of 10 dB over the typical user, and 10% achieve a gain of 20 dB.

Remark 3.2. *It is interesting to compare this result with the success probability of a BS silencing scheme that mutes all the BSs within* r_1/ρ *for the typical user. We have*

$$\begin{aligned} \mathbb{P}(\mathrm{SIR} > \theta) &= \int_0^{\infty} 2\pi\lambda x \exp\Big(-\pi\lambda x^2 - \int_{\frac{x}{\rho}}^{\infty} \big(1 - \frac{1}{1+\theta(\frac{x}{t})^{\alpha}}\big) 2\pi\lambda t \mathrm{d}t\Big) \mathrm{d}x \\ &= \frac{1}{1 - \rho^{-2} + \rho^{-2}\ {}_2F_1(1, -\delta; 1-\delta; -\rho^{\alpha}\theta)}. \end{aligned} \tag{3.8}$$

It is easy to show that (3.8) is smaller than (3.3) for any $\theta > 0$ and $\rho \in [0, 1]$. This is expected since muting the interfering BSs in r_1/ρ does not affect the ratio of r_1/r_i for $r_i > r_1/\rho$.

3.3 Cooperation

The spatial variation of link performance lead to nonuniformity of user experience. BS cooperation is one of the methods to ameliorate the problem and improve performance at the cell edge. BS cooperation, known as CoMP in 3GPP, is a technique to mitigate/exploit interference and improve reliability by coordinating the signal transmission or enabling the joint transmission/processing among a set of BSs. The design, analysis and optimization of BS cooperation schemes are of significant importance, as the gain of coordination comes at the cost of the backhaul capacity, channel state information (CSI), synchronization efforts, and, in general, more signaling overhead [15]. Hence practical BS cooperation schemes need to be evaluated under the constraint of limited time-frequency resource blocks (RBs) at each BS.

3.3.1 Previous Work

BS cooperation schemes mainly focus on four aspects: the dependence of cooperation on users' channel, the selection of the set of cooperating BSs (fixed-size or adaptive), the cooperation mode (BS silencing, point selection, coherent/non-coherent joint transmission), and its implementation challenges (limited backhaul, imperfect synchronization, imperfect CSI). [61–63] study user-centric BS cooperation while [14, 64] study BS cooperation where all users are non-coherently served by n strongest BSs. It is shown in [14] that users located at the Voronoi vertices benefit more from cooperation than the typical user. Also, it is shown in [64] that increasing the size of the cooperation set leads to a larger variance of the link success probability and thus reduces fairness. In [61, 62], the authors define the "cooperation region"

such that users receive cooperation only when they are located in the cooperation region. Both definitions are based on the relative distances to the serving and the nearest interfering BS, and different cooperation modes are analyzed. In [62], BS silencing is activated for users in the cooperation region. However, [62] assumes a small-cell scenario where there are many inactive BSs and the network is thus less interference-limited. [61] studies the network where all BSs are always active. Users within the cooperation region are coherently served by the two nearest BSs. The scheme, however, relies on the precise channel phase match within the cooperating BSs. A transmission scheme that is less sensitive to channel estimation is analyzed in [63], where the cooperating BSs non-coherently transmit to the target user. The set of cooperating BSs is defined to be BSs within a disk of a fixed radius centered at each user. The definition depends on the selection of the radius and leads to an indefinite size of the cooperating set, which can boost the system complexity. BS cooperation in a two-tier network is studied in [65], where the strongest BSs from each tier jointly serve users who suffer from strong interference. The scheme does not consider the case when both the strongest serving BS and strongest interfering BS belong to the same tier.

3.3.2 A Tunable Cooperation Scheme

In designing the cooperation scheme, we extend our previous definition for cell regions. Define

$$\begin{aligned}
\mathcal{C}_1 &\triangleq \{u \in \mathbb{R}^2 \colon \|u - x_1(u)\| \leq \rho \|u - x_2(u)\|\} \\
\mathcal{C}_2 &\triangleq \{u \in \mathbb{R}^2 \colon \rho \|u - x_2(u)\| < \|u - x_1(u)\|, \ \|u - x_1(u)\| \leq \rho \|u - x_3(u)\|\} \\
\mathcal{C}_3 &\triangleq \{u \in \mathbb{R}^2 \colon \|u - x_1(u)\| > \rho \|u - x_3(u)\|\}.
\end{aligned} \tag{3.9}$$

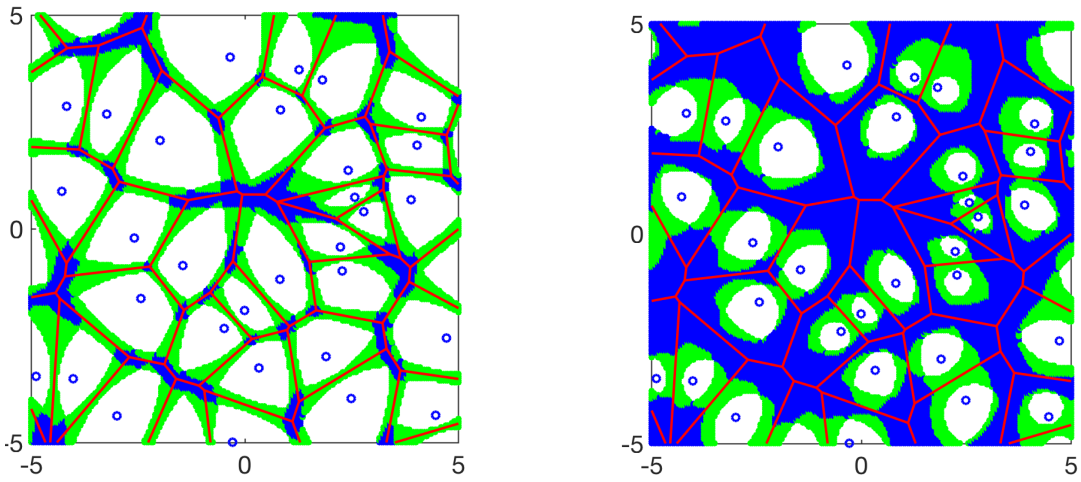

(a) $\gamma = 0.2$. (b) $\gamma = 0.5$.

Figure 3.2. Illustration of the partition when the BSs follow a PPP with intensity $\lambda = 1$ for $\gamma = 0.2$ and $\gamma = 0.5$. The window is $[-5, 5]^2$. Blue circles denote points generated from the PPP. Red lines are the edges of the associated Voronoi cells. Blank, green and blue regions denote the cell center region $\mathcal{C}_1$, the cell edge region $\mathcal{C}_2$, and the cell corner region $\mathcal{C}_3$, respectively.

With a slight abuse of notation ($\mathcal{C}_2 \cup \mathcal{C}_3$ is referred to as "the cell edge region" in the last section), we refer to $\mathcal{C}_1,\ \mathcal{C}_2,\ \mathcal{C}_3$ as "the cell center region", "the cell edge region", and "the cell corner region" respectively. Users within $\mathcal{C}_1,\ \mathcal{C}_2,\ \mathcal{C}_3$ are referred to as "the cell center users", "the cell edge users", and "the cell corner users", respectively. The boundaries of each region $\mathcal{C}_i$ are formed by the union of circular arcs, where for each arc, the two nearest points of Φ are the same and their distance ratio to a point of the arc is ρ. An illustration of the partitioned plane for cooperation levels $\gamma = 0.2$ and $\gamma = 0.5$ is shown in Fig. 3.2.

We define the cooperation set $\mathcal{S}$ to be

$$\mathcal{S} \triangleq \begin{cases} \{x_1(u)\}, & u \in \mathcal{C}_1 \\ \{x_1(u), x_2(u)\}, & u \in \mathcal{C}_2 \\ \{x_1(u), x_2(u), x_3(u)\}, & u \in \mathcal{C}_3. \end{cases} \tag{3.10}$$

In other words, a user in $\mathcal{C}_i$ is jointly served by i BSs since it is relatively close to i BSs.

γ is referred to as the cooperation level since the area fraction of $\mathcal{C}_2 \bigcup \mathcal{C}_3$ increases monotonically with γ. $\gamma = 0$ results in $\mathcal{C}_1 = \mathbb{R}^2$ (no cooperation), and $\gamma = 1$ results in $\mathcal{C}_3 = \mathbb{R}^2 \setminus \Phi$. The special cases $\gamma \in \{0, 1\}$ for the Poisson network have been analyzed in [12, 23] and [14, 64], respectively.

We consider the non-coherent joint transmission scheme to minimize the constraints on CSI. We focus on the typical user located at the origin o, where the desired signal comes from BSs in the defined cooperation sets and the interference comes from the other BSs. The SIR at the typical user is

$$\mathrm{SIR} = \frac{\left| \sum_{x \in \mathcal{S}} h_x \|x\|^{-\alpha/2} \right|^2}{\sum_{x \in \Phi \setminus \mathcal{S}} |h_x|^2 \|x\|^{-\alpha}}.$$

Here, $(h_x)_{x\in\Phi}$ are iid Rayleigh fading, and α denotes the power-law path loss exponent.

3.3.3 Poisson Networks

We study the performance of the scheme in Poisson networks, where $\Phi \subset \mathbb{R}^2$ is a PPP with intensity λ. Let $r_i = \|x_i(o)\|$ be the distance from the origin to its i-th nearest BS as defined before. The joint distribution of r_1, r_2 and r_3 is [66]

$$f_{r_1,r_2,r_3}(x,y,z) = (2\lambda\pi)^3 xyz \exp\left(-\lambda\pi z^2\right), \quad 0 \le x \le y \le z. \tag{3.11}$$

The area fraction of each region depends on γ and is equal to the probability that the origin falls into each region:

$$\mathbb{P}(o \in \mathcal{C}_1) = (1-\gamma)^2, \quad \mathbb{P}(o \in \mathcal{C}_2) = \gamma(1-\gamma)^2(2-\gamma), \quad \mathbb{P}(o \in \mathcal{C}_3) = \gamma^2(2-\gamma)^2. \tag{3.12}$$

Fig. 3.3 shows the area fraction of the three regions as γ increases from 0 to 1.

3.3.3.1 Asymptotic Gain

While the success probability of all but a few basic network models is intractable, the asymptotic SIR gain [67] gives a simple and unified characterization of the SIR improvement compared to a baseline scheme. Using the PPP model as baseline, G is the asymptotic SIR gain if

$$\bar{F}(\theta) \sim \bar{F}_{\mathrm{PPP}}(\theta/G), \quad \theta \to 0. \tag{3.13}$$

It can be visualized as the asymptotic horizontal shift (in dB) between the SIR distributions of the studied model and the PPP. Following [67], we define the mean

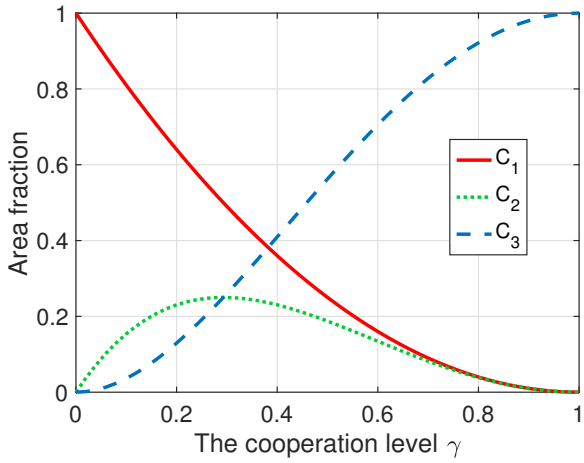

Figure 3.3. The area fraction of the three regions for Poisson networks per (3.12).

interference-signal ratio (MISR) as MISR $\triangleq \mathbb{E}\big(I/\bar{S}\big)$, where $\bar{S} \triangleq \mathbb{E}_h[S]$ is the average signal power. MISR_{PPP} denotes the MISR of the PPP.

Theorem 3.2. *The asymptotic SIR gain of the proposed BS cooperation scheme in Poisson networks is*

$$G = \frac{2}{(\alpha+2)\mathbb{E}\Big[(\frac{r_1}{r_2})^{\alpha}\mathbb{1}_{\mathcal{C}_1}\Big] + (\alpha+4)\mathbb{E}\Big[\frac{(r_1/r_3)^{\alpha}}{1+(r_1/r_2)^{\alpha}}\mathbb{1}_{\mathcal{C}_2}\Big] + 6\mathbb{E}\Big[\frac{(r_1/r_3)^{\alpha}}{1+(r_1/r_2)^{\alpha}+(r_1/r_3)^{\alpha}}\mathbb{1}_{\mathcal{C}_3}\Big]}. \tag{3.14}$$

For $\alpha = 4$, we have

$$G = \Big(\rho^6 + \rho^8\Big(\frac{2}{\rho^2} - \frac{\pi}{2} + 2\arctan\rho^2 - 2\Big) + 3\int_0^{\infty}\int_x^{\frac{x}{\rho}}\int_{\frac{x}{\rho}}^{\infty} \frac{8xyz^{-3}e^{-z^2}}{x^{-4}+y^{-4}+z^{-4}}\mathrm{d}z\mathrm{d}y\mathrm{d}x\Big)^{-1}. \tag{3.15}$$

Proof. The asymptotic SIR gain G can be expressed as

$$G = \frac{\text{MISR}_{\text{PPP}}}{\text{MISR}_{\gamma}}.$$

The MISR of the 2D PPP without cooperation is $\mathrm{MISR}_{\mathrm{PPP}} = 2/(\alpha-2)$ [67], and

$$\mathrm{MISR}_{\gamma} = \mathrm{MISR}_{\mathcal{C}_1} + \mathrm{MISR}_{\mathcal{C}_2} + \mathrm{MISR}_{\mathcal{C}_3},$$

where $\mathrm{MISR}_{\mathcal{C}_i}$ denotes the MISR within $\mathcal{C}_i$. For $\mathcal{C}_1$, we have

$$\mathrm{MISR}_{\mathcal{C}_1} = \sum_{i>1} \mathbb{E}\Big[\Big(\frac{r_1}{r_i}\Big)^{\alpha} \mathbb{1}_{\mathcal{C}_1}\Big] \overset{\text{(a)}}{=} \mathbb{E}\Big[\Big(\frac{r_1}{r_2}\Big)^{\alpha} \mathbb{1}_{\mathcal{C}_1}\Big] \sum_{i>1} \mathbb{E}\Big[\Big(\frac{r_2}{r_i}\Big)^{\alpha}\Big],$$

where step (a) follows from the fact that only the first term in $\mathrm{MISR}_{\mathcal{C}_1}$ is constrained by the cooperation region. It can be calculated using the joint distribution of r_1 and r_2 as

$$\begin{aligned}\mathbb{E}\Big[\Big(\frac{r_1}{r_2}\Big)^{\alpha} \mathbb{1}_{\mathcal{C}_1}\Big] &= \int_0^{\infty} \int_{\frac{x}{\rho}}^{\infty} f_{r_1,r_2}(x,y) \Big(\frac{r_1}{r_2}\Big)^{\alpha} \mathrm{d}y\mathrm{d}x \\ &= \rho^{\alpha+2}.\end{aligned}$$

The second term can be calculated by considering the relative distance process [47]

$$\sum_{i>1} \mathbb{E}\left[\Big(\frac{r_2}{r_i}\Big)^{\alpha}\right] = 1 + \frac{4}{\alpha-2}.$$

Similarly, we obtain the MISR in $\mathcal{C}_2$ and $\mathcal{C}_3$ as

$$\begin{aligned}\mathrm{MISR}_{\mathcal{C}_2} &= \sum_{i>2} \mathbb{E}\Big[\frac{r_i^{-\alpha}}{r_1^{-\alpha} + r_2^{-\alpha}} \mathbb{1}_{\mathcal{C}_2}\Big] \\ &= \mathbb{E}\Big[\frac{(r_1/r_3)^{\alpha}}{1 + (r_1/r_2)^{\alpha}} \mathbb{1}_{\mathcal{C}_2}\Big] \sum_{i>2} \mathbb{E}\Big[\Big(\frac{r_3}{r_i}\Big)^{\alpha}\Big],\end{aligned} \tag{3.16}$$

where

$$\sum_{i>2} \mathbb{E}\left[\Big(\frac{r_3}{r_i}\Big)^{\alpha}\right] = 1 + \frac{6}{\alpha-2},$$

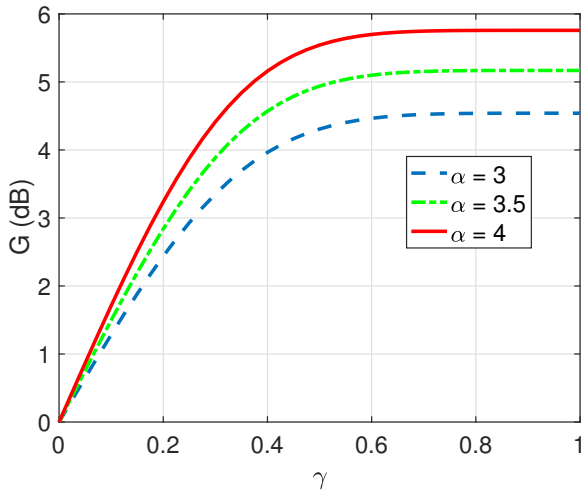

Figure 3.4. The asymptotic gain G (in dB) using (3.14).

and

$$\begin{aligned}
\mathrm{MISR}_{\mathcal{C}_3} &= \sum_{i>3} \mathbb{E}\Big[\frac{r_i^{-\alpha}}{r_1^{-\alpha}+r_2^{-\alpha}+r_3^{-\alpha}}\mathbb{1}_{\mathcal{C}_3}\Big] \\
&= \mathbb{E}\Big[\frac{(r_1/r_3)^{\alpha}}{1+(r_1/r_2)^{\alpha}+(r_1/r_3)^{\alpha}}\mathbb{1}_{\mathcal{C}_3}\Big]\sum_{i>3}\mathbb{E}\Big[\Big(\frac{r_3}{r_i}\Big)^{\alpha}\Big] \qquad (3.17)\\
&= \int_0^{\infty}\int_x^{\frac{x}{\rho}}\int_{\frac{x}{\rho}}^{\infty}\frac{8xyz^{1-\alpha}e^{-z^2}}{x^{-\alpha}+y^{-\alpha}+z^{-\alpha}}\mathrm{d}z\mathrm{d}y\mathrm{d}x\sum_{i>3}\mathbb{E}\Big[\Big(\frac{r_3}{r_i}\Big)^{\alpha}\Big], \qquad (3.18)
\end{aligned}$$

where

$$\sum_{i>3}\mathbb{E}\Big[\Big(\frac{r_3}{r_i}\Big)^{\alpha}\Big] = \frac{6}{\alpha-2}.$$

We obtain the expression for G as in (3.14). □

We next investigate the derivative of the asymptotic SIR gain.

Corollary 3.3 (Derivative at $\gamma=0$ and $\gamma=1$)**.** *The asymptotic SIR gain G satisfies*

$$\frac{\partial G}{\partial\gamma}\Big|_{\gamma=0} = \alpha, \quad \frac{\partial G}{\partial\gamma}\Big|_{\gamma=1} = 0. \qquad (3.19)$$

Proof. For a general α we express G as $G = (G_1 + G_2 + G_3)^{-1}$, where

$$G_1 = (\alpha+2)\mathbb{E}\Big[\Big(\frac{r_1}{r_2}\Big)^{\alpha}\mathbb{1}_{\mathcal{C}_1}\Big] = \rho^{\alpha+2}, \tag{3.20}$$

$$\begin{aligned} G_2 &= \frac{\alpha+4}{2}\mathbb{E}\Big[\frac{(r_1/r_3)^{\alpha}}{1+(r_1/r_2)^{\alpha}}\mathbb{1}_{\mathcal{C}_2}\Big] \\ &= \frac{\alpha+4}{2}\int_0^{\infty}\int_x^{\frac{x}{\rho}}\int_{\frac{x}{\rho}}^{\infty} 8xyze^{-z^2}\frac{z^{-\alpha}}{x^{-\alpha}+y^{-\alpha}}\mathrm{d}z\mathrm{d}y\mathrm{d}x, \end{aligned} \tag{3.21}$$

$$\begin{aligned} G_3 &= 3\mathbb{E}\Big[\frac{(r_1/r_3)^{\alpha}}{1+(r_1/r_2)^{\alpha}+(r_1/r_3)^{\alpha}}\mathbb{1}_{\mathcal{C}_3}\Big] \\ &= 3\int_0^{\infty}\int_x^{\frac{x}{\rho}}\int_{\frac{x}{\rho}}^{\infty} 8xyze^{-z^2}\frac{z^{-\alpha}}{x^{-\alpha}+y^{-\alpha}+z^{-\alpha}}\mathrm{d}z\mathrm{d}y\mathrm{d}x. \end{aligned} \tag{3.22}$$

Now

$$\frac{\partial G}{\partial \rho} = -G^2\Big(\frac{\partial G_1}{\partial \rho}+\frac{\partial G_2}{\partial \rho}+\frac{\partial G_3}{\partial \rho}\Big),$$

where

$$\frac{\partial G_1}{\partial \rho} = (\alpha+2)\rho^{\alpha+1}, \tag{3.23}$$

$$\frac{\partial G_2}{\partial \rho} = \frac{-4\rho^{1+\alpha}}{1+\rho^{\alpha}} + \frac{\rho^{\alpha-3}(\alpha+4)}{2}\int_0^{\infty}\int_x^{\frac{x}{\rho}} x^3e^{-\frac{x^2}{\rho^2}}\frac{8y}{1+(x/y)^{\alpha}}\mathrm{d}y\mathrm{d}x, \tag{3.24}$$

and

$$\frac{\partial G_3}{\partial \rho} = -3\rho^{\alpha-3}\int_0^{\infty}\int_x^{\frac{x}{\rho}} x^3ye^{-\frac{x^2}{\rho^2}}\frac{8}{1+\rho^{\alpha}+(x/y)^{\alpha}}\mathrm{d}y\mathrm{d}x. \tag{3.25}$$

By taking the limit we obtain

$$\frac{\partial G}{\partial \gamma}\Big|_{\gamma=0} = -\lim_{\rho\to 1}\frac{\partial G}{\partial \rho} = \alpha, \tag{3.26}$$

and

$$\frac{\partial G}{\partial \gamma}\Big|_{\gamma=1} = -\lim_{\rho\to 0}\frac{\partial G}{\partial \rho} = 0. \tag{3.27}$$

□

This result shows that the asymptotic gain from $\gamma = 0$ increases with slope α and saturates at $\gamma = 1$. Fig. 3.4 shows the asymptotic SIR gain as γ increases from 0 to 1. When the path loss exponent α grows large, the transmission scenario approaches the point-to-point transmission scenario where the interference is negligible—the interference free scenario. In this case, the network is no longer interference-limited and the effect of noise needs to be considered.

3.3.3.2 Conditional Success Probability

Lemma 3.4. *The conditional success probability for the proposed scheme is*

$$P_{\mathrm{s}}(\theta) = \begin{cases} \prod_{i=2}^{\infty} \frac{1}{1+\theta r_i^{-\alpha}/r_1^{-\alpha}}, & o \in \mathcal{C}_1 \\ \prod_{i=3}^{\infty} \frac{1}{1+\theta r_i^{-\alpha}/(r_1^{-\alpha}+r_2^{-\alpha})}, & o \in \mathcal{C}_2 \\ \prod_{i=4}^{\infty} \frac{1}{1+\theta r_i^{-\alpha}/(r_1^{-\alpha}+r_2^{-\alpha}+r_3^{-\alpha})}, & o \in \mathcal{C}_3. \end{cases} \tag{3.28}$$

Proof. For $o \in \mathcal{C}_1$, the typical user is associated with the nearest BS only, hence

$$\begin{aligned} P_{\mathrm{s}}(\theta) &= \mathbb{P}\left(g_1 r_1^{-\alpha} > \theta \sum_{i=2}^{\infty} g_i r_i^{-\alpha} \right) \\ &\overset{\text{(a)}}{=} \mathbb{E}\left[\exp\left(-\theta \sum_{i=2}^{\infty} g_i r_i^{-\alpha} / r_1^{-\alpha} \right) \right] \\ &\overset{\text{(b)}}{=} \mathbb{E}\left[\prod_{i=2}^{\infty} \exp(-\theta g_i r_i^{-\alpha} / r_1^{-\alpha}) \right] \\ &= \prod_{i=2}^{\infty} \frac{1}{1+\theta r_i^{-\alpha} / r_1^{-\alpha}}. \end{aligned} \tag{3.29}$$

Step (a) follows from the exponential distribution of the fading power. Step (b) follows from the independence of fading coefficients.

For $o \in \mathcal{C}_2$, the typical user receives the non-coherent joint transmission from two nearest BSs, and thus

$$\begin{aligned} P_{\mathrm{s}}(\theta) &= \mathbb{P}\left(|h_1 r_1^{-\alpha/2} + h_2 r_2^{-\alpha/2}|^2 > \theta \sum_{i=3}^{\infty} g_i r_i^{-\alpha} \right) \\ &\overset{\text{(a)}}{=} \mathbb{E}\left[\prod_{i=3}^{\infty} \exp(-\theta g_i r_i^{-\alpha} / (r_1^{-\alpha} + r_2^{-\alpha})) \right] \\ &= \prod_{i=3}^{\infty} \frac{1}{1+\theta r_i^{-\alpha} / (r_1^{-\alpha} + r_2^{-\alpha})}. \end{aligned} \tag{3.30}$$

Step (a) follows from the fact that $|h_1 r_1^{-\alpha/2} + h_2 r_2^{-\alpha/2}|^2$ is exponentially distributed with mean $r_1^{-\alpha} + r_2^{-\alpha}$.

The proof of $o \in \mathcal{C}_3$ is parallel to that of $o \in \mathcal{C}_2$. □

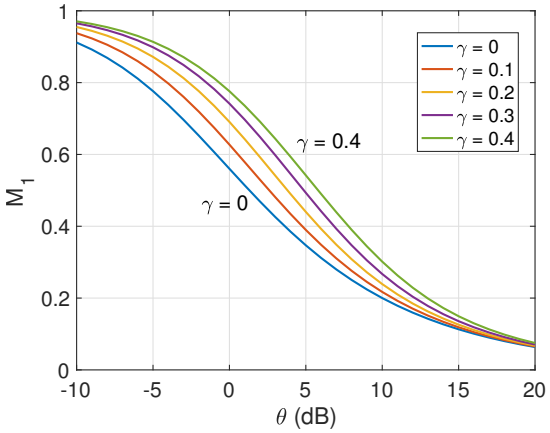

(a) $M_1(\theta)$ for $0 \leq \gamma \leq 0.4$.

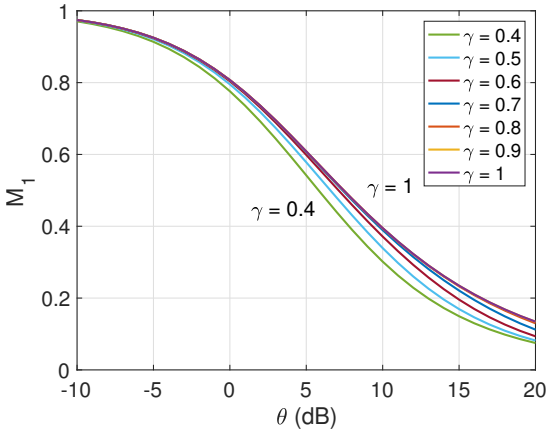

(b) $M_1(\theta)$ for $0.4 \leq \gamma \leq 1$.

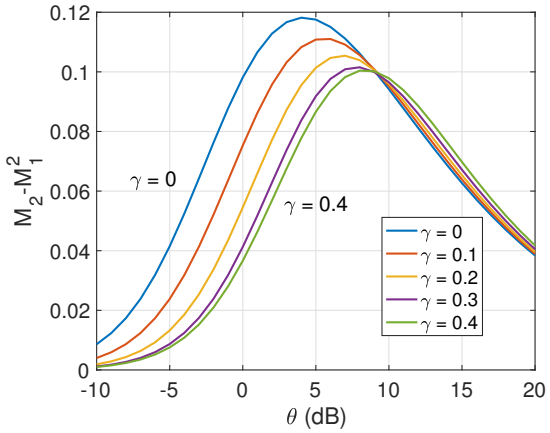

(c) $M_2(\theta) - M_1(\theta)^2$ for $0 \leq \gamma \leq 0.4$.

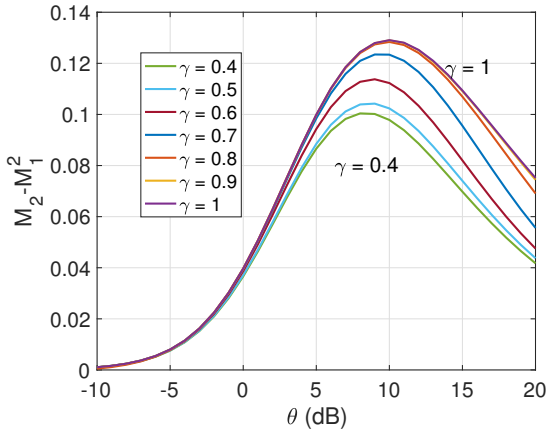

(d) $M_2(\theta) - M_1(\theta)^2$ for $0.4 \leq \gamma \leq 1$.

Figure 3.5. The mean $M_1(\theta)$ and variance $M_2(\theta) - M_1(\theta)^2$ of the conditional success probability with cooperation level $\gamma = 0$ to $\gamma = 1$, $\alpha = 4$.

3.3.3.3 Moments

Theorem 3.5. *The b-th moment of the conditional success probability of the typical user of the proposed scheme in Poisson networks is*

$$\begin{aligned} M_b = & \frac{\rho^2}{{}_2F_1(b,-\delta;1-\delta,-\rho^\alpha\theta)} \\ & + \int_0^\infty \int_x^{\frac{x}{\rho^2}} \int_{\frac{x}{\rho^2}}^\infty \exp\Big(- zF_b\Big(\Big(\frac{z}{x}\Big)^{\frac{1}{\delta}} + \Big(\frac{z}{y}\Big)^{\frac{1}{\delta}}\Big)\Big)\Big(1+\frac{\theta}{\big(\frac{z}{y}\big)^{\frac{1}{\delta}} + \big(\frac{z}{x}\big)^{\frac{1}{\delta}}}\Big)^{-b} \mathrm{d}z\mathrm{d}y\mathrm{d}x \\ & + \int_0^\infty \int_x^{\frac{x}{\rho^2}} \int_y^{\frac{x}{\rho^2}} \exp\Big(- zF_b\Big(1+\Big(\frac{z}{x}\Big)^{\frac{1}{\delta}} + \Big(\frac{z}{y}\Big)^{\frac{1}{\delta}}\Big)\Big)\mathrm{d}z\mathrm{d}y\mathrm{d}x, \quad b\in\mathbb{C}, \end{aligned} \tag{3.31}$$

where $F_b(x) = {}_2F_1(b,-\delta;1-\delta;-\theta/x)$.

Proof.

$$M_b = \mathbb{E}[P_{\mathrm{s}}(\theta)^b] = \sum_{i=1}^{3} \mathbb{E}\left[P_{\mathrm{s}}(\theta)^b \mathbb{1}_{\mathcal{C}_i}\right]. \tag{3.32}$$

For $\mathcal{C}_1$, we know from the last section that $\mathbb{E}[P_{\mathrm{s}}(\theta)^b\mathbb{1}_{\mathcal{C}_1}] = \rho^2/{}_2F_1(b,-\delta;1-\delta,-\rho^\alpha\theta)$. For $\mathcal{C}_2$,

$$\mathbb{E}[P_{\mathrm{s}}(\theta)^b\mathbb{1}_{\mathcal{C}_2}] = \mathbb{E}\left[\prod_{k=3}^{\infty}\left(\frac{1}{1+\theta r_k^{-\alpha}/(r_1^{-\alpha}+r_2^{-\alpha})}\right)^b \mathbb{1}_{\mathcal{C}_2}\right] \tag{3.33}$$

$$\overset{(a)}{=} \int_0^\infty \int_x^{\frac{x}{\rho}} \int_{\frac{x}{\rho}}^\infty \frac{f_{r_1,r_2,r_3}(x,y,z)}{(1+sz^{-\alpha})^b} \exp\Big(- \int_z^\infty \big(1-(1+st^{-\alpha})^{-b}\big)2\pi\lambda t\mathrm{d}t\Big)\mathrm{d}z\mathrm{d}y\mathrm{d}x$$

$$\overset{(b)}{=} \int_0^\infty \int_x^{\frac{x}{\rho^2}} \int_{\frac{x}{\rho^2}}^\infty \frac{\exp(-z)}{(1+sz^{-\alpha/2})^b} \exp\Big(- \int_z^\infty \big(1-(1+st^{-\alpha/2})^{-b}\big)\mathrm{d}t\Big)\mathrm{d}z\mathrm{d}y\mathrm{d}x$$

$$\overset{(c)}{=} \int_0^\infty \int_x^{\frac{x}{\rho^2}} \int_{\frac{x}{\rho^2}}^\infty \exp\Big(- z\ {}_2F_1\Big(b,-\delta,1-\delta,-\frac{s}{z^\alpha}\Big)\Big)(1+sz^{-1})^{-1}\mathrm{d}z\mathrm{d}y\mathrm{d}x.$$

Step (a) follows from letting $s = \theta/(x^{-\alpha} + y^{-\alpha})$. Step (b) follows from changing variables $2\pi\lambda x^2$, $2\pi\lambda y^2$, $2\pi\lambda z^2$, $2\pi\lambda t^2$ to x, y, z, t. Step (c) follows from changing variable $t^{\alpha/2}$ to t and $\int_r^\infty (1 - 1/(1 + sx^{-1})^b) x^{\delta-1} \mathrm{d}x = r^\delta(-1 + {}_2F_1(b, -\delta, 1-\delta, -s/r))/\delta$. $\mathbb{E}[P_{\mathrm{s}}(\theta)^b \mathbb{1}_{\mathcal{C}_3}]$ can be derived by changing the integration region and s. □

We focus on the mean and variance of $P_{\mathrm{s}}(\theta)$, namely M_1 and $M_2 - M_1^2$. Fig. 3.5 shows the success probability and the variance as a function of θ from $\gamma = 0$ to $\gamma = 1$.

For $0 \leq \gamma \leq 0.4$, the maximal variance is monotonically decreasing when θ is small, and is maximized when the success probability is around $p_s(\theta) = 0.35$. For $\gamma \geq 0.4$, the maximal variance starts monotonically increasing. So the minimal maximal variance is achieved when $\gamma = 0.4$. For $0 \leq \gamma \leq 0.4$, the variance when $\theta > 10$ dB is essentially the same. For $\gamma \geq 0.4$, the variance when $\theta < 0$ dB is essentially the same.

For $\gamma = 1$, the results coincide with the proposed scheme in [64], where all users are served by a fixed number of cooperating BSs. It is shown in [64] that such user-independent BS cooperation increases the unfairness (variance of the conditional success probability).

Remark 3.3. *For small θ, the main reason not to succeed is bad fading (fading defines the asymptotic slope of the success probability as $\theta \to 0$). The secondary reason is bad location. Cooperation helps with both, but it makes less of a difference for users in a good location—users near the cell center almost all succeed anyway, even without cooperation. Hence for small θ, M_1 does not change anymore once $\gamma > 0.4$. Similarly, for the variance, all users who need help are receiving it at $\gamma < 0.4$. For larger γ, there is a negligible improvement for most users, hence no further reduction in variance.*

For large θ, the main reason to succeed is good location (proximity to the serving BS defines the asymptotic slope as $\theta \to \infty$). Those users who are quite close to their BS but not extremely close will benefit from cooperation, which means that γ needs

to be fairly large (> 0.4) to make a difference in M_1. Conversely, users who get cooperation for $\gamma < 0.4$ are in such bad location that they cannot succeed at high θ. Similarly, for the variance, for $\gamma < 0.4$ there is no impact since no user switches from not succeeding to succeeding. For $\gamma > 0.4$, the users in almost-great locations start to benefit from cooperation (while those in bad locations still do not), which widens the gap between the two, increasing the variance. This is the regime where "the rich get richer".

3.3.4 Lattice Networks

Here we apply the scheme to two single-tier lattice networks, namely square lattice and triangular lattice networks. Lattice networks are generally less tractable but they provide upper bounds on the network performance due to the optimistic assumption of BS deployment. Here, we confine our analysis to the asymptotic SIR gain and make a comparison between Poisson and lattice networks.

The area fractions of the three regions in lattice networks can be analytically calculated thanks to its rigid structure. The boundaries of each region $\mathcal{C}_i$ are formed by the union of circular arcs, where for each arc, the distance ratio from a point of the arc to its two nearest points is ρ. Note that all the arcs have the same radius and angle depending on γ, as shown in Fig. 3.6. Fig. 3.7 shows the area fraction of each region as γ increases from 0 to 1.

In Fig. 3.8, we compare the asymptotic gain in Poisson networks and lattice networks. The horizontal shift in the lattice cases are approximated using $\tilde{G}_{p_\mathrm{s}=0.95}$, *i.e.*, the horizontal SIR shift of the simulated success probability evaluated at $p_\mathrm{s} = 0.95$. The simulation is performed with 100,000 user locations. The SIR gap at $\gamma = 0$ is the inherent deployment gain between Poisson and lattice networks (3 dB and 3.4 dB respectively [67]). All three curves increase almost linearly at the beginning and tend to saturate around $\gamma = 0.6$. The comparison reveals the similarity of the SIR

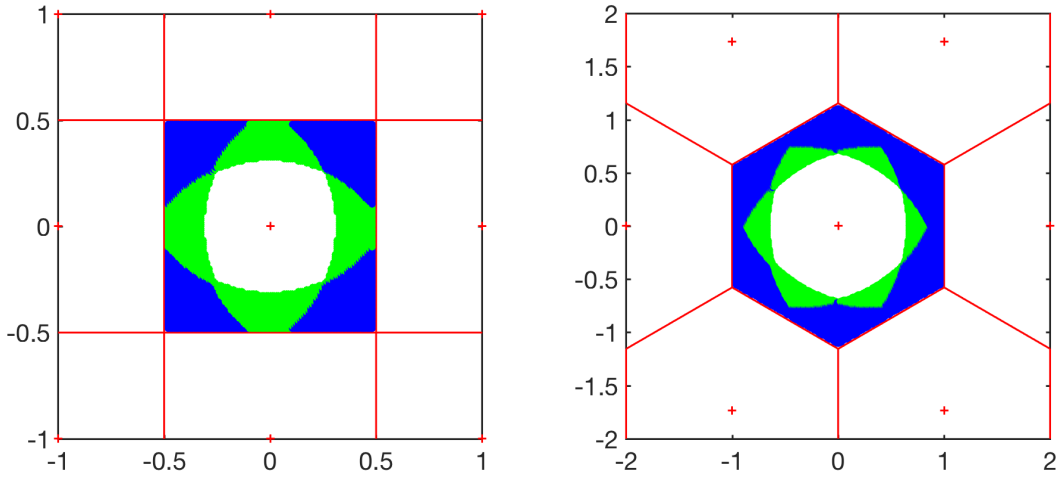

(a) Square lattice. (b) Triangular lattice.

Figure 3.6. The cooperation regions in a square lattice and a triangular lattice network when $\gamma = 0.5$. Only one cell is colored since all cells are shifted version of each other. Red crosses and red lines denote BSs and the edges of the associated Voronoi cells in the lattice. Blank, green and blue regions denote $\mathcal{C}_1$, $\mathcal{C}_2$ and $\mathcal{C}_3$ respectively.

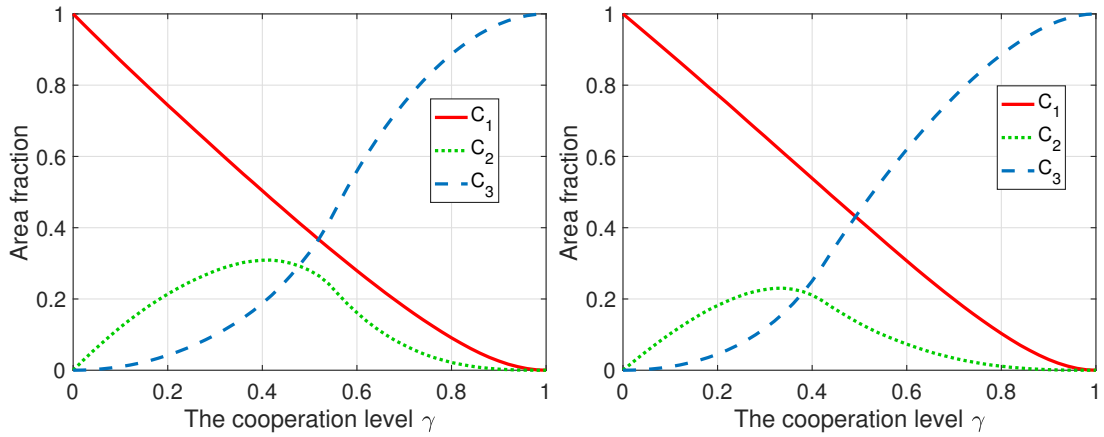

(a) Square lattice. (b) Triangular lattice.

Figure 3.7. The area fractions of the three regions for square and triangular lattices.

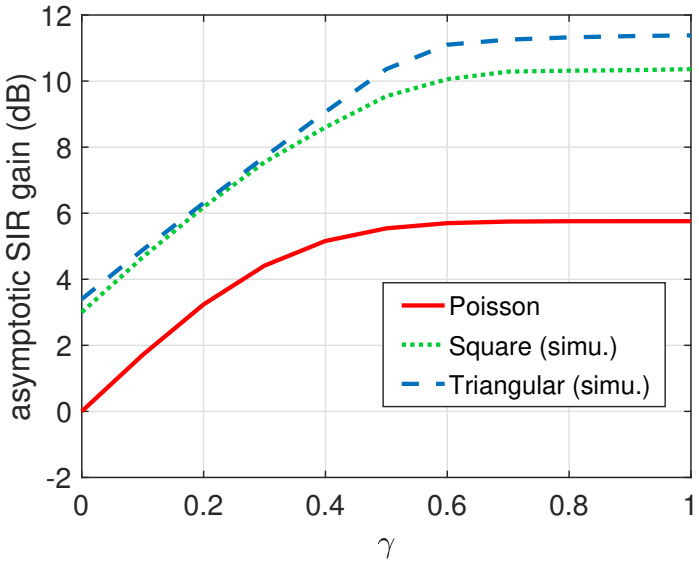

Figure 3.8. The comparison of the asymptotic SIR gain in Poisson networks and lattice networks, $\alpha = 4$.

gain patterns due to BS cooperation in different network structures.

3.4 Summary

1. We show that in Poisson networks, the top fraction x of users enjoy an SIR gain of $-5\alpha \log_{10} x$ dB relative to the typical user. We derive both the exact and asymptotic form of the SIR distribution for the cell boundary users.

2. We propose and study a location-dependent BS cooperation scheme. We introduce a parameter $\gamma \in [0, 1]$ to tune the cooperation level of the network. We derive the SIR distribution and its approximation form based on the asymptotic SIR gain.

3. We show that in Poisson networks: (1) the derivative of the asymptotic SIR gain equals to the path loss exponent α at $\gamma = 0$ (no cooperation) and is 0 at $\gamma = 1$ (full cooperation); (2) a moderate γ jointly improves the SIR performance and the network fairness.

4. BS models including the PPP and lattice networks are studied. We compare the simulation results of the asymptotic SIR gain in lattice networks to Poisson networks and show their similarity.

CHAPTER 4

JOINT SPATIAL-PROPAGATION MODELING

4.1 Introduction

The previous chapters focus on analysis of systems where wireless signal propagation consists of power-law path loss and small-scale fading. Shadowing, caused by obstacles is another propagation effect that leads to spatial variation. It is highly relevant to cell planning. This chapter considers a model where the spatial deployment of BSs and shadowing are inherently correlated. For coverage, cellular operators deploy more BSs in regions with severe signal decay, and vice versa, such that users at the cell boundaries achieve a sufficient and consistent signal strength. In other words, the shape and size of the Voronoi cells reflect the underlying propagation conditions, which we reverse-engineer to devise a cell-dependent correlated shadowing model. To do so, it is necessary to study the cell shape and radii in the Poisson Voronoi tessellation (PVT).

We first introduce the notion of the directional radius of Voronoi cells. The directional radius of a cell is defined as the distance from the nucleus to the cell boundary at an angle relative to the direction of a uniformly random location in the cell. We study the distribution of the radii in two types of cells in the Poisson Voronoi tessellations: the zero-cell, which contains the origin, and the typical cell. The analysis reveals the asymmetry of PVT and is applied later to analyze the JSP model. It will be shown that accounting for the spatial-propagation correlation reveals a critical deployment gain of approximately 3.4 dB over the standard independent model.

4.2 Previous Work

The first and only JSP model is presented in [68], where the authors reverse engineer the path loss exponent (PLE) of the power-law path loss model from the BS locations. A fundamental assumption in [68] is that the PLE is a deterministic function of the BS locations such that users at the Voronoi cell edge receive a minimum average power P_0, or, equivalently, a minimum average signal-to-noise ratio (SNR), from their nearest BS. It is shown that under this assumption, the PPP yields almost the same success probability as the triangular lattice networks. However, there are a few drawbacks in this model. Firstly, it suffers from the singularity of the power-law path loss model, which can result in a negative PLE. Secondly, the assumption that all users along the cell boundaries receive power P_0 is rather optimistic and unlikely to hold in an actual deployment. In this chapter, we take the variation of the received power along the cell boundaries into account. Lastly, the analysis in [68] is limited to the spatially averaged coverage performance, whereas this work provides a more fine-grained analysis.

Also relevant to this model are models that consider correlated shadowing. One of the first correlated shadowing models is proposed in [69], where for a fixed BS and a moving user with a constant velocity, the periodically sampled shadowing is a discrete process whose autocorrelation decays exponentially. A correlated shadowing model with an intuitive physical interpretation is modeled and analyzed in [70], where the "penetration loss" depends on the number of obstacles (in this case, buildings) in the path. A survey of correlated shadowing models can be found in [71]. Apart from the correlation, the variance of shadowing is shown to have a significant impact on network performance [72] [73]. It is derived in [73] that for general BS processes satisfying a homogeneity constraint, if the shadowing correlation is "moderate" (decreasing fast enough in distance), the signal strengths converge to those in a PPP as the variance of shadowing increases.

To facilitate the analysis of the JSP model, we study two types of Poisson Voronoi cells and their radii: the zero-cell, which is the cell that contains the origin, and the typical cell. While it is known that the zero-cell has a larger mean volume than the typical cell [74, 75], the directional radii characterize the shape of the two cells and have not been studied before to the best of our knowledge. Related, the distance from the nucleus to a uniformly random location in the typical cell and the distance from the nucleus of the zero-cell to the typical location are studied in [76]. User point processes are characterized based on the PVT in [77]. The distribution of the distance from the typical Voronoi edge/vertex location to its nearest Poisson point is given in [78, 79], while [80] derives the distribution of the radius of the largest disk included within the cells and the radius of the smallest disk containing the cells. Some gamma-type results[1] are given in [81, 82].

4.3 Directional Radii of Poisson Voronoi Cells

4.3.1 Definitions

We first define the radii of interest. For consistency of the definitions, we introduce the displaced typical cell and zero-cell such that the nucleus of the cells is at the origin. Let $\Phi \subset \mathbb{R}^2$ be a motion-invariant point process of intensity λ.

Typical cell. Let

$$\Phi^o \triangleq (\Phi \mid o \in \Phi)$$

and denote by $V(o)$ the Voronoi cell of Φ^o with nucleus o. Let z be a location chosen uniformly at random from $V(o)$ and let $(\|z\|, \zeta)$ be its polar coordinates. Next, define

$$\tilde{\Phi} \triangleq \mathrm{rot}_{-\zeta}(\Phi^o),$$

[1] Results related to Gamma distribution.

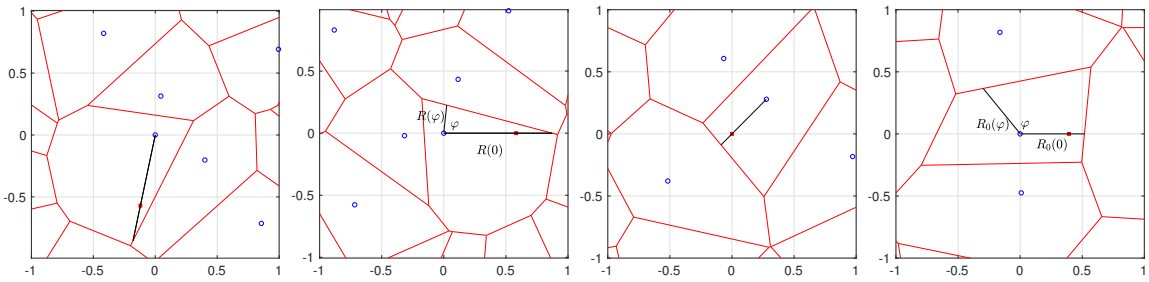

(a) The typical cell. (b) Displaced typical cell. (c) The 0-cell. (d) Displaced 0-cell.

Figure 4.1. Illustration of the directional distances in the typical cell and the 0-cell of a PPP. The blue circles represent Poisson points and the red lines represent the Voronoi tessellations. In (a), the red square represents the uniform randomly distributed point z in the typical cell. In (b), z is displaced to reside on the positive semi x-axis. In (c) and (d), the red square represents the origin and the displaced origin.

where rot_u is a rotation around the origin by angle u, and denote the Voronoi cell of $\tilde{\Phi}$ with nucleus o by $\tilde{V}(o)$. Let $D \triangleq \|z\|$ be the distance from the nucleus of the typical cell to the uniformly random location in the typical cell.

Zero-cell. Let $x_i \in \Phi$ be the $(i+1)$-th closest point to the origin, *e.g.*, $x_0 = \arg\min_{x\in\Phi}\{\|x\|\}$. Let V_0 be the Voronoi cell with nucleus x_0 (which contains the origin). Letting φ_0 be the angle of x_0, define

$$\tilde{\Phi}_0 \triangleq \mathrm{rot}_{\pi-\varphi_0}(\Phi_{-x_0}),$$

where Φ_y is a translation of all points of Φ by y. This way, $o \in \tilde{\Phi}_0$. Let $\tilde{V}_0$ be the Voronoi cell of $\tilde{\Phi}_0$ with nucleus o. Let $D_0 \triangleq \|x_0\|$.

Definition 4.1 (Directional radius)**.** *For $\varphi \in [0, 2\pi)$, we define the directional radius $R(\varphi)$ to the boundary $\partial\tilde{V}(o)$ of the typical cell by*

$$R(\varphi)(\cos\varphi, \sin\varphi) \in \partial\tilde{V}(o)$$

and the directional radius $R_0(\varphi)$ *to the boundary* $\partial\tilde{V}_0$ *of the 0-cell by*

$$R_0(\varphi)(\cos\varphi, \sin\varphi) \in \partial\tilde{V}_0.$$

So $(R(\varphi), \varphi)_{\varphi\in[0,2\pi)}$ parametrizes the boundary of the typical cell $\tilde{V}(o)$ in polar coordinates, and $R(0)$ is the distance from the nucleus to the boundary in the direction of the randomly chosen point. Similarly, $(R_0(\varphi), \varphi)_{\varphi\in[0,2\pi)}$ parametrizes the boundary of the 0-cell $\tilde{V}_0$ in polar coordinates, and $R_0(0)$ is the distance from the nucleus to the boundary in the direction of the displaced origin, now at coordinates $(\|x_0\|, 0)$.

The areas of the two cells are obtained as

$$|\tilde{V}(o)| = \frac{1}{2}\int_0^{2\pi} R^2(\varphi)\mathrm{d}\varphi$$

and

$$|\tilde{V}_0| = \frac{1}{2}\int_0^{2\pi} R_0^2(\varphi)\mathrm{d}\varphi,$$

respectively, and the mean areas follow as

$$\mathbb{E}|\tilde{V}(o)| = \int_0^{\pi} \mathbb{E}(R^2(\varphi))\mathrm{d}\varphi$$

and

$$\mathbb{E}|\tilde{V}_0| = \int_0^{\pi} \mathbb{E}(R_0^2(\varphi))\mathrm{d}\varphi,$$

where $|\cdot|$ is the Lebesgue measure in two dimensions. Integrating over $[0, \pi)$ is sufficient due to the symmetry of the distributions, *i.e.*, $\mathbb{E}R(\varphi) \equiv \mathbb{E}R(-\varphi)$.

Fig. 4.1 shows realizations of the typical cell, the zero-cell and their displaced version when Φ is a Poisson point process.

Definition 4.2 (Uniform-angled radius)**.** *We define the uniform-angled radius* $\bar{R}$ *to*

the boundary $\partial\tilde{V}(o)$ of the typical cell by

$$\bar{R} \triangleq R(\Theta)$$

and the uniform-angled radius $\bar{R}_0$ to the boundary $\partial\tilde{V}_0$ of the 0-cell by

$$\bar{R}_0 \triangleq R_0(\Theta)$$

where

$$\Theta \sim \text{Uniform}[0, 2\pi].$$

Since Φ is motion-invariant, we may equivalently define $\bar{R} \triangleq \|\partial V(o) \cap (\mathbb{R}^+, 0)\|$ and $\bar{R}_0 \triangleq \|\partial V_0 \cap (\mathbb{R}^+, 0)\|$.

R and $\bar{R}$ are related by

$$\mathbb{E}(\bar{R}^b) = \frac{1}{\pi}\int_0^\pi \mathbb{E}(R^b(\varphi))\mathrm{d}\varphi, \tag{4.1}$$

and

$$\mathbb{E}(\bar{R}_0^b) = \frac{1}{\pi}\int_0^\pi \mathbb{E}(R_0^b(\varphi))\mathrm{d}\varphi, \tag{4.2}$$

for $b \in \mathbb{R}$. Again, integrating over $[0, \pi)$ is sufficient due to the symmetry.

Lemma 4.3. *For general point processes where $|V(o)|$ and $|V_0|$ are finite almost surely, we have*

$$\mathbb{P}(\|z\|/R(0) \le t) = t^2, \quad t \in [0, 1], \tag{4.3}$$

and

$$\mathbb{P}(\|x_0\|/R_0(0) \le t) = t^2. \quad t \in [0, 1]. \tag{4.4}$$

Proof. For any point process, conditioned on $V(o)$, let z be uniform randomly distributed in $V(o)$. The probability that $\|z\|/R(0) < t$ is the same as the probability

that z falls into the similar polygon of $V(o)$, with radius scaled by t in all directions. This probability is equal to t^2 for any realization of $V(o)$. The same argument holds for the zero-cell. □

Remark 4.1. *Lemma 4.3 holds for non-stationary point processes also, where the typical cell is centered at the origin.*

4.3.2 The Typical Cell of the PVT

Let Φ be a Poisson point process of intensity λ.

Lemma 4.4. *The pdf of $\bar{R}$ is*

$$f_{\bar{R}}(r) = 2\lambda\pi r e^{-\lambda\pi r^2}. \tag{4.5}$$

Proof. Due to the isotropy of the Poisson process, it is sufficient to consider $\bar{R} = \|\partial V(o) \cap (\mathbb{R}^+, 0)\|$. The event that $\bar{R}$ is larger than r happens if $b((\bar{R}, 0), r)$[2] contains no point. Thus, $\mathbb{P}(\bar{R} > r) = e^{-\lambda\pi r^2}$. □

Remark 4.2. *The mean area of the typical cell follows as*

$$\mathbb{E}|V(o)| = \pi\mathbb{E}(\bar{R}^2) = \frac{1}{\lambda}.$$

Recall that in [75], the mean area of the typical cell is obtained by using Robbin's formula [83] and that for any fixed point $p = (r, \theta)$, $\mathbb{P}(p \in V(o)) = \exp(-\lambda\pi r^2)$,

$$\mathbb{E}|V(o)| = \int_{\mathbb{R}^2} \mathbb{P}\left(p \in V(o)\right) \mathrm{d}p = \int_0^{2\pi} \int_0^{\infty} \exp\left(-\lambda\pi r^2\right) r \mathrm{d}r\mathrm{d}\theta = \frac{1}{\lambda}.$$

Our method and the method in [75] for calculating the mean area are essentially the same, by observing that the event that $\bar{R}$ is larger than r happens if and only if a

[2]The open ball with center (R, ϕ) (in polar coordinates) and radius $r \geq 0$ is denoted by $b((R, \phi), r)$.

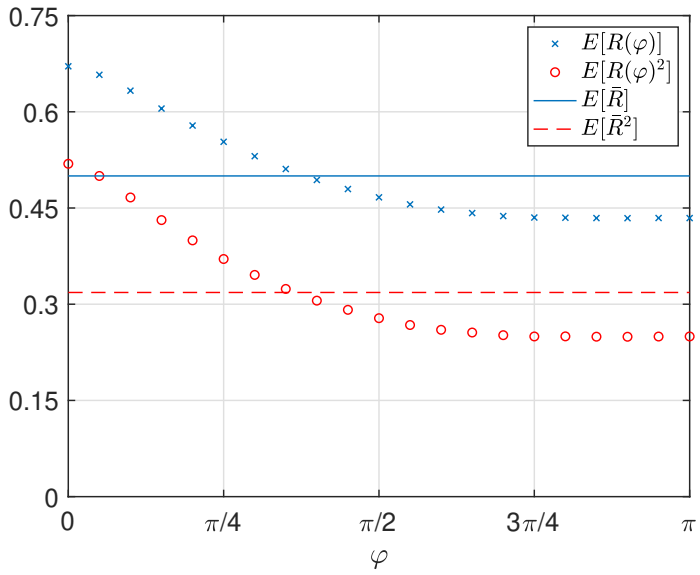

Figure 4.2. First two moments of the directional distances in the typical cell, $\lambda = 1$, via simulation. The mean and second moment of $\bar{R}$ (straight lines) are obtained via Lemma 4.4.

fixed point $(r, 0) \in V(o)$. Its probability does not depend on θ. The result for the mean area holds for arbitrary stationary point processes [74].

Fig. 4.2 shows the first two moments of the directional radius in the typical cell obtained via simulation. It is apparent that the cell is significantly larger in the direction of the randomly chosen point than in the opposite direction. $R(0)$ is on average about 55% larger than $R(\pi)$.

4.3.3 The 0-cell of the PVT

Recall that $D_0 = \|x_0\|$ is the distance from the nucleus of the 0-cell to the origin.

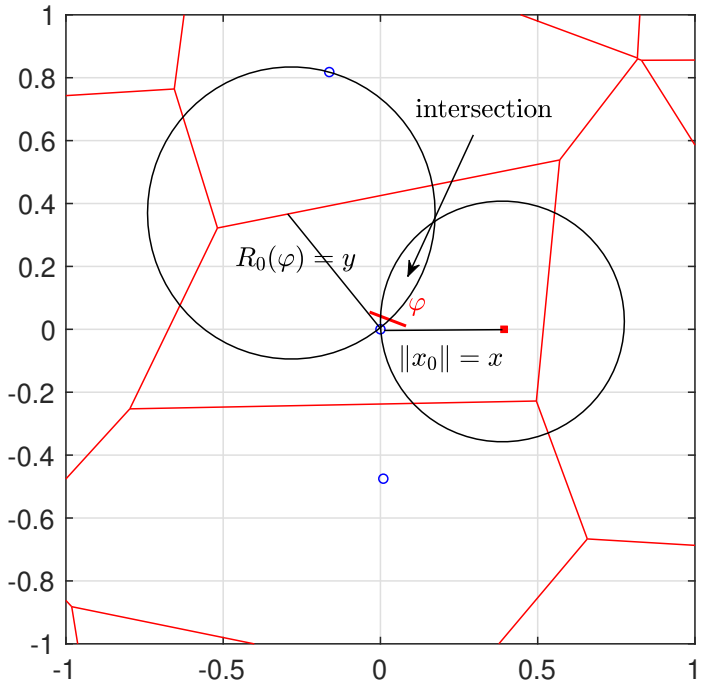

Figure 4.3. Illustration of the intersection between $b((x,0),x)$ and $b((y,\varphi),y)$ whose area is $S(\varphi,x,y)$.

Theorem 4.5. *The joint pdf of* $D_0, R_0(\varphi), \varphi \in [0,\pi)$ *is*

$$f_{D_0,R_0(\varphi)}(x,y) = 2\lambda\pi x \exp\big(-\lambda\pi(x^2+y^2) + \lambda S(\varphi,x,y)\big)\left(2\lambda\pi y - \lambda\frac{\partial S(\varphi,x,y)}{\partial y}\right), \tag{4.6}$$

for $x \geq 0,\ y \geq 0$ *when* $\varphi \neq 0$, *and for* $y \geq x \geq 0$ *when* $\varphi = 0$, *and*

$$S(\varphi,x,y) = (\pi-\varphi)x^2 + (y^2-x^2)\arccos\frac{y - x\cos\varphi}{\sqrt{x^2+y^2-2xy\cos\varphi}} - xy\sin\varphi. \tag{4.7}$$

Proof. The event $R_0(\varphi) > y$ given $\|x_0\| = x$ is equivalent to there being no point in $b((y,\varphi),y) \setminus b((x,0),x)$. Hence

$$\mathbb{P}(R_0(\varphi) > y \mid D_0 = x) = \exp\big(-\lambda(\pi y^2 - S(\varphi,x,y))\big), \tag{4.8}$$

where $S(\varphi, x, y)$ in (4.7) is the area of the intersection of $b((x,0),x)$ and $b((y,\varphi),y)$, *i.e.*, $S(\varphi,x,y) = |b((x,0),x) \cap b((y,\varphi),y)|$.

Hence the conditional pdf of $R_0(\varphi)$ given D_0 is

$$f_{R_0(\varphi)|D_0}(y \mid x) = \exp\big(-\lambda\pi y^2 + \lambda S(\varphi,x,y)\big)\left(2\lambda\pi y - \lambda\frac{\partial S(\varphi,x,y)}{\partial y}\right). \tag{4.9}$$

From the void probability of the PPP we know that

$$f_{D_0}(x) = 2\lambda\pi x \exp(-\lambda\pi x^2).$$

Applying the Bayesian rule $f_{D_0,R_0(\varphi)D_0}(x,y) = f_{R_0(\varphi)|D_0}(y \mid x) f_{D_0}(x)$ we obtain (4.6).

□

Fig. 4.3 illustrates the directional radius $R_0(\varphi)$ and the intersection region.

Remark 4.3. *Integrating (4.6) over x we obtain the distribution for $R_0(\varphi), \varphi \in [0,\pi]$. A straightforward extension of Theorem 4.5 is the joint distribution of $R_0(\varphi_1), R_0(\varphi_2), D_0$ for $\varphi_1 \in [0,\pi], \varphi_2 \in [0,\pi]$, which involves the intersection of three open balls. Such an extension is needed when evaluating the second moment of $|\tilde{V}_0|$ but is omitted here.*

Corollary 4.6. *The pdf of $R_0(0)$ is*

$$f_{R_0(0)}(y) = 2(\lambda\pi)^2 y^3 \exp\left(-\lambda\pi y^2\right), \tag{4.10}$$

and the pdf of $R_0(0) - D_0$ is

$$f_{R_0(0)-D_0}(y) = \sqrt{\lambda}\pi \operatorname{erfc}\left(y\sqrt{\lambda\pi}\right). \tag{4.11}$$

The pdf of $R_0(\pi)$ is

$$f_{R_0(\pi)}(y) = 2\lambda\pi y \exp\left(-\lambda\pi y^2\right). \tag{4.12}$$

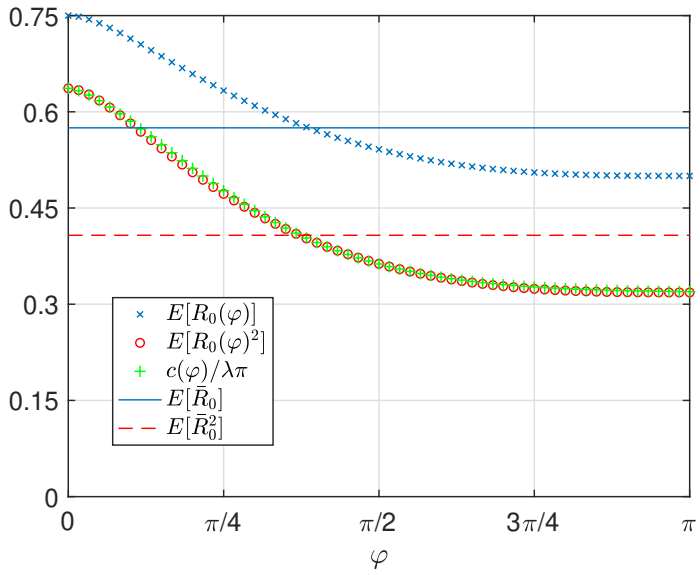

Figure 4.4. First two moments of the directional radius ($R_0(\varphi)$) via Theorem 4.5 and the uniform-angled radius ($\bar{R}_0$) in the 0-cell, $\lambda = 1$. The green curve, $c(\varphi)/\lambda\pi$, is given in (4.20).

Further, D_0 and $R_0(\pi)$ are iid.

Proof. Letting $\varphi = 0$, the joint distribution of D_0, $R_0(0)$ is

$$f_{R_0(0),D_0}(x,y) = (2\lambda\pi)^2 xy \exp\left(-\lambda\pi y^2\right), \quad y \geq x \geq 0. \tag{4.13}$$

So the pdf of $R_0(0)$ is

$$f_{D_o}(y) = \int_0^y (2\lambda\pi)^2 xy \exp\left(-\lambda\pi y^2\right) \mathrm{d}x = 2(\lambda\pi)^2 y^3 \exp\left(-\lambda\pi y^2\right). \tag{4.14}$$

The ccdf of $R_0(0) - D_0$ given D_0 can be written as

$$\mathbb{P}(R_0(0) - D_0 > y \mid D_0 = x) = \mathbb{P}(R_0(0) > x + y \mid D_0 = x) = \exp(-\lambda\pi(y^2 + 2xy)). \tag{4.15}$$

and

$$f_{R_0(0)-D_0|D_0}(y \mid x) = 2\lambda\pi(x+y)\exp(-\lambda\pi(y^2+2xy)). \tag{4.16}$$

The joint distribution of $R_0(0)$, $R_0(0) - D_0$ is

$$f_{R_0(0),R_0(0)-D_0}(x,y) = (2\lambda\pi)^2 x(x+y)\exp\left(-\lambda\pi(x+y)^2\right), \tag{4.17}$$

which gives the pdf of $R_0(0) - D_0$ as

$$f_{R_0(0)-D_0}(y) = (2\lambda\pi)^2 \int_0^\infty x(x+y)\exp\left(-\lambda\pi(x+y)^2\right)\mathrm{d}x = \sqrt{\lambda}\pi\,\mathrm{erfc}\left(y\sqrt{\lambda\pi}\right). \tag{4.18}$$

For $\varphi = \pi$, we obtain $S(\pi, x, y) = 0$, $\frac{\partial S(\pi,x,y)}{\partial y} = 0$. $f_{D_0,R_0(\pi)}(x,y) = f_{D_0}(x) f_{R_0(\pi)}(y)$. Thus, D_0 and $R_0(\pi)$ are iid. □

From Corollary 4.6, we obtain $\mathbb{E}(R_0(0)) = 3/(4\sqrt{\lambda})$, $\mathbb{E}(R_0(\pi)) = 1/(2\sqrt{\lambda})$, and $\mathbb{E}(R_0(0) - D_0) = 1/(4\sqrt{\lambda})$. Thus, $R_0(0)$ is on average exactly 50% larger than $R_0(\pi)$.

The correlation coefficient of R_0 and $R_0(0) - D_0$ follows as

$$\rho_{R_0,R_0(0)-D_0} = \frac{8-3\pi}{\sqrt{12-3\pi}\sqrt{16-3\pi}} \approx -0.3462.$$

Also, $\mathbb{E}((R_0(0) - D_0)/D_0) = 1$, but $\mathbb{E}(R_0(0) - D_0)/\mathbb{E}(D_0) = 1/2$.

Corollary 4.7. *The pdf of* $\bar{R}_0$ *is*

$$f_{\bar{R}_0}(y) = \frac{1}{\pi}\int_0^\pi f_{R_0(\varphi)}(y)\mathrm{d}\varphi. \tag{4.19}$$

Proof. Combine $\Theta \sim \text{uniform}[0, 2\pi]$ and Theorem 4.5. □

$\mathbb{E}\bar{R}_0 = \mathbb{E}[\int_0^\pi R_0(\varphi)\mathrm{d}\varphi]/\pi = 0.5753/\sqrt{\lambda}$.

Remark 4.4. *The mean area of the 0-cell is*

$$\mathbb{E}|\tilde{V}_0| = \int_0^{\pi} \mathbb{E}(R_0^2(\varphi))\mathrm{d}\varphi = \frac{1.280176}{\lambda}.$$

Further,

$$\mathbb{E}(R_0^2(\varphi)) \approx \frac{c(\varphi)}{\lambda\pi}, \tag{4.20}$$

where $c(\varphi) = 1 + \exp(-\varphi^{3/2})$*, is a good approximation to the second moment of the directional radius. It gives a mean area of*

$$1 + \frac{2\Gamma_{\mathrm{inc}}(2/3, \pi^{3/2})}{3\pi} \approx 1.2869,$$

where $\Gamma_{\mathrm{inc}}(a, z) = \int_0^z e^{-t}t^{a-1}\mathrm{d}t$ *is the lower incomplete gamma function*[3]*.*

Fig. 4.4 shows the first two moments of $R_0(\varphi),\ \varphi \in [0, \pi]$ and $\bar{R}_0$; it also shows the approximation $\mathbb{E}R_0^2(\phi) \sim c(\varphi)/(\lambda\pi)$ is quite good. This new approach for evaluating the mean area is easy to understand. By comparison, the existing approach is based on the first two moments of the area of the typical cell and the statistical relation between V_0 and $V(o)$ [74, 75], which we discuss in the next subsection.

4.3.4 Relation of the Typical Cell and the 0-Cell

Fundamentally, the typical cell and the zero-cell are related by [84]

$$\mathbb{E}\big[f(V_0)\big] = \frac{\mathbb{E}^o\big[|V(o)|f(V(o))\big]}{\mathbb{E}^o\big[|V(o)|\big]}, \tag{4.21}$$

where f is any translation-invariant non-negative function on compact sets, and $\mathbb{E}^o$ denotes the expectation with respect to the Palm distribution [7]. In words, a translation-invariant statistic of the 0-cell is that of the typical cell weighted by

[3]In Matlab, $\Gamma_{\mathrm{inc}}(2/3, \pi^{3/2})$ is expressed as `gammainc(pi^1.5,2/3)*gamma(2/3)`.

volume (area in 2D). Letting $f(\cdot) = |\cdot|$, the mean area of the zero-cell is

$$\mathbb{E}\big[|V_0|\big] = \lambda \mathbb{E}^o\big[|V(o)|^2\big]. \tag{4.22}$$

Using Robbin's formula, $\mathbb{E}^o\left(|V(o)|^2\right) = \int_{\mathbb{R}^4} \mathbb{P}\left(x_0, x_1 \in V(o)\right) \mathrm{d}x_0 \mathrm{d}x_1$ [74] [75]. It is apparent that the 0-cell is not just a typical cell enlarged by 28%. In fact, larger cells in the PVT are associated with being more circular and having more sides [85]. To compare the typical cell and the 0-cell, we consider the number of sides of the typical cell and the 0-cell, denoted by N and N_0. We have $\mathbb{E}N_0 = \lambda \mathbb{E}^o[|V(o)|N] \geq \mathbb{E}N = 6$ due to the positive correlation between the area and number of sides of Poisson Voronoi cells [2, Chap 9]. Table 4.1 shows some mean values related to the typical cell and the 0-cell for $\lambda = 1$. Results obtained via simulations are marked by (*).

TABLE 4.1

SOME MEAN VALUES OF THE TYPICAL CELL AND THE ZERO-CELL IN THE PVT.

Cell Type	Number of Sides	Area	Directional Radius	Distance to a Uniformly Random Location
Typical cell	$\mathbb{E}N = 6$	$\mathbb{E}\|V(o)\| = 1$	$\mathbb{E}R(0) = 0.67$ (*), $\mathbb{E}R(\pi) = 0.432$ (*)	$\mathbb{E}D = 0.447$ (*)
Zero-cell	$\mathbb{E}N_0 = 6.41$ (*)	$\mathbb{E}\|V_0\| \approx 1.28$	$\mathbb{E}R_0(0) = 0.75$, $\mathbb{E}R_0(\pi) = 0.5$	$\mathbb{E}D_0 = 0.5$

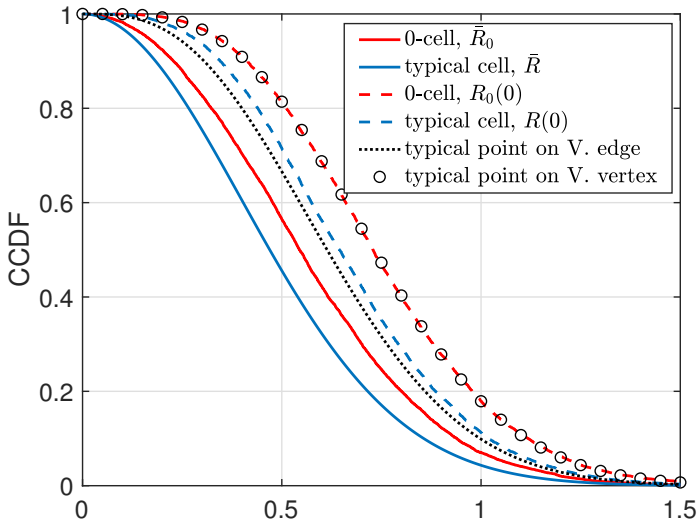

Figure 4.5. Distribution of distances in the 0-cell and the typical cell, $\lambda = 1$.

4.3.5 Gamma-Type Results

We now compare our results with some known distributions. Corollary 4.6 shows that $\pi R_0^2(0) \sim \Gamma(2, \lambda)$; it is known that $\|x_1\|$, the distance between the origin and its second-nearest point, satisfies $\pi\|x_1\|^2 \sim \Gamma(2, \lambda)$ [86]. Hence $R_0(0)$ and $\|x_1\|$ are identical in distribution. The explanation is as follows: for the PPP, the stopping set defined as the minimum disk containing n Poisson points is $\Gamma(n, \lambda)$ distributed [82]. Further, the probability that a point is covered by a stopping set does not depend on whether it is a point of the process or not. In our cases, both $\pi R_0^2(0)$ and $\pi\|x_1\|^2$ are defined by two Poisson points. Denote the distance from the typical point on the edge to its closest Poisson point by R_{e} and the distance from the typical point on the Voronoi vertex to its closest Poisson point by R_{v}. It is shown in [78, 79] that $\pi R_{\mathrm{e}}^2 \sim \Gamma(3/2, \lambda)$, and $\pi R_{\mathrm{v}}^2 \sim \Gamma(2, \lambda)$, which gives $f_{R_{\mathrm{e}}}(r) = 4\lambda^{3/2}\pi r^2 e^{-\lambda\pi r^2}$, and $f_{R_{\mathrm{v}}}(r) = 2(\lambda\pi)^2 r^3 e^{-\lambda\pi r^2}$. Hence $R_0(0)$ and R_v are identical in distribution. Fig. 4.5 shows the ccdf of the distributions given in Lemma 4.4, Theorems 4.5, 4.7, and the distributions of R_{e} and R_{v}.

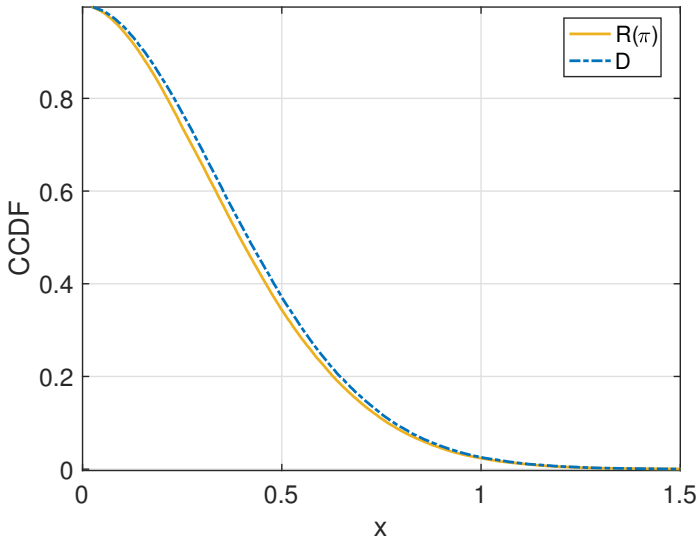

Figure 4.6. The distribution of D and $R(\pi)$, $\lambda = 1$, via simulation.

4.3.6 Discussion and Impact of Cell Asymmetry

From the results on the directional radii, it is apparent that the Poisson Voronoi cells are, quite surprisingly, rather asymmetric around their nucleus. We summarize them in the facts below.

Fact 1. For the zero-cell, the mean radius in the direction of the typical user is 50% larger than the mean radius in the opposite direction, i.e., $\mathbb{E}\left(R_0(0)\right)/\mathbb{E}\left(R_0(\pi)\right) = 3/2$. The typical user is at the same distance on average as an edge user in the opposite direction, since $R_0(\pi)$ and D_0 are iid. Further, we can infer from Fig. 4.4 that about a quarter of edge users (those with $\varphi \geq 3\pi/4$) are at essentially the same distance as the typical user.

Fact 2. For the typical cell, numerical results from Table I suggest that $\mathbb{E}R(\pi)$ is 3% smaller than $\mathbb{E}D$. The ccdf of D and $R(\pi)$ are plotted in Fig. 4.6, which shows that the two curves are almost identical. In the one-dimensional case where $\varphi \in \{0, \pi\}$, the distribution of $R(\pi)$, derived in Appendix B, is identical to the distribution of D, derived in [76, Theorem 1]. Further, we can infer from Fig. 4.2 that about a

quarter of edge users (those with $\varphi \geq 3\pi/4$) are at essentially the same distance as the uniformly random user.

In addition, the distance from the typical BS to the nearest edge location, $R_{\min}$, is distributed as $f_{R_{\min}}(r) = 8\lambda\pi r e^{-4\lambda\pi r^2}$ as it is half the nearest-neighbor distance in the PPP. Since $\mathbb{E}(\pi R_{\min}^2) = 1/4$, 3/4 of the interior users are farther from the nucleus than the nearest edge user. And $\mathbb{E}(R_{\min})$ is only 37% of the mean distance in the direction of the uniformly random user.

These facts may prompt us to rethink some assumptions that are generally made, such as the claim that edge users necessarily suffer from low signal strength. Also, care is needed when evaluating the performance of non-orthogonal multiple access (NOMA) schemes, especially if "cell-center" refers to a user located uniformly at random in the cell and "cell-edge" refers to a user located uniformly at random on the edge of the cell. In this case, simply pairing a cell-center user as the strong user and an edge user as the weak one may be quite inefficient, since the edge user may be closer to the BS than the "cell-center" user. Conversely, if "cell-center" and "cell-edge" are defined based on relative distances between serving and interfering base stations as in Chapter 3, then a "cell-edge" user may actually be quite far from the edge of the cell. A potential model to pair users for Poisson Voronoi cells is to select a "cell-center" user uniformly at random inside the cell, and select an edge user whose angle differs only slightly from that of the "cell-center" user. This increases the likelihood of significant channel gain difference between users and thus increases the NOMA gain. An alternative model that guarantees the intended ordering of strong and weak user is to place the two randomly in the in-disk of the cell and then order them [87].

4.4 JSP Model

In this section, we introduce the JSP model and the performance metrics. We also recall some relevant results of previous models.

4.4.1 System Model

Let $\Phi \subset \mathbb{R}^2$ be a stationary point process with intensity λ modeling BS locations. We refer to the JSP model for a specific type of BS point processes named x as the "JSP-x" model. For instance, " JSP-PPP" refers to the JSP model when Φ is a PPP. The typical user is located at the origin without loss of generality. We assume all BSs are active and transmit with unit power. For $x \in \Phi$, denote by h_x and K_x the power of the small-scale iid Rayleigh fading with unit mean and the large-scale shadowing between x and the origin, respectively. The power-law path loss model is considered, *i.e.*, $\ell(x) = \|x\|^{-\alpha}$, where $\alpha > 2$ is a constant.

Let $r(x)$ be the distance from $x \in \Phi$ to its Voronoi cell edge oriented towards the typical user. Let $\{x_i\}_{i\in\mathbb{N}}$ be the point process ordered by the distance to the origin, *i.e.*, $x_1 \triangleq \arg\min_{x\in\Phi}\{\|x\|\}$ and so on. Note that $r(x_1)$ is the same as $R_0(0)$ defined in the last section. Fig. 4.7 shows a realization of Φ and the corresponding $r(x_1),\ r(x_2)$. By the construction of the Voronoi cells, $r(x_1) \geq \|x_1\|$ and $r(x_i) \leq \|x_i\|,\ i \geq 2$.

Definition 4.8 (Cell-Dependent Shadowing)**.** *In cell-dependent shadowing, the coefficients $\{K_x\}_{x\in\Phi}$ have the property that given Φ, users at the Voronoi cell boundaries receive an expected power P_0, i.e.,*

$$\mathbb{E}[K_x r(x)^{-\alpha} \mid \Phi] = P_0. \tag{4.23}$$

We further assume that $\{K_x\}_{x\in\Phi}$ are conditionally independent (given Φ) log-normal

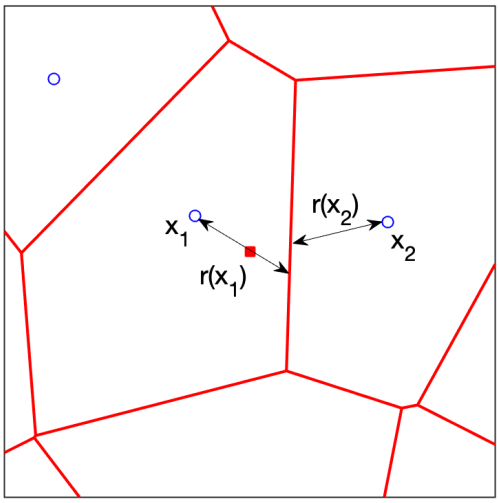

Figure 4.7. An illustration of the JSP model with cell-dependent shadowing. Blue circles are BS locations generated from a PPP. Red lines are the Voronoi tessellation. The typical user is denoted by the red square.

random variables. We denote by μ_x *and* σ_x *the mean and standard deviation*[4] *of* $\log(K_x)$ *conditioned on* Φ*, and we fix* $\sigma_x \equiv \sigma$ *for* $\forall x \in \Phi$.

The log-normal model is commonly used to capture the distribution of shadowing and thus allows us to compare this model with previous models. We have $\exp(\mu_x + \sigma^2/2) = P_0 r(x)^\alpha$, which gives $\mu_x = \log(P_0 r(x)^\alpha) - \sigma^2/2$. Depending on whether $\sigma = 0$ or $\sigma > 0$, $\{K_x\}_{x\in\Phi}$ is a deterministic function of Φ or a set of random variables correlated with Φ.

For $\sigma = 0$, $\{K_x\}_{x\in\Phi}$ is a deterministic function of Φ. In this case, we have

$$K_x = P_0 r(x)^\alpha. \tag{4.24}$$

[4]Instead of denoting the standard deviation of the noise in the previous chapters, σ denotes the standard deviation of shadowing coefficients in this chapter.

Users located at the Voronoi cell edges receive a signal power P_0 (averaged over small-scale fading).

For $\sigma > 0$, the shadowing in the JSP model is doubly random such that the power averaged over small-scale fading along the cell edge fluctuates around P_0. In this case, we have

$$\mathbb{E}[K_x \mid \Phi] = P_0 r(x)^{\alpha}. \tag{4.25}$$

The JSP model for a deterministic BS point process ϕ (such as a realization of a PPP) can be defined similarly by removing the conditioning on the BS point process.

Remark 4.5. *The JSP model in [68] assumes $r(x)^{-\alpha(x)} = P_0$, which is sensitive to P_0 and λ due to the singularity of the path loss model as mentioned earlier. Our model avoids this deficiency while generalizing several models in the literature: if $P_0 = r(x)^{-\alpha}$ in (4.23), we retrieve the iid shadowing model in [72]; if further $\sigma = 0$, we retrieve the traditional model without shadowing (or constant shadowing) in [12].*

4.4.2 Performance Metrics

We consider the strongest-BS association throughout this paper. Let $x \in \Phi$ be the serving BS, *i.e.*, the BS from which the user receives the strongest signal averaged over small-scale fading. We consider the SIR, defined as

$$\mathrm{SIR} \triangleq \frac{S}{I} = \frac{h_x K_x \|x\|^{-\alpha}}{\sum_{y \in \Phi \setminus \{x\}} h_y K_y \|y\|^{-\alpha}}. \tag{4.26}$$

4.4.2.1 Asymptotic Gain

Here, the MISR is

$$\mathrm{MISR} = \mathbb{E}\Bigg[\sum_{y \in \Phi \setminus \{x\}} \frac{K_y \|y\|^{-\alpha}}{K_x \|x\|^{-\alpha}} \Bigg].$$

Throughout this paper, we use the PPP model without shadowing as the baseline for comparison. Denoting the asymptotic gain by G, we have

$$G = \frac{\mathrm{MISR}_{\mathrm{PPP}}}{\mathrm{MISR}}. \tag{4.27}$$

4.4.2.2 Meta Distribution

For Rayleigh fading, the conditional success probability is

$$\begin{aligned} P_{\mathrm{s}}(\theta) &\triangleq \mathbb{P}(\mathrm{SIR} > \theta \mid \Phi, \{K_y\}_{y\in\Phi}) \\ &= \mathbb{P}\Big(h_x K_x \|x\|^{-\alpha} > \theta \sum_{y\in\Phi\setminus\{x\}} h_y K_y \|y\|^{-\alpha} \;\Big|\; \Phi, \{K_y\}_{y\in\Phi}\Big) \\ &= \mathbb{E}\Big[\exp\Big(-\theta \sum_{y\in\Phi\setminus\{x\}} h_y \frac{K_y\|y\|^{-\alpha}}{K_x\|x\|^{-\alpha}}\Big) \;\Big|\; \Phi, \{K_y\}_{x\in\Phi}\Big] \\ &\overset{(a)}{=} \prod_{y\in\Phi\setminus\{x\}} \frac{1}{1+\theta(\|x\|/\|y\|)^{\alpha} K_x/K_y}. \end{aligned}$$

4.4.2.3 Path Loss Point Process

We define the path loss point process for a general BS point process Φ to be $\Pi \triangleq \{K_x/\|x\|^{\alpha}\}_{x\in\Phi}$. For deterministic point processes, we use ϕ instead of Φ. To avoid a colocated BS and user, we assume no BS is located at the origin. The path loss point process, introduced in [88], characterizes the received signal strengths (averaged over small-scale fading) from all transmitters in the network from the viewpoint of the typical user. It is also referred to as the "signal spectrum" in [73], or the "propagation process" in [72].

4.4.3 Relevant Results

In the baseline model, it is assumed that shadowing is constant for all transmissions, *i.e.*, $K_x \equiv 1,\ x \in \Phi$. The nearest BS also provides the strongest signal (averaged over fading). It is known that for the PPP, $M_b(\theta) = 1/{}_2F_1(b, -\delta; 1-\delta; -\theta)$

[23], $b \in \mathbb{C}$, where ${}_2F_1$ is the hypergeometric function. The triangular lattice has a 3.4 dB asymptotic gain over the PPP [67].

In the iid log-normal shadowing model [72], it is assumed that $\log K_x \sim \mathcal{N}(\mu, \sigma^2)$, $x \in \Phi$, where $\mu = -\sigma^2/2$ to normalize $\mathbb{E}K_x$. It is shown in [89] that the path loss point process of the PPP with iid shadowing is again a PPP. Thus, under the strongest-BS association, the performance of the iid log-normal shadowing model for the PPP is the same as the baseline PPP model. Further, [72] shows that in the iid log-normal shadowing model for any deterministic/stochastic BS point processes satisfying a homogeneity constraint, the path loss point process converges to that of a PPP when $\sigma \to \infty$. [73] proves that this conclusion also holds for moderately correlated shadowing.

4.5 Performance Analysis

In this section, we analyze the performance of the JSP-PPP model. We focus on the distribution of the serving signal, shadowing distribution/correlation, the asymptotic SIR gain, the SIR meta distribution, and finally the path loss point process. We first introduce the lemma below.

Lemma 4.9. *For a Poisson point process with intensity λ, the ccdf of $r(x_i)/\|x_i\|$, $i \geq 2$ is*

$$\mathbb{P}(r(x_i)/\|x_i\| > t) = (1-t^2)^i, \quad t \in [0,1], \tag{4.28}$$

and the ccdf of $r(x_i)$ is

$$\mathbb{P}(r(x_i) > t) = \exp(-\lambda \pi t^2). \tag{4.29}$$

Proof. Recall that x_i is the i-th closest point to the origin. Let $\Phi(b(o,r))$ denote the number of points in Φ falling in the disk of radius r centered at the origin. For

$t \in [0,1]$,

$$\begin{aligned}
&\mathbb{P}(r(x_i)/\|x_i\| > t) \\
&= \mathbb{E}\mathbb{P}(r(x_i) > \|x_i\| t \mid \|x_i\|) \\
&\overset{(a)}{=} \mathbb{E}\mathbb{P}(\Phi(b(o,\|x_i\|t)) = 0 \mid \Phi(b(o,\|x_i\|)) = i) \\
&\overset{(b)}{=} \mathbb{E}\left(\frac{\|x_i\|^2 - \|x_i\|^2 t^2}{\|x_i\|^2}\right)^i \\
&= (1-t^2)^i.
\end{aligned}$$

Step (a) holds since the probability of having no point inside a disk only depends on the radius of the disk, not on the disk center. Step (b) follows from the property of the PPP, where conditioned on $\|x_i\|$, the i points are distributed uniformly at random in $b(o,\|x_i\|)$. Combining (4.28) with the distribution of $\|x_i\|$ [86] we obtain the ccdf for $r(x_i)$, $i \geq 2$, in (4.29). □

4.5.1 The Serving Signal

For $\sigma = 0$, x_1 is the strongest BS. Hence $\mathbb{E}_h[S] = K_{x_1}\|x_1\|^{-\alpha}$. We have

$$\begin{aligned}
\mathbb{P}(K_{x_1}\|x_1\|^{-\alpha} > t) &= \mathbb{P}(P_0 r(x_1)^\alpha \|x_1\|^{-\alpha} > t) \\
&= \mathbb{P}(\|x_1\|/r(x_1) < (P_0/t)^{1/\alpha}) \\
&\overset{(a)}{=} P_0^\delta t^{-\delta}, \quad t \geq P_0,
\end{aligned} \tag{4.30}$$

where $t \geq P_0$ due to the minimum received power constraint. Step (a) follows from Lemma 4.3. The distribution of $K_{x_1}\|x_1\|^{-\alpha}$ does not depend on Φ, and it is equal to the distribution of the signal power in a circular cell where the received power at the cell edge is P_0. We further obtain the tail of the ccdf of S in the lemma below.

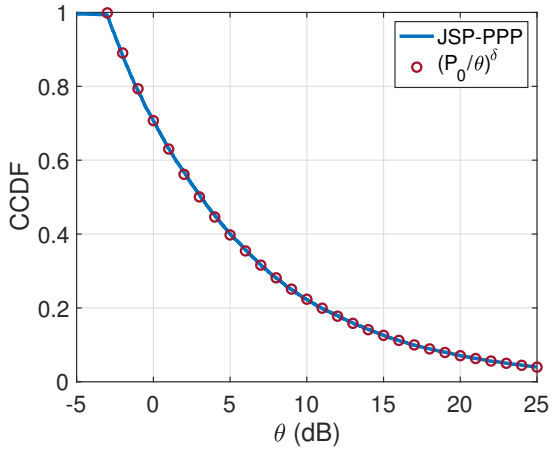

(a) JSP-PPP, $\sigma = 0,\ \lambda = 10^{-2}$.

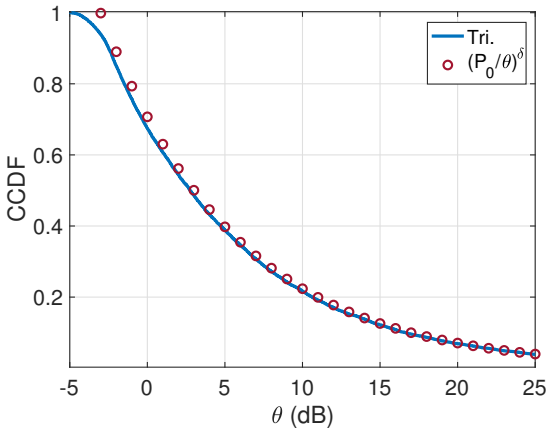

(b) Triangular lattice.

Figure 4.8. The distribution of $\mathbb{E}_h[S]$. $P_0 = 0.5$, $\alpha = 4$.

Lemma 4.10. *For the JSP model with any BS process and $\sigma = 0$,*

$$\mathbb{P}(S > t) \sim P_0^\delta \mathbb{E}(h^\delta) t^{-\delta}, \quad t \to \infty. \tag{4.31}$$

Proof.

$$\begin{aligned}
\mathbb{P}(S > t) &= \mathbb{P}(P_0 h_{x_1} r(x_1)^\alpha \|x_1\|^{-\alpha} > t) \\
&= \mathbb{P}(\|x_1\|/r(x_1) < (P_0 h_{x_1}/t)^{1/\alpha}) \\
&\sim P_0^\delta \mathbb{E}(h^\delta) t^{-\delta}, \quad t \to \infty.
\end{aligned}$$

□

In [47, Lemma 7], it is shown that for the baseline model (without shadowing), the tail of the ccdf of the desired signal strength for all stationary point processes is $\mathbb{P}(S > t) \sim \lambda\pi\mathbb{E}(h^\delta)t^{-\delta},\ t \to \infty$. If we let

$$P_0 = (\lambda\pi)^{1/\delta}, \tag{4.32}$$

we obtain the same tails. Intuitively, if we could "pack" the space with congruent circular cells, we would have $r^{-\alpha} = (1/\lambda\pi)^{-\alpha/2} = (\lambda\pi)^{1/\delta} = P_0$.

Fig. 4.8a shows the distribution of $\mathbb{E}_h[S]$ for the JSP-PPP model and (4.30) with $\sigma = 0,\ \lambda = 10^{-2},\ P_0 = 0.5$, and $\alpha = 4$. Fig. 4.8b shows that we can use $(P_0\theta)^{-\delta}$ to approximate the distribution of the signal from the nearest BS in triangular lattices, which is not surprising considering that hexagonal cells and circular cells are similar in shape. Note that for lattices, the minimum average received power is determined by the radius of the smallest disk containing the cell, or, equivalently, the intensity of the point process. Thus, the intensity of the triangular lattice in Fig. 4.8b is scaled for a fair comparison.

For $\sigma > 0$, the serving BS $x = \arg\max_{y\in\Phi}\{K_y\|y\|^{-\alpha}\}$.

$$\begin{aligned}
&\mathbb{P}(K_x\|x\|^{-\alpha} < t) \\
&= \mathbb{P}(K_y\|y\|^{-\alpha} < t, y \in \Phi) \\
&= \mathbb{E}\prod_{y\in\Phi}\mathbb{P}(K_y < \|y\|^{\alpha}t \mid \Phi) \\
&= \mathbb{E}\prod_{y\in\Phi}\left(\frac{1}{2} + \frac{1}{2}\,\mathrm{erf}\left[\frac{\log t\|y\|^{\alpha} - \log P_0 r(y)^{\alpha} + \sigma^2/2}{\sqrt{2}\sigma}\right]\right).
\end{aligned} \tag{4.33}$$

4.5.2 Shadowing Coefficients

4.5.2.1 Distribution

For $\sigma = 0$, the shadowing coefficient from any BS is a deterministic function of the cell radius of that BS oriented towards the origin. For the serving cell,

$$\mathbb{P}(K_{x_1} \geq t) = \exp\left(-\lambda\pi t^{\delta}P_0^{-\delta}\right)(1 + \lambda\pi t^{\delta}P_0^{-\delta}), \tag{4.34}$$

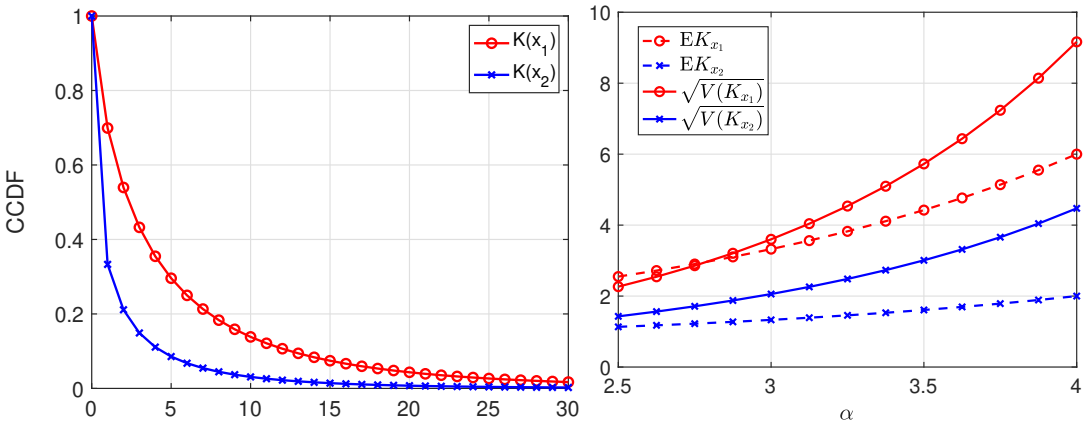

(a) Ccdfs of the shadowing per (4.34) and (4.35).

(b) Mean and standard deviation. $P_0 = (\lambda\pi)^{\alpha/2}$.

Figure 4.9. Ccdfs, means, and standard deviations of K_{x_1} and K_{x_2}, $\sigma = 0$, $\lambda = 1$, $\alpha = 4$.

and

$$\mathbb{P}(K_{x_i} \geq t) = \exp\left(-\lambda\pi t^{\delta} P_0^{-\delta}\right), \tag{4.35}$$

which follow from the distribution of $r(x_1)$ and $r(x_i), i \geq 2$, in Theorem 4.5 and Lemma 4.9, respectively.

Based on (4.34) and (4.35), $\mathbb{E}[K_{x_1}] = P_0(\lambda\pi)^{-\alpha/2}\Gamma(\alpha/2+2)$. $\mathbb{E}[K_{x_i}] = P_0(\lambda\pi)^{-\alpha/2} \times \Gamma(\alpha/2+1)$, $i \geq 2$. Denoting by $\mathbb{V}K_{x_i}$ the variance of K_{x_i}, we have $\mathbb{V}K_{x_1} = P_0^2(\lambda\pi)^{-\alpha}(\Gamma(\alpha+2) - \Gamma(\alpha/2+2)^2)$ and $\mathbb{V}K_{x_i} = P_0^2(\lambda\pi)^{-\alpha}(\Gamma(\alpha+1) - \Gamma(\alpha/2+1)^2)$, $i \geq 2$. Fig. 4.9a shows the ccdfs for K_{x_1} and K_{x_2}. Fig. 4.9b shows the mean and standard deviation of K_{x_1} and K_{x_2} versus α based on (4.34) and (4.35). K_{x_1} statistically dominates $K_{x_i}, i \geq 2$, since $r(x_1)$ statistically dominates $r_{x_i}, i \geq 2$.

For $\sigma > 0$, the ccdf of K_{x_i} is

$$\begin{aligned}\mathbb{P}(K_{x_i} \geq t) &= \mathbb{E}\mathbb{P}(K_{x_i} \geq t \mid r(x_i)) \\ &= \frac{1}{2}\mathbb{E}\,\mathrm{erfc}\left(\frac{\log t - \log(P_0 r(x_i)^\alpha) + \sigma^2/2}{\sqrt{2}\sigma}\right),\end{aligned}$$

where the distribution of $r(x_0)$ is given in Theorem 4.5 and the distribution of $r(x_i), i \geq 2$, is given in Lemma 4.9. σ appears in both the denominator and numerator inside of the erfc function. When $\sigma \to \infty$, the impact of $r(x_i)$ diminishes.

4.5.2.2 Correlation

We consider two types of shadowing correlation. The first type is the correlation between the shadowing coefficients from two BSs to the typical user. The second type is the correlation between the shadowing coefficient and the directional radius of a cell. In the proposed JSP model, these two types of correlation are inherently related, *i.e.*, the correlation between shadowing is induced by the correlation between cell radius. If the BS deployment is modeled by a point pattern (*i.e.*, deterministic point process), only the second type of correlation exists.

Let $P_0 = 1$ for simplicity. The correlation coefficient between the shadowing coefficients K_x, K_y (from BS $x, y \in \Phi$) is

$$\rho_{K_x,K_y} = \frac{\mathbb{E}[K_x K_y] - \mathbb{E}K_x \mathbb{E}K_y}{\sqrt{\mathbb{V}K_x}\sqrt{\mathbb{V}K_y}},$$

where $\mathbb{E}[K_x K_y] = \mathbb{E}[r(x)^\alpha r(y)^\alpha]$, $\mathbb{E}K_x = \mathbb{E}[r(x)^\alpha]$, and $\mathbb{V}K_x = \exp(\sigma^2)\mathbb{E}r(x)^{2\alpha} - (\mathbb{E}r(x)^\alpha)^2$. As the distance between two BSs x, y increases, the correlation between $r(x)$ and $r(y)$ vanishes. Hence the locality of the shadowing correlation is preserved. Obviously, $\rho_{K_x,K_y} \leq \rho_{r(x)^\alpha, r(y)^\alpha}$, and the equality holds when $\sigma = 0$. Further, ρ_{K_x,K_y} decreases with σ. For $\sigma \to \infty$, $\rho_{K_x,K_y} \to 0$ for any $x \neq y$.

The correlation between K_x and $r(x)^\alpha$ is

$$\rho_{K_x, r(x)^\alpha} = \sqrt{\frac{\mathbb{V}(r(x)^\alpha)}{\mathbb{V}K_x}},$$

where again, $\mathbb{V}K_x = \exp(\sigma^2)\mathbb{E}r(x)^{2\alpha} - (\mathbb{E}r(x)^\alpha)^2$. $\rho_{K_x, r(x)^\alpha} = 1$ for $\sigma = 0$. For $\sigma \to \infty$, $\rho_{K_x, r(x)^\alpha} \to 0$.

4.5.3 Asymptotic Gain

For $\sigma = 0$,

$$\begin{aligned} \text{MISR} &= \mathbb{E}\left[\frac{\sum_{x\in\Phi\setminus\{x_1\}} K_x \|x\|^{-\alpha}}{K_{x_1}\|x_1\|^{-\alpha}}\right] \\ &= \mathbb{E}\left[\sum_{x\in\Phi\setminus\{x_1\}} \frac{r(x)^\alpha}{r(x_1)^\alpha}\frac{\|x\|^{-\alpha}}{\|x_1\|^{-\alpha}}\right]. \end{aligned}$$

The MISR is independent of P_0 and λ. Fig. 4.10a shows the asymptotic gain (relative to the baseline-PPP model) for the baseline triangular lattice model and the JSP-PPP with $\sigma = 0$. The asymptotic gain increases with α. Fig. 4.10b shows the asymptotic gain G for the JSP-PPP decreases with σ. As discussed in the last subsection, increasing σ decreases the correlation between the shadowing coefficients as well as the correlation between shadowing and cell radius. The figure shows that increasing the variance of the JSP-PPP model is harmful to coverage. Eventually, the JSP-PPP model reverts to the PPP as $\sigma \to \infty$.

4.5.4 Meta Distribution

Fig. 4.11 shows how the conditional success probabilities with a fixed $\theta = 1$ are distributed for the PPP with iid log-normal shadowing and the JSP-PPP model. The strongest-BS association is assumed for both models. For $\sigma = 0$, the region where $P_{\text{s}}(\theta) > 0.8$ appears elliptical around the nucleus for the PPP; while for the JSP-

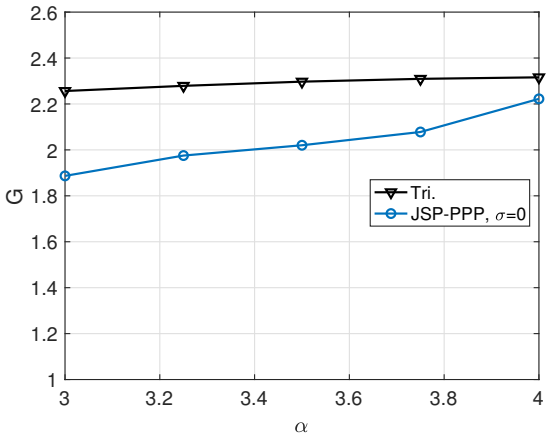

(a) The asymptotic gain for triangular lattices and the JSP-PPP with $\sigma = 0$.

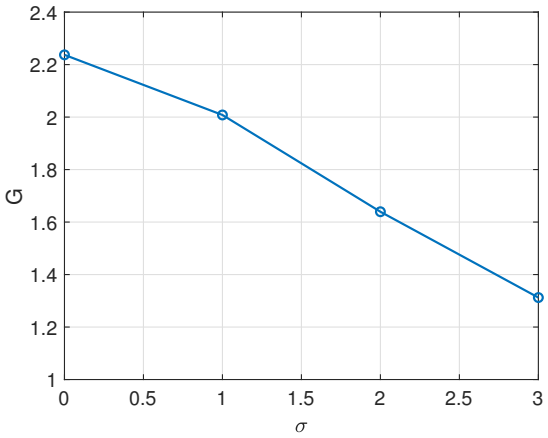

(b) The asymptotic gain for the JSP-PPP with $\sigma = 0, 1, 2, 3$, for $\alpha = 4$.

Figure 4.10. The asymptotic gain of the JSP-PPP model.

PPP, the region where $P_{\mathrm{s}}(\theta) > 0.8$ is enlarged and adapts to the cell shape almost perfectly. For $\sigma = 1$, both regions are blurred due to the shadowing variance, and the JSP-PPP model outperforms the PPP model.

Fig. 4.12 shows the simulation results for the MD of the JSP-PPP model with fixed reliabilities. The MD for the (baseline) triangular lattice and the (baseline) PPP model are plotted for comparison. Under the strongest-signal association, the MD decreases with σ, making a shift from the triangular lattice to the PPP.

Fig. 4.13 plots the first two moments of the conditional success probability for the JSP-PPP model and the triangular lattice with iid log-normal shadowing. The first two moments leads to a good approximation of the MD [23]. Hence the MD for the JSP-PPP model is close to the triangular lattice for a set of different values of σ.

4.5.5 Convergence of the Path Loss Point Process

The path loss point process of the JSP model for a point pattern ϕ is $\Pi = \{\|x\|^{\alpha}/K_x\}_{x\in\phi}$. In this subsection, we show that the path loss point process of the JSP model for any realization of the PPP converges to that of a PPP as $\sigma \to \infty$.

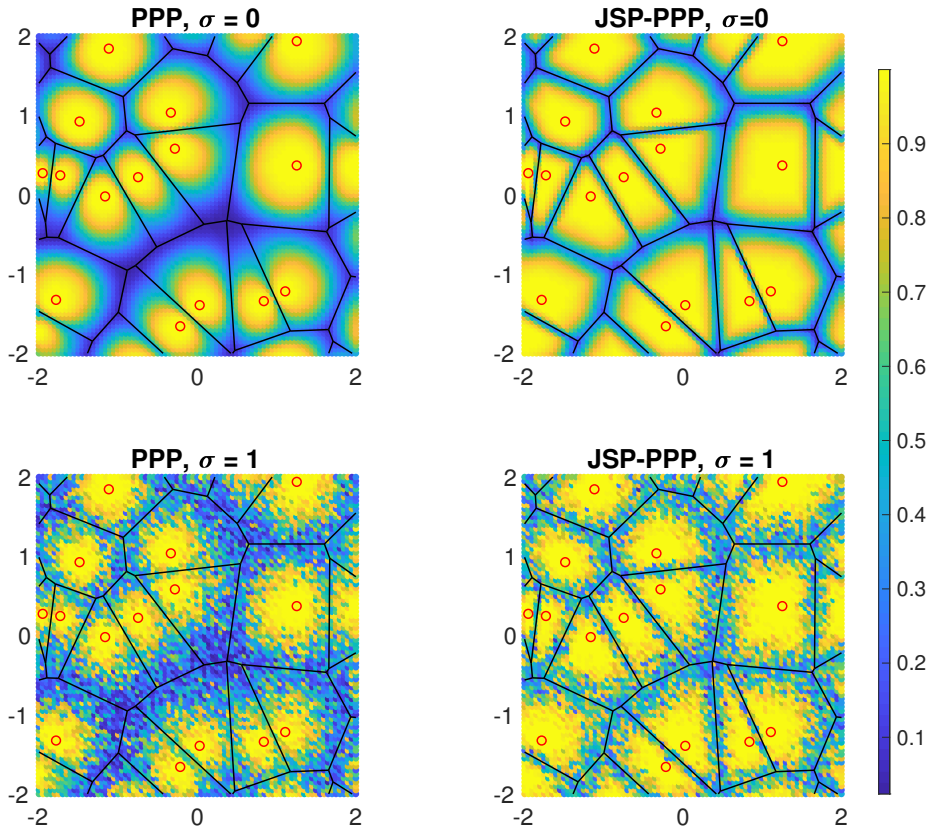

Figure 4.11. Illustration of the conditional success probability for $\theta = 1$ for the PPP and the JSP-PPP with $\sigma = 0, 1$ under the strongest-BS association, $\lambda = 1$, $\alpha = 4$.

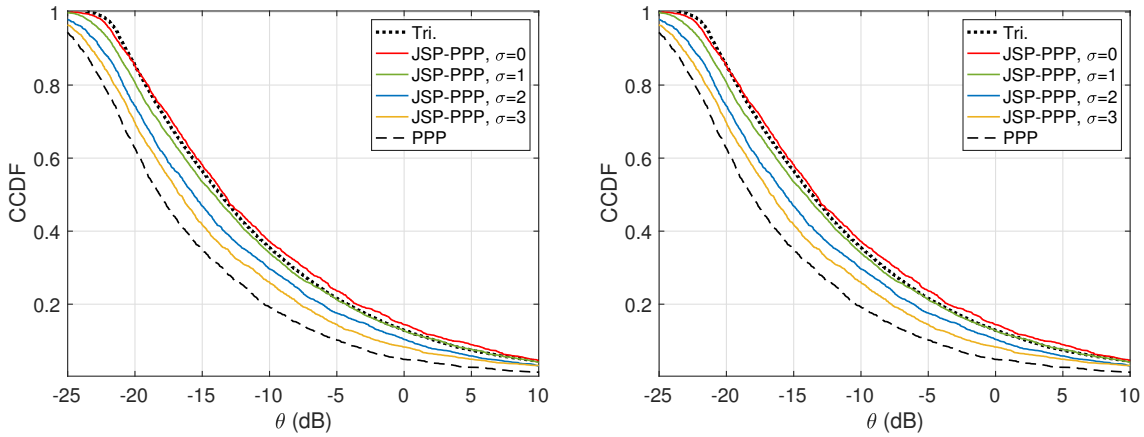

(a) $\bar{F}_{P_s}(\theta, x),\ x = 0.99.$ (b) $\bar{F}_{P_s}(\theta, x),\ x = 0.9.$

Figure 4.12. The MD for the JSP-PPP model with $\sigma = 0, 1, 2, 3$ and $x = 0.9, 0.99$, $\alpha = 4$. The black dashed and dotted curves denote the MD for the PPP and the triangular lattice (without shadowing), respectively.

First we recall a result from [72].

Proposition 4.11. *[72] For any deterministic and locally finite collection of points $\phi \subset \mathbb{R}^2$ without a point at the origin, let the shadowing coefficients, $\{K_x\}_{x\in\phi}$, be iid log-normal random variables with $\mathbb{E}K_x = 1$ and $\mathbb{V}(\log(K_x)) = \sigma^2$. If there is a constant $0 < \lambda < \infty$ such that as $t \to \infty$*

$$\frac{\phi\left(b(o,t)\right)}{\pi t^2} \to \lambda, \tag{4.36}$$

then the path loss point process Π after rescaling by $(\mathbb{E}K_x^{\delta})^{1/\delta} = \exp\left(-\sigma^2(1-\delta)/2\right)$ converges weakly as $\sigma \to \infty$ to that of the PPP on $\mathbb{R}^+$ with intensity measure $\Lambda([0,t)) = \lambda\pi t^2$.

The rescaling of Π by $(\mathbb{E}K_x^{\delta})^{1/\delta}$ is necessary to obtain a non-zero intensity measure as $\sigma \to \infty$. Now, when ϕ be a realization of the PPP, we have the convergence of the path loss point process for the JSP model as follows.

Lemma 4.12. *The path loss point process of the JSP model for any realization of*

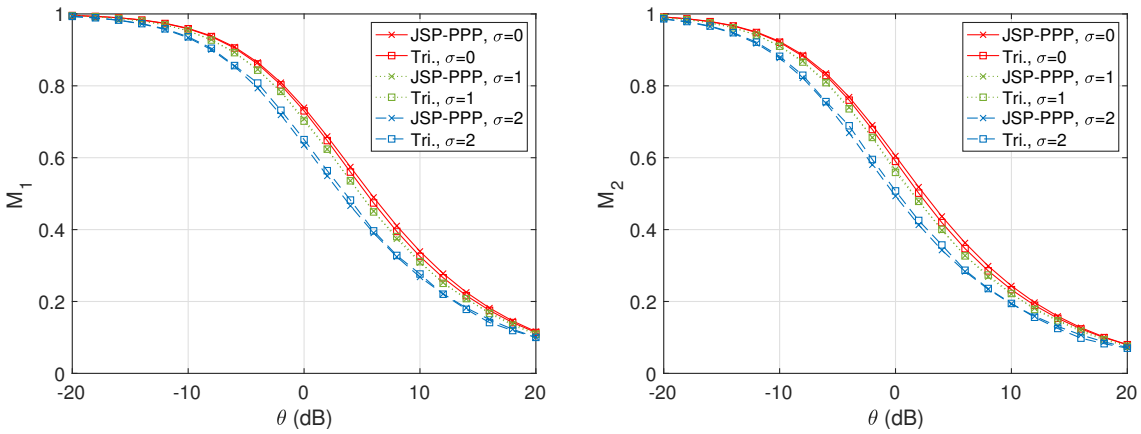

(a) $M_1(\theta)$. (b) $M_2(\theta)$.

Figure 4.13. First two moments of the conditional success probability for JSP-PPP and the triangular lattice with iid shadowing. $\sigma = 0, 1, 2$, $\alpha = 4$.

the PPP after rescaling by $P_0 \exp\left(-\sigma^2(1-\delta)/2\right)$ *converges weakly as* $\sigma \to \infty$ *to that of the PPP on* $\mathbb{R}^+$ *with intensity measure* $\Lambda([0,t)) = t^2$.

Proof. We first show that the JSP model for a point pattern ϕ can be viewed as the iid log-normal shadowing model in Proposition 4.11 with a modified point pattern $\hat{\phi}$. Then we show that when ϕ is a realization of the PPP, its modified BS point pattern $\hat{\phi}$ satisfies the convergence criterion.

For the JSP model, $\{K_x\}_{x\in\phi}$ are independent but not necessarily identically distributed log-normal random variables such that $\mathbb{E}K_x = P_0 r(x)^\alpha$ and $\mathbb{V}(\log(K_x)) = \sigma^2$. We have

$$\Pi = \left\{ x \in \phi \colon \frac{\|x\|^\alpha}{r(x)^\alpha} \frac{1}{K_x / r(x)^\alpha} \right\} = \left\{ x \in \hat{\phi} \colon \frac{\|x\|^\alpha}{\hat{K}_x} \right\},$$

where $\hat{\phi} \triangleq \{x \in \phi \colon x/r(x)\}$ and $\hat{K}_x \triangleq K_x / r(x)^\alpha$. Now $\{\hat{K}_x\}_{x\in\phi}$ are iid log-normal with $\mathbb{E}\hat{K}_x = P_0$ and $\mathbb{V}(\log(\hat{K}_x)) = \sigma^2$. After rescaling of Π by $(\mathbb{E}\hat{K}_x^\delta)^{1/\delta} = P_0 \exp\left(-\sigma^2(1-\delta)/2\right)$, we retrieve the iid shadowing model in [72]. Now it suffices to show that $\hat{\phi}$ satisfies the homogeneity condition (4.36).

For the PPP,

$$\begin{aligned}\mathbb{E}\hat{\Phi}(b(o,t)) &= \mathbb{E}\sum_{i\geq 1}\mathbb{1}(\|x_i\|/r(x_i) < t)\\ &= \sum_{i\geq 1}\mathbb{P}(r(x_i)/\|x_i\| > 1/t)\\ &\overset{(a)}{=} t^2.\end{aligned}$$

Step (a) follows from the ccdf of $r(x_i)/\|x_i\|$ given in Lemma 4.3 and Lemma 4.9. $\mathbb{1}(\cdot)$ is the indicator function. Hence we have $\mathbb{E}\hat{\Phi}(b(o,t))/\pi t^2 = 1/\pi$. By the ergodicity of the PVT, $\lim_{t\to\infty}\hat{\phi}(b(o,t))/\pi t^2 = 1/\pi$. □

4.6 Summary

1. We characterize the shape and size of the Poisson Voronoi cells by introducing the notion of the directional radius in Voronoi tessellations.

2. For the PVT, we derive the exact distributions of the directional radius in the zero-cell and the uniform-angled radius in the typical cell. The results reveal the asymmetry of Poisson Voronoi cells and also lead to a new approach of evaluating the mean cell areas. For cases without an explicit expression, simulation results and approximations are provided.

3. We introduce and study a joint spatial-propagation model for coverage-oriented cellular networks. We consider cell-dependent shadowing where the shadowing coefficients are conditionally log-normal random variables given the BS point process such that users at the cell edges receive an expected power P_0. Hence the JSP model ascribes the irregular deployment of base stations to an intelligent design by the operators, rather than to pure randomness, as is done in most of the literature.

4. This chapter highlights the effect of the variance of the large-scale path loss along the cell boundaries on the network performance. In the limiting case of $\sigma \to \infty$, the path loss point processes for a general class of point processes seem to converge to that of a PPP.

CHAPTER 5

CONCLUSIONS

The inherent randomness of wireless node locations and their interactions through the wireless medium warrants a probabilistic approach to studying wireless networks. Through the stochastic geometry framework, we characterize the interplay between the target reliability, rate, and user percentage using the meta distributions. Further, cooperation between nodes is an effective way to improve the uniformity of user performance. Lastly, cellular network coverage depends mainly on the correlation between the deployment and propagation conditions. For future work, an important future direction is to devise methods to improve the guaranteed performance for (ultra-)high percentage of users in the presence of spatial and temporal randomness and to investigate further if fundamental limits of such guarantees exist. For instance, modeling user traffic patterns can incorporate the temporal randomness. For specific communication scenarios such as machine-type communications, node traffic/activities and the network may be jointly designed to optimize the end-to-end performance.

BIBLIOGRAPHY

1. E. N. Gilbert, "Random plane networks," *Journal of the Society for Industrial and Applied Mathematics*, vol. 9, no. 4, pp. 533–543, 1961.

2. S. N. Chiu, D. Stoyan, W. S. Kendall, and J. Mecke, *Stochastic geometry and its applications*. John Wiley & Sons, 2013.

3. J. Moller, *Lectures on random Voronoi tessellations*, vol. 87. Springer Science & Business Media, 2012.

4. D. J. Daley and D. Vere-Jones, *An introduction to the theory of point processes: volume II: General theory and structure*. Springer Science & Business Media, 2007.

5. R. Meester and R. Roy, *Continuum Percolation*. Cambridge University Press, 1996.

6. M. Haenggi and R. K. Ganti, *Interference in Large Wireless Networks*. Now Foundations and Trends, 2009.

7. M. Haenggi, *Stochastic geometry for wireless networks*. Cambridge University Press, 2012.

8. F. Baccelli and B. Błaszczyszyn, "Stochastic geometry and wireless networks: Volume II applications," *Foundations and Trends in Networking*, vol. 4, no. 1–2, pp. 1–312, 2010.

9. F. Baccelli and B. Błaszczyszyn, "Stochastic geometry and wireless networks: Volume I theory," *Foundations and Trends in Networking*, vol. 3, no. 3–4, pp. 249–449, 2010.

10. B. Blaszczyszyn, M. Haenggi, P. Keeler, and S. Mukherjee, *Stochastic Geometry Analysis of Cellular Networks*. Cambridge University Press, 2018.

11. F. Baccelli, M. Klein, M. Lebourges, and S. Zuyev, "Stochastic geometry and architecture of communication networks," *Telecommunication Systems*, vol. 7, pp. 209–227, Jun 1997.

12. J. G. Andrews, F. Baccelli, and R. K. Ganti, "A tractable approach to coverage and rate in cellular networks," *IEEE Transactions on Communications*, vol. 59, pp. 3122–3134, Nov 2011.

13. A. AlAmmouri, J. G. Andrews, and F. Baccelli, "A unified asymptotic analysis of area spectral efficiency in ultradense cellular networks," *IEEE Transactions on Information Theory*, vol. 65, no. 2, pp. 1236–1248, 2019.

14. G. Nigam, P. Minero, and M. Haenggi, "Coordinated multipoint joint transmission in heterogeneous networks," *IEEE Transactions on Communications*, vol. 62, pp. 4134–4146, Nov 2014.

15. R. Irmer, H. Droste, P. Marsch, M. Grieger, G. Fettweis, S. Brueck, H.-P. Mayer, L. Thiele, and V. Jungnickel, "Coordinated multipoint: Concepts, performance, and field trial results," *IEEE Communications Magazine*, vol. 49, pp. 102–111, Feb 2011.

16. H. S. Dhillon, R. K. Ganti, F. Baccelli, and J. G. Andrews, "Modeling and analysis of K-tier downlink heterogeneous cellular networks," *IEEE Journal on Selected Areas in Communications*, vol. 30, pp. 550–560, Apr 2012.

17. J. Ginibre, "Statistical ensembles of complex, quaternion, and real matrices," *Journal of Mathematical Physics*, vol. 6, no. 3, pp. 440–449, 1965.

18. N. Miyoshi and T. Shirai, "A cellular network model with Ginibre configured base stations," *Advances in Applied Probability*, vol. 46, no. 3, pp. 832–845, 2014.

19. N. Deng, W. Zhou, and M. Haenggi, "The Ginibre point process as a model for wireless networks with repulsion," *IEEE Transactions on Wireless Communications*, vol. 14, pp. 107–121, Jan 2015.

20. A. Guo and M. Haenggi, "Spatial stochastic models and metrics for the structure of base stations in cellular networks," *IEEE Transactions on Wireless Communications*, vol. 12, pp. 5800–5812, Nov 2013.

21. M. Haenggi, J. G. Andrews, F. Baccelli, O. Dousse, and M. Franceschetti, "Stochastic geometry and random graphs for the analysis and design of wireless networks," *IEEE Journal on Selected Areas in Communications*, vol. 27, pp. 1029–1046, Sep 2009.

22. H. ElSawy, E. Hossain, and M. Haenggi, "Stochastic geometry for modeling, analysis, and design of multi-tier and cognitive cellular wireless networks: A survey," *IEEE Communications Surveys Tutorials*, vol. 15, pp. 996–1019, Third 2013.

23. M. Haenggi, "The meta distribution of the SIR in Poisson bipolar and cellular networks," *IEEE Transactions on Wireless Communications*, vol. 15, pp. 2577–2589, Apr 2016.

24. M. Haenggi, "Meta distributions—part 1: Definition and examples," *IEEE Communications Letters*, vol. 25, no. 7, pp. 2089–2093, 2021.

25. M. Haenggi, "Meta distributions—part 2: Properties and interpretations," *IEEE Communications Letters*, vol. 25, no. 7, pp. 2094–2098, 2021.

26. K. Feng and M. Haenggi, "Separability, asymptotics, and applications of the SIR meta distribution in cellular networks," *IEEE Transactions on Wireless Communications*, vol. 19, no. 7, pp. 4806–4816, 2020.

27. K. Feng and M. Haenggi, "The SINR meta distribution in Poisson cellular networks," *IEEE Wireless Communications Letters*, vol. 10, no. 7, pp. 1385–1389, 2021.

28. K. Feng and M. Haenggi, "On the location-dependent SIR gain in cellular networks," *IEEE Wireless Communications Letters*, vol. 8, no. 3, pp. 777–780, 2019.

29. K. Feng and M. Haenggi, "A tunable base station cooperation scheme for Poisson cellular networks," in *2018 52nd Annual Conference on Information Sciences and Systems (CISS)*, Mar 2018.

30. K. Feng and M. Haenggi, "A location-dependent base station cooperation scheme for cellular networks," *IEEE Transactions on Communications*, vol. 67, no. 9, pp. 6415–6426, 2019.

31. K. Feng and M. Haenggi, "Joint spatial-propagation modeling of cellular networks based on the directional radii of Poisson Voronoi cells," *IEEE Transactions on Wireless Communications*, vol. 20, no. 5, pp. 3240–3253, 2021.

32. Q. Cui, X. Yu, Y. Wang, and M. Haenggi, "The SIR meta distribution in Poisson cellular networks with base station cooperation," *IEEE Transactions on Communications*, vol. 66, pp. 1234–1249, Mar 2018.

33. M. Salehi, H. Tabassum, and E. Hossain, "Meta distribution of SIR in large-scale uplink and downlink NOMA networks," *IEEE Transactions on Communications*, vol. 67, pp. 3009–3025, Apr 2019.

34. N. Deng and M. Haenggi, "SINR and rate meta distributions for HCNs with joint spectrum allocation and offloading," *IEEE Transactions on Communications*, vol. 67, pp. 3709–3722, May 2019.

35. Y. Wang, M. Haenggi, and Z. Tan, "SIR meta distribution of K-tier downlink heterogeneous cellular networks with cell range expansion," *IEEE Transactions on Communications*, vol. 67, pp. 3069–3081, Apr 2019.

36. Y. Wang, M. Haenggi, and Z. Tan, "The meta distribution of the SIR for cellular networks with power control," *IEEE Transactions on Communications*, vol. 66, pp. 1745–1757, Apr 2018.

37. P. D. Mankar, H. S. Dhillon, and M. Haenggi, "Meta distribution analysis of the downlink SIR for the typical cell in a Poisson cellular network," in *IEEE Globecom*, 2019.

38. S. S. Kalamkar and M. Haenggi, "Simple approximations of the SIR meta distribution in general cellular networks," *IEEE Transactions on Communications*, vol. 67, pp. 4393–4406, Jun 2019.

39. S. Wang and M. Di Renzo, "On the meta distribution in spatially correlated non-Poisson cellular networks," *EURASIP Journal on Wireless Communications and Networking*, Jun 2019.

40. S. S. Kalamkar and M. Haenggi, "The spatial outage capacity of wireless networks," *IEEE Transactions on Wireless Communications*, vol. 17, pp. 3709–3722, Jun 2018.

41. M. Haenggi, "Efficient calculation of meta distributions and the performance of user percentiles," *IEEE Wireless Communications Letters*, vol. 7, pp. 982–985, Dec 2018.

42. S. Guruacharya and E. Hossain, "Approximation of meta distribution and its moments for poisson cellular networks," *IEEE Wireless Communications Letters*, vol. 7, pp. 1074–1077, Dec 2018.

43. X. Yu, Q. Cui, Y. Wang, N. Li, X. Tao, and M. Valkama, "Stochastic geometry based analysis for heterogeneous networks: a perspective on meta distribution," *Science in China Series F: Information Sciences*, vol. 63, pp. 1–21, 2020.

44. X. Lu, M. Salehi, M. Haenggi, E. Hossain, and H. Jiang, "Stochastic geometry analysis of spatial-temporal performance in wireless networks: A tutorial," *IEEE Communications Surveys & Tutorials*, Early Access, 2021.

45. S. S. Kalamkar and M. Haenggi, "Per-link reliability and rate control: Two facets of the SIR meta distribution," *IEEE Wireless Communications Letters*, vol. 8, pp. 1244–1247, Aug 2019.

46. M. Bennis, M. Debbah, and H. V. Poor, "Ultrareliable and low-latency wireless communication: Tail, risk, and scale," *Proceedings of the IEEE*, vol. 106, pp. 1834–1853, Oct 2018.

47. R. K. Ganti and M. Haenggi, "Asymptotics and approximation of the SIR distribution in general cellular networks," *IEEE Transactions on Wireless Communications*, vol. 15, pp. 2130–2143, Mar 2016.

48. N. Miyoshi and T. Shirai, "Tail asymptotics of signal-to-interference ratio distribution in spatial cellular network models," *Probability and Mathematical Statistics*, vol. 37, pp. 431–453, Jan 2017.

49. X. Zhang and M. Haenggi, "The performance of successive interference cancellation in random wireless networks," *IEEE Transactions on Information Theory*, vol. 60, pp. 6368–6388, Oct 2014.

50. 3GPP, "Study on scenarios and requirements for next generation access technologies," Tech. Rep. 38.913, 3rd Generation Partnership Project (3GPP), 2020.

51. 3GPP, "Base Station (BS) radio transmission and reception," Tech. Rep. 38.104, 3rd Generation Partnership Project (3GPP), 2020.

52. P. Madhusudhanan, J. G. Restrepo, Y. Liu, T. X. Brown, and K. R. Baker, "Downlink performance analysis for a generalized shotgun cellular system," *IEEE Transactions on Wireless Communications*, vol. 13, no. 12, pp. 6684–6696, 2014.

53. X. Zhang and M. Haenggi, "The performance of successive interference cancellation in random wireless networks," *IEEE Transactions on Information Theory*, vol. 60, no. 10, pp. 6368–6388, 2014.

54. M. Haenggi, "On distances in uniformly random networks," *IEEE Transactions on Information Theory*, vol. 51, pp. 3584–3586, Oct 2005.

55. R. K. Ganti and M. Haenggi, "Asymptotics and approximation of the SIR distribution in general cellular networks," *IEEE Transactions on Wireless Communications*, vol. 15, no. 3, pp. 2130–2143, 2016.

56. M. Nakagami, "The m-distribution—a general formula of intensity distribution of rapid fading," in *Statistical Methods in Radio Wave Propagation*, pp. 3–36, Pergamon, 1960.

57. S. Guruacharya and E. Hossain, "Approximation of meta distribution and its moments for Poisson cellular networks," *IEEE Wireless Communications Letters*, vol. 7, no. 6, pp. 1074–1077, 2018.

58. O. Macchi, "The coincidence approach to stochastic point processes," *Advances in Applied Probability*, vol. 7, no. 1, pp. 83–122, 1975.

59. L. Decreusefond, I. Flint, and A. Vergne, "A note on the simulation of the Ginibre point process," *Journal of Applied Probability*, vol. 52, no. 4, pp. 1003–1012, 2015.

60. X. Zhang and M. Haenggi, "A stochastic geometry analysis of inter-cell interference coordination and intra-cell diversity," *IEEE Transactions on Wireless Communications*, vol. 13, no. 12, pp. 6655–6669, 2014.

61. F. Baccelli and A. Giovanidis, "A stochastic geometry framework for analyzing pairwise-cooperative cellular networks," *IEEE Transactions on Wireless Communications*, vol. 14, pp. 794–808, Feb 2015.

62. J. Yoon and G. Hwang, "Distance-based inter-cell interference coordination in small cell networks: Stochastic geometry modeling and analysis," *IEEE Transactions on Wireless Communications*, vol. 17, pp. 4089–4103, Jun 2018.

63. R. Tanbourgi, S. Singh, J. G. Andrews, and F. K. Jondral, "A tractable model for noncoherent joint-transmission base station cooperation," *IEEE Transactions on Wireless Communications*, vol. 13, pp. 4959–4973, Sep 2014.

64. Q. Cui, X. Yu, Y. Wang, and M. Haenggi, "The SIR meta distribution in Poisson cellular networks with base station cooperation," *IEEE Transactions on Communications*, vol. 66, pp. 1234–1249, Mar 2018.

65. A. H. Sakr and E. Hossain, "Location-aware cross-tier coordinated multipoint transmission in two-tier cellular networks," *IEEE Transactions on Wireless Communications*, vol. 13, pp. 6311–6325, Nov 2014.

66. X. Zhang and M. Haenggi, "A stochastic geometry analysis of inter-cell interference coordination and intra-cell diversity," *IEEE Transactions on Wireless Communications*, vol. 13, pp. 6655–6669, Dec 2014.

67. M. Haenggi, "The mean interference-to-signal ratio and its key role in cellular and amorphous networks," *IEEE Wireless Communications Letters*, vol. 3, pp. 597–600, Dec 2014.

68. A. Guo and M. Haenggi, "Joint spatial and propagation models for cellular networks," in *2015 IEEE Global Communications Conference (GLOBECOM)*, Dec 2015.

69. M. Gudmundson, "Correlation model for shadow fading in mobile radio systems," *Electronics Letters*, vol. 27, pp. 2145–2146, Nov 1991.

70. F. Baccelli and X. Zhang, "A correlated shadowing model for urban wireless networks," in *2015 IEEE Conference on Computer Communications (INFOCOM)*, pp. 801–809, Apr 2015.

71. S. S. Szyszkowicz, H. Yanikomeroglu, and J. S. Thompson, "On the feasibility of wireless shadowing correlation models," *IEEE Transactions on Vehicular Technology*, vol. 59, pp. 4222–4236, Nov 2010.

72. B. Błaszczyszyn, M. K. Karray, and H. P. Keeler, "Wireless networks appear Poissonian due to strong shadowing," *IEEE Transactions on Wireless Communications*, vol. 14, pp. 4379–4390, Aug 2015.

73. N. Ross and D. Schuhmacher, "Wireless network signals with moderately correlated shadowing still appear Poisson," *IEEE Transactions on Information Theory*, vol. 63, pp. 1177–1198, Feb 2017.

74. E. Gilbert, "Random subdivisions of space into crystals," *The Annals of mathematical statistics*, vol. 33, no. 3, pp. 958–972, 1962.

75. A. Hayen and M. Quine, "Areas of components of a Voronoi polygon in a homogeneous Poisson process in the plane," *Advances in Applied Probability*, vol. 34, no. 2, pp. 281–291, 2002.

76. P. D. Mankar, P. Parida, H. S. Dhillon, and M. Haenggi, "Distance from the nucleus to a uniformly random point in the 0-cell and the typical cell of the

Poisson-Voronoi tessellation," *Journal of Statistical Physics*, vol. 181, pp. 1678–1698, 2020.

77. M. Haenggi, "User point processes in cellular networks," *IEEE Wireless Communications Letters*, vol. 6, pp. 258–261, Apr 2017.

78. L. Muche, "The Poisson-Voronoi tessellation: relationships for edges," *Advances in Applied Probability*, vol. 37, no. 2, pp. 279–296, 2005.

79. V. Baumstark and G. Last, "Some distributional results for Poisson-Voronoi tessellations," *Advances in Applied Probability*, vol. 39, pp. 16–40, 2007.

80. P. Calka, "The distributions of the smallest disks containing the Poisson-Voronoi typical cell and the Crofton cell in the plane," *Advances in Applied Probability*, vol. 34, no. 4, p. 702–717, 2002.

81. J. Møller and S. Zuyev, "Gamma-type results and other related properties of Poisson processes," *Advances in Applied Probability*, vol. 28, no. 3, p. 662–673, 1996.

82. S. Zuyev, "Stopping sets: Gamma-type results and hitting properties," *Advances in Applied Probability*, vol. 31, no. 2, pp. 355–366, 1999.

83. H. E. Robbins, "On the measure of a random set," *The Annals of Mathematical Statistics*, vol. 15, pp. 70–74, Mar 1944.

84. J. Mecke, "On the relationship between the 0-cell and the typical cell of a stationary random tessellation," *Pattern Recognition*, vol. 32, no. 9, pp. 1645–1648, 1999.

85. D. Hug, M. Reitzner, and R. Schneider, "Large Poisson-Voronoi cells and Crofton cells," *Advances in Applied Probability*, vol. 36, no. 3, pp. 667–690, 2004.

86. M. Haenggi, "On distances in uniformly random networks," *IEEE Transactions on Information Theory*, vol. 51, pp. 3584–3586, Oct 2005.

87. K. S. Ali, M. Haenggi, H. ElSawy, A. Chaaban, and M.-S. Alouini, "Downlink Non-Orthogonal Multiple Access (NOMA) in Poisson Networks," *IEEE Transactions on Communications*, vol. 67, pp. 1613–1628, Feb 2019.

88. M. Haenggi, "A geometric interpretation of fading in wireless networks: Theory and applications," *IEEE Transactions on Information Theory*, vol. 54, pp. 5500–5510, Dec 2008.

89. B. Blaszczyszyn, M. K. Karray, and F. Klepper, "Impact of the geometry, path-loss exponent and random shadowing on the mean interference factor in wireless cellular networks," in *Wireless and Mobile Networking Conference (WMNC) 2010*, Oct 2010.